Universidad de Málaga

Escuela Técnica Superior de Ingeniería de Telecomunicación

TESIS DOCTORAL

Integrated coherent reception and polarization management for next generation access networks

Autor:

JOSÉ DARÍO SARMIENTO MERENGUEL

Directores:

ROBERT HALIR
ALEJANDRO ORTEGA MOÑUX

AUTOR: José Darío Sarmiento Merenguel

http://orcid.org/0000-0003-4397-2611

EDITA: Publicaciones y Divulgación Científica. Universidad de Málaga

Dr.D. Robert Halir y Dr.D. Alejandro Ortega Moñux, profesores doctores del Departamento de Ingeniería de Comunicaciones de la Universidad de Málaga

CERTIFICAN:

Que D. José Darío Sarmiento Merenguel, Ingeniero de Telecomunicación, ha realizado en el Departamento de Ingeniería de Comunicaciones de la Universidad de Málaga bajo su dirección, el trabajo de investigación correspondiente a su TESIS DOCTORAL titulada:

Integrated coherent reception and polarization management for next generation access networks

En dicho trabajo se han expuesto diversas aportaciones originales, entre las que cabe destacar el diseño de un receptor coherente con diversidad de polarización, monolíticamente integrado, que elude el uso de dispositivos de control de polarización, que tradicionalmente representan el elemento más crítico del receptor, debido a sus reducidas tolerancias. Además, se ha implementado un controlador de polarización, con unas prestaciones del estado del arte, siendo compatible con tecnologías de fabricación CMOS y altas tolerancias. Por último, en el área de dispositivos SWG, se ha realizado un minucioso análisis numérico y experimental de la importancia de las pérdidas por leakage en guías periódicas sublongitud de onda. Los resultados expuestos han dado lugar a publicaciones en revistas internacionales de alto nivel de impacto y aportaciones a congresos de ámbito nacional e internacional.

Por todo ello, consideran que esta Tesis es apta para su presentación al tribunal que ha de juzgarla. Y para que conste a efectos de lo establecido en el Real Decreto 99/2011, de 28 de enero, por el que se regulan las enseñanzas oficiales de doctorado, AUTORIZAN la presentación de esta Tesis en la Universidad de Málaga.

Málaga, a _____ de _____ de 2017

Fdo.: Dr.D. Robert Halir

Fdo.: Dr.D. Alejandro Ortega Moñux

E.T.S.I.Telecomunicación, Campus de Teatinos, 29071-MÁLAGA, Tlf.: 952131440, Fax: 952132927

UNIVERSIDAD DE MÁLAGA
ESCUELA TÉCNICA SUPERIOR DE INGENIERÍA DE TELECOMUNICACIÓN

Reunido el tribunal examinador en el día de la fecha, constituido por:

Presidente: Dr. D. _____

Secretario: Dr. D. _____

Vocal: Dr. D. _____

para juzgar la Tesis Doctoral titulada **Integrated coherent reception and polarization management for next generation access networks** realizada por D. Jose Darío Sarmiento Merenguel y dirigida por el Dr. D. Robert Halir y el Dr. D. Alejandro Ortega Moñux, acordó por

_____

otorgar la calificación de

_____

y para que conste, se extiende firmada por los componentes del tribunal la presente diligencia.

Málaga, a _____ de _____ de _____

El Presidente: El Secretario: El Vocal:

Fdo.: _____ Fdo.: _____ Fdo.: _____

Integrated coherent reception and polarization management for next generation access networks

Jose Darío Sarmiento Merenguel

To María,
my parents,
and my brother.

Acknowledgements

Gracias papá y mamá, por el apoyo que seguís brindadome día a día, y por haber sabido guiarme en todo momento.

Gracias a mi amor, María, por hacer que todo sea más fácil, por aguantar mis agobios, pero sobre todo gracias por entenderme, prometo que si nos volvemos a casar, no realizaré ninguna estancia en los meses previos a la boda.

Gracias a Carlos y Elena por hacerme ver las cosas de otro modo, pero sobre todo, gracias por compartir vuestra calidad humana.

Gracias a mis directores de tesis, Robert y Alejandro... gracias por vuestro apoyo y por vuestra infinita paciencia. Sin duda alguna dos genios que, además de contribuir al desarrollo de la tesis, han contribuido a mi desarrollo personal. Robert, gracias por haberme orientado durante este tiempo y por compartir conmigo tu pragmatismo y tu eficiencia. Alejandro, gracias por tu infinita paciencia y dedicación, por hacerme ver que no existen objetivos inalcanzables, sino trabajo y constancia.

Gracias a todos los compañeros del laboratorio de fotónica, Jose Manuel, Alejandro, Abdel y Daniel, por todos los momentos compartidos en este tiempo, espero que el Mc Flurry del jueves y la hamburguesa del viernes se conviertan en una tradición.

Gracias a Gonzalo Wangüemert, quien me abrió las puertas a la investigación, y me ha enseñado tanto durante este tiempo, gracias por tu gran humanidad.

Gracias José Raul por haber sido fuente de inspiración constante, al fin somos doctores y tendremos tiempo para vernos más a menudo.

Jose Darío Sarmiento Merenguel
Málaga, Spain
September 2017

Contents

1 Introduction

THIS work is devoted to the design, and characterization of an integrated polarization controller achieving state-of-the-art perfomances and the implementation and characterization of a coherent receiver with polarization diversity, both of them with a remarkable improvement on the tolerances to fabrication deviations. Furthermore, a contribution to the field of photonic integrated metamaterials is described. In this opennig chapter the relevance of photonics is first provided (section 1.1), then the general framework of the presented work is overwieved (section 1.2). Finally in section 1.3, the organisation of the thesis is given.

1.1. The science of light

Light has always played an extraordinary role in the human evolution. Light is in the origin of life, being essential for most of the life forms. The dominance of light has set one of the most important milestones along the human history. The first time we achieved the control of light dates back to the Pleistocene, when our ancestors takes the control of fire [1]. This achievement was an inflection point in the human being evolution, as it allows cooking, warming and protection against predators. From then on, light have played a central role in the human everyday life. Furthermore, the pursuit of understanding the nature of light have been a boost to the development of physics and science in general.

It has been very recently, that the human have reached another light related milestone, the invention of the laser. In 1960, Theodore Maiman realized the first working laser, based on the use of a ruby crystal as a gain medium [2]. This invention set the origin of the science of light, comprising its generation, control, and detection, also known as Photonics. Since then, a wide variety of Photonics applications have appeared:

- Energy applications, comprising applications such as photovoltaics for energy production, lighting, and even the optical lithography, in which high energy lasers enable the fabrication of micro-electronics devices.

- Medical applications, such as non-invasive laser surgery, or even non-invasive oxygen saturation meter and more recently, optical coherent tomography.

- Measurement and sensor applications, including applications ranging from spectroscopy, glass fiber sensors and more recently biomolecular detectors that are envisioned to change the current medicine practice.
- Information technology, comprising applications such as optical communications, rangin from long-distance communications to on-chip optical interconnection, and optical storage i.e. CD and DVD technologies.

Photonics wasn't the only term related with light appeared in the 60s. In 1969 S. E. Miller, who had envisioned the potential of optical communications, coined the term of integrated optics, referring to the fabrication of many optical components in a single substrate [3]. In his paper Miller proposed the miniaturization of the laser circuitry, setting the basis of integrated photonics. Miller also described the advantages of integration in terms of thermal and mechanical isolation, while for communication purposes he highlighted a reduction in power consumption. However, he recognized the difficulty of their prospects, while at the same time believed they are worth the serious required effort.

Since then, an important part of the photonics research activity has been devoted to the integration of photonics applications, giving raise to the broad discipline of integrated photonics. Integrated photonics circuits have already been demonstrated, with a huge range of applications and functionalities: optical transmitters and receivers, gas sensors, lab-on-chip devices, and microwave signal processors.

Among the different mentioned applications, optical communications probably is the application of photonics that has shown the deepest impact in the modern society. The birth of optical communications is found in the 60s, with the invention of the semiconductor laser and the invention of the ultra-low loss silica glass optical fiber. The first commercial deployments of optical communication networks dates from the end of the 70s [4], kickstarting the race for ever better performances.

Optical communications are at the core of the worldwide internet network, whose global traffic evolution, shown in figure 1.1, grows almost exponentially [5]. In order to satisfy the ever growing bandwidth requirements, optical communications have been continuously evolving, from the first intensity-modulation direct-detection (IM-DD) schemes, achieving data rates below 1 Gbps in distances below 50 km [6] to the recently commercially available coherent schemes, achieving data rates up to 100 Gbps and link distances higher than 1000 km [7].

During the last years, bandwidth-hungry applications such as social networking (Instagram, Facebook) and video streaming (Netflix, Youtube) together with the advent of cloud computing based services have pushed the copper links in data-centers to its limits, giving an opportunity to optical communications to go beyond its traditional scope (long distance communications, commonly referred as telecom applications in the bibliography [4]) to a new niche consisting of short distance and low power optical communications, commonly referred as datacom applications. In this new scope, provided the massive number of required transceivers, the cost becomes crucial, with most of the proposed schemes based on IM-DD schemes.

In both telecom and datacom applications, the use of the polarization of light can be exploited to improve the performance of the optical links. In datacom applications, schemes based on polarization modulation have been recently proposed as a

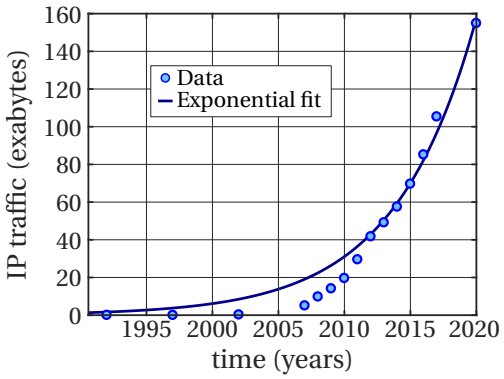

Figure 1.1.: Global IP Traffic reported by Cisco VNI [5]

cost-effective alternative to IM-DD schemes, improving the spectral efficiency and enabling channel linearization [8]. In telecom applications, polarization of light is used to multiplex information on two orthogonal polarization states, enabling a two-fold increase of the available data rate [9, 10].

Another improvement of the current optical communication systems lays on the optical bandwidth. Most of the current approaches are designed to work in the C-Band, which is the portion of the electromagnetic spectrum comprising wavelengths from 1530 to 1550 nm. In the future this band may not be enough to satisfy the bandwidth necessity, so receivers working in a broader wavelength range will be required. Among others factors, the bandwidth of the receivers is limited by dispersion, that severely hinders the behavior of the receiver when the operation wavelengths differs from the designed wavelength. Recently, subwavelength gratings (SWG), i.e., structures with periods small enough to suppress diffraction, have been used to implement dispersion engineered metamaterials that enables ultra-broadband devices [11, 12].

The primary focus of this thesis lays on the implementation of polarization diversity devices. Thus, on one side a novel integrated polarization controller scheme, with highly relaxed fabrication tolerances is implemented. On the other side, a monolithically integrated dual polarization coherent receiver, that avoids the use of polarization managing devices is implemented. Finally, a complementary work about the leakage losses on SWG devices is presented.

1.2. Overview of this thesis

In this section, the work presented in this thesis is succinctly outlined. It is worth to mention that provided the different nature of the topics presented in this thesis, a more detailed revision of the state of the art is provided at the beginning of each chapter. The realized work has been divided in three different subsections, according to the topic in which they are framed. A graphical summary of the realized work is also presented in figure 1.2.

Integrated Polarization Controller

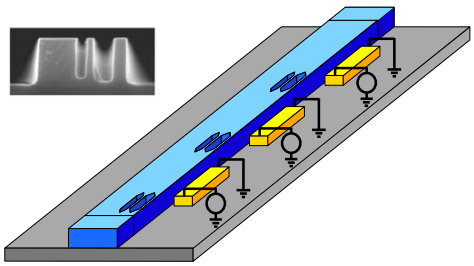

High fabrication tolerances

Fully compatible with CMOS process

Exhibits 40 dB in polarization extinction ratio range

Monolithically integrated dual polarization coherent receiver

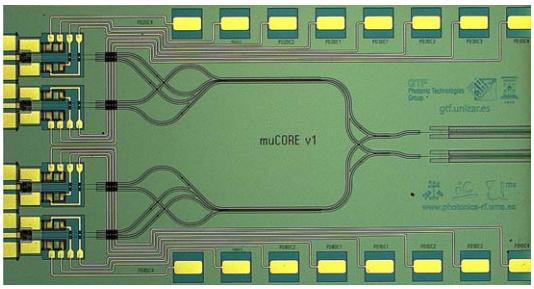

Implemented in InP

OIF compliant

Avoids the use of polarization management integrated devices

Leakage losses in SWG devices

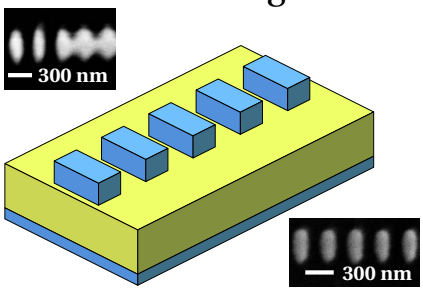

A relation between effective index and leakage losses is reported

Techniques to ease the design of SWG are established.

Figure 1.2.: Summary of the work realized in this thesis

1.2.1. Integrated polarization management

Polarization of light has found a wide range of applications apart from the previously reported in optical communications [13]. Chemists use the fact that organic materials rotate the polarization of light to analyze the structure of new organic molecules. Polarization is also exploited by biologist, as it differentiates organic tissues in optical coherent tomography applications [14], and more recently, quantum physicist make use of polarization for quantum key distribution [15]. Integrated polarization devices have been proposed since the early 1980s implementing different functionalities such as polarization rotation, polarization beam splitting and polarization control [16]. Most of the polarization controllers reported to date either are integrable but achieve poor performances or achieve good performances by sacrifying the integrability [17].

One of the goals of this thesis is the implementation of an integrated polarization controller, that allows to change any arbitrary polarization state into any other arbitrary polarization state. This polarization controller is implemented using a technology-independent scheme based on polarization rotators and polarization phase shifters. Such a scheme allows to employ polarization rotators with largely relaxed fabrication tolerances, improving the tolerance to fabrication deviations of the device. The polarization controller has been designed and fabricated in the Silicon-On-Insulator platform. Operation along the complete C-Band has been demonstrated, achieving a polarization extinction ratio range of 40 dB ($\pm$ 20 dB). This is the highest polarization extinction ratio achieved in a fully integrated polarization controller, overcoming the trade-off between integration and performances. It is worth mentioning that this part of the thesis has been developed in collaboration with the Université Paris-Sud.

1.2.2. Integrated dual polarization coherent reception

As previously discussed, polarization of light can be exploited in order to double the capacity of optical communications links. First reported results on polarization multiplexing dates back to the beginning of the 90s [18]. Since then, different approaches of coherent receivers with polarization diversity have been proposed and even commercialized [19]. However, the inclusion of integrated polarization diversity devices, such as the polarization beam splitters (PBSs), holds a significant drawback, due to the low tolerances of these devices to fabrication deviations, that leads to very low fabrication yields. This non-solved problem, has led the Optical Internetworking Forum (OIF) to establish the integration of the polarization diversity circuitry as non mandatory [20], resulting in devices with polarization diversity circuitry implemented in bulk optics and difficulting the integration and miniaturization of the receiver, which ultimately increments the cost of the receiver.

One of the goals of this thesis is the implementation of a monolithically integrated dual polarization coherent receiver, which does require neither PBSs nor additional signal processing algorithms to realize the polarization demultiplexing, increasing the tolerances of the device to fabrication deviations. The genunine operation of this receiver was previsouly conceived in the research group, [21]. In this receiver, the PBS is replaced by a polarization diversity network consisting of 4 birefringent waveguides, that will induce a certain polarization phase shift. The receiver have been designed

and fabricated in the InP platform. This work have been developed in the framework of a Spanish national research project, realized in collaboration with the Universidad de Zaragoza.

1.2.3. Leakage Losses in SWG structures

As mentioned in the previous sections, SWG enable the engineering of materials dispersion, which can be used for example to achieve broadband devices. The first published work using SWG was reported in [22]. From then on, SWG has found widespread use in integrated photonics, enabling highly efficient surface gratings couplers, compact polarization splitters and wavelength multiplexers, and polarization independent grating couplers, to name but a few applications [12, 23–26]. Nevertheless, the implementation of SWG devices has a minor drawback, that has to be carefully addressed during device design: the use of SWG structures entails a decrease of the modal confinement, that may induce prohibitive losses, which ultimately may result in useless devices.

In this thesis, a deep analysis of the leakage losses in SWG devices has been both numerically and experimentally realized. For this purpose a set of SWG waveguides, has been designed and fabricated in the Silicon on Insulator platform. It has been concluded that there is a relation between the leakage losses and the Bloch Floquet effective index in SWG waveguides. Furthermore, some rules that ease the design of SWG devices have been extracted.

1.3. Organization of this thesis

This thesis is structured in six chapters, organized as follows:

Chapter 2 of this thesis provides the fundamental basis of polarization. Thus, section 2.2 covers the formal description of polarization of light, together with the main formalisms used to describe the polarization of light and to model polarization sensitive systems. Section 2.3 and 2.4 are devoted to give an overview of the state of the art in polarization management devices, namely polarization phase shifters and rotators.

Chapter 3 is focussed on the design of an integrated polarization controller. First of all, its principle of operation is provided in section 3.2. 3.3 provides all the details about the design of the polarization controller, while the characterization of the device is given in section and 3.4.

Chapter 4 includes the implementation of a dual polarization coherent receiver. The historical background of coherent communications systems, together with its operation principle is provided in sections 4.1 and 4.2. Section 4.3 will focus on coherent receivers principle of operation, describing its main subsystems. Then, section 4.4 aims to describe the principle of operation of the implemented coherent receiver, while section 4.5 will focus on its design. At the end of this chapter, in section 4.6 the preliminary results of the receiver characterization are provided.

Chapter 5 is devoted to the leakage losses in SWG devices, demonstrating the relation between the modal effective index and the leakage losses in SWG structures. Thus, after reviewing the main SWG simulation strategies on section 5.2, the numerical demonstration of the referred relation is provided in section 5.3, while the experi-

mental demonstration is shown in section 5.4. Then, in section 5.5 some of the main conclusions of chapter are reviewed.

Finally, in chapter 6 the conclusions (section 6.1), together with other contributions of the author that are not included in this manuscript (section 6.2) are provided. The prospects of the presented work are given in section 6.3.

2
Polarized lightwaves

2.1. Introduction

The polarization of light is a phenomenon of a high interest in the understanding of the physical world while at the same time has a broad range of applications in a wide variety of settings, from advanced research laboratories to common household.

The most familiar household application of polarization is found on polarized sunglasses, widely use in car driving. These glasses filter the specularly reflected light from flat paved surfaces, avoiding glare from sun reflection. Another familiar example of polarized glasses is found on the 3D cinema, where polarization is exploited to provide stereoscopic vision. Light polarization is also the physical phenomena that lays on the operation of the widely used LCD screen.

In scientific scenarios, there are many measurement techniques that are based on the polarization of light: in materials engineering polarization is used to characterize the mechanical stress, in geology it is used to identify different materials while in chemistry it is used to determine concentration of organic molecules. Polarization of light also plays a key role in integrated photonics, with different applications reported to date, mainly in the field of optical communications. Most of the integrated photonics applications related with the polarization of light make use of a reduced set of polarization managing devices such as polarization beam splitters, polarization phase shifters, polarization converter and polarization controllers.

In this chapter, we first provide a formal description of the polarization of light (section 2.2). We then focus on two integrated photonics devices, such as the polarization phase shifters (section 2.3) and the polarization rotator (section 2.4), which are the more fundamental polarization managing devices. A state of the art on the implementation of these devices together with its fundamental operation principle is also provided.

2.2. Describing the polarization of light

The electric field of a monochromatic plane lightwave, propagating along the z-axis in an isotropic medium, as depicted in figure 2.1 a), can be described using the following expression [27]:

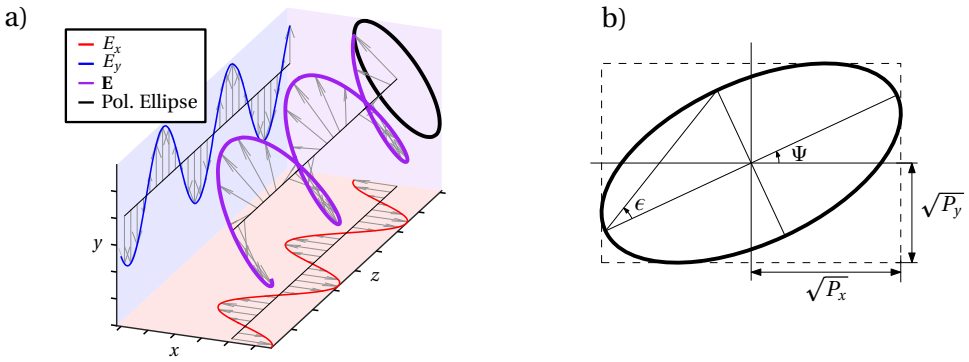

Figure 2.1.: a) Electric field of a monochromatic plane lightwave propagating in the along the z axis. b) Polarization ellipse, used to graphically represent the state of polarization of a lightwave.

$$\mathbf{E}(x,y,z,t) = \mathrm{Re}\left\{(A_x\hat{\mathbf{x}} + A_y\hat{\mathbf{y}})e^{j(\omega t-\beta z)}\right\} \tag{2.1}$$

where A_x and A_y are the complex amplitudes in the x and y direction, ω is the angular optical frequency and β the propagation constant of the field. The polarization of such a lightwave is defined as the temporal evolution of the locus of the electric field tip, in a plane perpendicular to the propagation direction, as depicted in figure 2.1 a), where the locus is the black colored ellipse. The complex amplitudes are given by their magnitudes, $\sqrt{P_x}$ and $\sqrt{P_y}$, and their phases φ_x and φ_y. Looking at the electric field components in the $z = 0$ plane, they can be expressed as:

$$e_x = \sqrt{P_x}\cos(\omega t - \varphi_x) \tag{2.2}$$

$$e_y = \sqrt{P_y}\cos(\omega t - \varphi_y) \tag{2.3}$$

These expressions constitute the parametric equations of the following ellipse:

$$\frac{e_x^2}{P_x} + \frac{e_y^2}{P_y} - \frac{e_y e_x}{\sqrt{P_x P_y}}\cos(\varphi_x - \varphi_y) = \sin^2(\varphi_x - \varphi_y) \tag{2.4}$$

This ellipse, which is separately shown in figure 2.1 b), is known as the polarization ellipse, and is useful to graphically represent the state of polarization of an electromagnetic lightwave. The polarization ellipse is defined by its ellipticity angle (ϵ) and its orientation angles (ψ) , with ϵ in $(-\pi/4, \pi/4)$ and ψ in $(-\pi/2, \pi/2)$. These angles can be defined in terms of the phase and magnitude of the field components:

$$\sin(2\epsilon) = \frac{2\sqrt{P_y/P_x}}{1 + P_y/P_x}\sin(\varphi_x - \varphi_y) = \frac{2\sqrt{PR}}{1+PR}\sin(\rho) \tag{2.5}$$

$$\tan(2\Psi) = \frac{2\sqrt{P_y/P_x}}{1 - P_y/P_x}\cos(\varphi_x - \varphi_y) = \frac{2\sqrt{PR}}{1-PR}\cos(\rho) \tag{2.6}$$

The polarization of an electromagnetic wave, is also fully defined using two parameters, the polarization ratio (PR), defined as PR = P_y/P_x and the polarization phase (ρ), defined as $\rho = \varphi_x - \varphi_y$. In the general case, the polarization of an electromagnetic wave is elliptical. However, this ellipse can degenerate in a straight line or in a circle, giving raise to the linear and circular polarizations. Table 2.1 shows the conditions that the PR and ρ have to meet, so that the polarizations is linear, circular or elliptical.

Polarization	PR	ρ
Linear	PR = $[0,\infty]$	$\rho = 0, \pi$
Circular	PR = 1	$\rho = \pm(2k+1)\frac{\pi}{2}$
Elliptical	PR = $(0,\infty)$	$\rho \neq 0, \pm(2k+1)\frac{\pi}{2}$

Table 2.1.: Polarization ratio and polarization phase of the elliptical, linear and circular states of polarization.

So far, the definition of polarization and a compact graphical representation of the state of polarization of a lightwave have been described. However, in order to model and characterize polarization sensitive optical systems this is not enough. Thus, in the following, some useful formalisms that ease the modeling and characterization of polarization sensitive systems and the representation of the polarization state evolution are presented. In subsection 2.2.1 the Jones calculus, which is useful to model polarization sensitive systems is presented. Section 2.2.2 is devoted to the Poincaré sphere, which is used to graphically represent polarization states. In section 2.2.3 the Stokes parameters, that describe polarization states and can be easily measured, are presented. Finally, as the origin of these formalisms lies the free space optics, section 2.2.4 aims to show that they can be used in integrated optics as well.

2.2.1. The Jones Calculus

The Jones calculus, proposed by Robert Clark Jones in 1941 [28], consists in a two-dimensional algebra used to represent the state of polarization (SOP) and to model systems that influence the state of polarization. Thus, polarization states are represented using 2×1 vectors, while linear polarization sensitive systems are represented using 2×2 matrices.

2.2.1.1. Definition of Jones vectors and Jones matrices

The elements of a Jones vector correspond with the complex amplitudes in the x and y direction, that fully determines the state of polarization, as shown in 2.4. Thus, a Jones vector is defined as:

$$\mathbf{E} = \begin{bmatrix} \sqrt{P_x} e^{j\varphi_x} \\ \sqrt{P_y} e^{j\varphi_y} \end{bmatrix}. \tag{2.7}$$

The Jones vectors can also be represented in terms of the polarization ellipse parameters as follows:

$$\mathbf{E} = e^{j\rho} \begin{bmatrix} \cos(\epsilon)\cos(\Psi) + j\sin(\epsilon)\sin(\Psi) \\ \cos(\epsilon)\sin(\Psi) + j\sin(\epsilon)\cos(\Psi) \end{bmatrix}. \tag{2.8}$$

Furthermore, when the absolute phase and magnitude of the electric field are irrelevant, Jones vectors are represented in terms of the polarization ratio and the polarization phase:

$$\mathbf{E} = \begin{bmatrix} ae^{j\rho} \\ \\ \sqrt{1-a^2} \end{bmatrix}, \tag{2.9}$$

with

$$a = \sqrt{\frac{1}{1+\mathrm{PR}}}. \tag{2.10}$$

As an example, table 2.2 shows the Jones vectors of some states of polarization.

Polarization	Jones Vector	
Linear Horizontal / Linear Vertical	$\begin{bmatrix} 1 \\ 0 \end{bmatrix}$	$\begin{bmatrix} 1 \\ 0 \end{bmatrix}$
Linear 45º / Linear -45º	$\frac{1}{\sqrt{2}}\begin{bmatrix} 1 \\ 1 \end{bmatrix}$	$\frac{1}{\sqrt{2}}\begin{bmatrix} -1 \\ 1 \end{bmatrix}$
Right Handed Circular/Left Handed Circular	$\frac{1}{\sqrt{2}}\begin{bmatrix} e^{j\pi/2} \\ 1 \end{bmatrix}$	$\frac{1}{\sqrt{2}}\begin{bmatrix} e^{-j\pi/2} \\ 1 \end{bmatrix}$

Table 2.2.: Jones vectors of the main states of polarization

The Jones matrices are used to operate with the Jones vectors. Thus, they model the propagation of polarized light through polarization sensitive optical systems. These matrices relates the Jones vector at the output of a polarization sensitive system with the Jones vector at its input, as follows:

$$\mathbf{E_{OUT}} = \overline{\overline{M_J}}\,\mathbf{E_{IN}} \tag{2.11}$$

where $\overline{\overline{M_J}}$ is a generic Jones matrix, defined as:

$$\overline{\overline{M_J}} = \begin{bmatrix} J_{11} & J_{12} \\ J_{21} & J_{22} \end{bmatrix} \tag{2.12}$$

where $J_{i,j}$ are complex coefficients that depend on the system characteristics. As transmission matrices, Jones matrices can be concatenated, so complex polarization sensitive systems can be modeled by using simpler Jones matrices. In the following subsection, the Jones matrices of the more common polarization sensitive optical systems are derived.

2.2.1.2. Jones matrices of common polarization sensitive optical systems

The simplest polarization sensitive device is the polarizer. This device only allows the transmission of a lightwave if it is aligned with its transmision axis. To understand

its principle of operation, let's consider an horizontal polarizer, wich only transmit horizontally polarized light so, given an arbitrary SOP at the input of the device, only the horizontal component will be at the output of the device. This behaviour can be expressed with the following Jones matrix:

$$\overline{\overline{M_{\mathrm{H-POL}}}} = \begin{bmatrix} 1 & 0 \\ 0 & 0 \end{bmatrix}. \tag{2.13}$$

In general, it is useful to know the Jones Matrix of a polarizer that have been rotated through an angle θ. To calculate the Jones matrix of a rotated device, as the rotated polarizer, we make use of the rotation transformation defined as:

$$\overline{\overline{M_{RJ}(\theta)}} = \overline{\overline{R(\theta)}} \cdot \overline{\overline{M_J}} \cdot \overline{\overline{R(-\theta)}}, \tag{2.14}$$

where $\overline{\overline{M_J}}$ is the original Jones matrix and $\overline{\overline{M_{RJ}(\theta)}}$ is the Jones matrix of the rotated device. The rotation matrix, $\overline{\overline{R(\theta)}}$ is defined as

$$\overline{\overline{R(\theta)}} = \begin{bmatrix} \cos(\theta) & \sin(\theta) \\ -\sin(\theta) & \cos(\theta) \end{bmatrix}. \tag{2.15}$$

Thus, the Jones matrix of a θ-rotated polarizer, $\overline{\overline{M_{\mathrm{H-POL}}(\theta)}}$, can be calculated as:

$$\overline{\overline{M_{\mathrm{RH-POL}}(\theta)}} = \overline{\overline{R(\theta)}} \cdot \overline{\overline{M_{\mathrm{H-POL}}}} \cdot \overline{\overline{R(-\theta)}}, \tag{2.16}$$

obtaining the following Jones matrix:

$$\overline{\overline{M_{\mathrm{RH-POL}}(\theta)}} = \begin{bmatrix} \cos^2\theta & \cos\theta\sin\theta \\ \cos\theta\sin\theta & \sin^2\theta \end{bmatrix}. \tag{2.17}$$

Another important polarization sensitive device, is the polarization phase shifter (PPS), also known as retarder [29]. This element will introduce a phase shift between the horizontal and vertical components. If the optical axes are aligned with the with the x and y axes, the Jones matrix of a PPS is defined as:

$$\overline{\overline{M_{PPS}(\Delta\rho)}} = \begin{bmatrix} e^{j\Delta\rho} & 0 \\ 0 & 1 \end{bmatrix}, \tag{2.18}$$

where $\Delta\rho$ is the induced polarization phase shift. From this matrix, it can be observed that the output Jones vector will be similar to the input one, except for the phase shift induced the x component.

As it will be important to understand the device presented in next chapter, it is of interest to know the Jones matrix of a polarization phase shifter whose optical axes are rotated an angle θ. The Jones matrix of such a rotated polarization phase shifter is calculated as:

$$\overline{\overline{M_{RPPS}(\Delta\rho,\theta)}} = \overline{\overline{R(\theta)}}\,\overline{\overline{M_{PPS}(\Delta\rho)}}\,\overline{\overline{R(-\theta)}}, \tag{2.19}$$

$$\overline{\overline{M_{RPPS}(\Delta\rho,\theta)}} = \begin{bmatrix} e^{j\Delta\rho}\cos^2\theta + \sin^2\theta & je^{j\Delta\rho/2}\sin\Delta\rho/2\sin 2\theta \\ je^{j\Delta\rho/2}\sin\Delta\rho/2\sin 2\theta & \cos^2\theta + e^{j\Delta\rho}\sin^2\theta \end{bmatrix}. \tag{2.20}$$

Device	Jones Matrix
Horizontal axis polarizer	$\begin{bmatrix} 1 & 0 \\ 0 & 0 \end{bmatrix}$
θ- rotated axis polarizer	$\begin{bmatrix} \cos^2\theta & \cos\theta\sin\theta \\ \cos\theta\sin\theta & \sin^2\theta \end{bmatrix}$
Polarization phase shifter	$\begin{bmatrix} e^{j\Delta\rho} & 0 \\ 0 & 1 \end{bmatrix}$
Polarization rotator	$\begin{bmatrix} e^{j\Delta\rho}\cos^2\theta+\sin^2\theta & je^{j\frac{\Delta\rho}{2}}\sin\frac{\Delta\rho}{2}\sin 2\theta \\ je^{j\frac{\Delta\rho}{2}}\sin\frac{\Delta\rho}{2}\sin 2\theta & \cos^2\theta+e^{j\Delta\rho}\sin^2\theta \end{bmatrix}$
Polarization Converter	$\begin{bmatrix} 0 & 1 \\ 1 & 0 \end{bmatrix}$

Table 2.3.: Jones matrices of different polarization sensitive devices

This matrix is also referred as the Jones matrix of a polarization rotator [23] and, when θ and $\Delta\rho$ are properly chosen, i.e $\theta = \pi/4$ and $\Delta\rho = \pi$, it behaves as a polarization converter, converting the input horizontal/vertical component into the output vertical/horizontal component.

To conclude this subsection, a resume of the Jones matrices described in this section is provided in table 2.3.

2.2.2. The Poincaré sphere

Jones vectors and matrices are very useful to operate with polarization states and polarization sensitive systems. However, they lack a graphical interpretation to keep track of the state of polarization, for example when the lightwave travels through a polarization sensitive system. At this point, the only option is to represent the polarization ellipse of the input and output polarization states. This can be solved using the Poincaré sphere, which represents a single polarization state as a point on the sphere's surface. Consequently, the evolution of the polarization state can be represented as a trajectory on the sphere's surface.

The Poincaré sphere is the 3D projection of the 2D polarization ellipse: On the one hand, any point on a sphere's surface can be defined using two different angles: the longitude, Φ ($-\pi \leq \Phi \leq \pi$), and the latitude, Θ ($-\pi/2 \leq \Theta \leq \pi/2$). On the other hand, a polarization state described by the polarization ellipse is defined using two angles, the orientation angle Ψ ($-\pi/2 \leq \Psi \leq \pi/2$), and the ellipticity angle, $\epsilon(-\pi/4 \leq \epsilon \leq \pi/4)$. Thus, the polarization ellipse can be mapped in a sphere considering that $\Phi = 2\Psi$ and $\Theta = 2\epsilon$. Figure 2.2 a) shows the Poincaré sphere indicating how a polarization state is mapped from its polarization ellipse parameters. In figure 2.2 a), the polarization states of table 2.2 are also shown.

A polarization state expressed in terms of polarization ratio and polarization phase, can also be represented in the Poincaré sphere. For this purpose, we define the polarization ratio constant circumference, which is the locus of SOP in the Poincaré sphere that have the same polarization ratio, i.e. as the blue circumference depicted in figure 2.2 b. This circumference results from the intersection of a polarization ratio constant

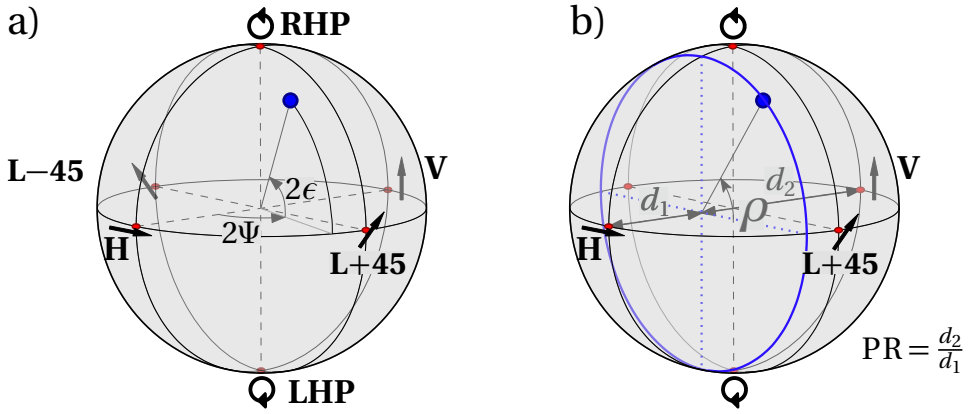

Figure 2.2.: a) Location of polarization states in the Poincaré sphere, based on the polarization ellipse parameters. The polarization states of table 2.2 have been signaled in this sphere. b) Location of a polarization state defined by its PR and its polarization phase (ρ) in the Poincaré sphere.

plane with the Poincaré sphere. The polarization ratio constant plane is defined as a plane whose distance to the V point is polarization ratio times the distance to the H point, so that the intersection with the Poincaré sphere gives SOP with PR = d_2/d_1, as shown in figure 2.2 b). Once the PR circumference is defined, the state of polarization is given by setting the polarization phase angle, ρ, as depicted in figure 2.2 b).

In the following we illustrate the evolution of the polarization state in two different devices: the polarization phase shifter and the polarization rotator, both of them introduced in section 2.2.1.2.

In a polarization phase shifter, whose Jones matrix is given in table 2.3, the SOP keeps its polarization ratio, while a certain polarization phase shift ($\Delta\rho$) is added. Thus, along the propagation through the device, the SOP will stay on a polarization ratio constant circumference, and will experiment an angular displacement of $\Delta\rho$. Figure 2.3 a) shows two cases of SOP evolution in a PPS: The first case shows the evolution of an input SOP which is linear polarization at 45º (a) to right handed circular polarization (b): in this case a 90º polarization phase shift is introduced to the input SOP. The second one is a generic case, in which an arbitrary polarization phase shift, $\Delta\rho$, is induced to an input SOP (c), so that the output SOP is (d).

Regarding the polarization rotator, as its Jones matrix (also provided in table 2.3) depends on two parameters, $\Delta\rho$ and θ, the evolution of the SOP will also depends on these two parameters. The impact of $\Delta\rho$ on the SOP evolution is the same that in the PPS, as it determines total angular displacement of the SOP on the sphere. Regarding θ, it will determine the direction in which the angular displacement is realized. To illustrate this, figure 2.3 b) shows the evolution of the SOP when horizontal polarization is launched into a polarization rotator, for different values of θ and setting $\Delta\rho$ to 180º. Polarization conversion, i.e. horizontal to vertical polarization is achieved for $\theta = \pi/4$ and $\Delta\rho = \pi$.

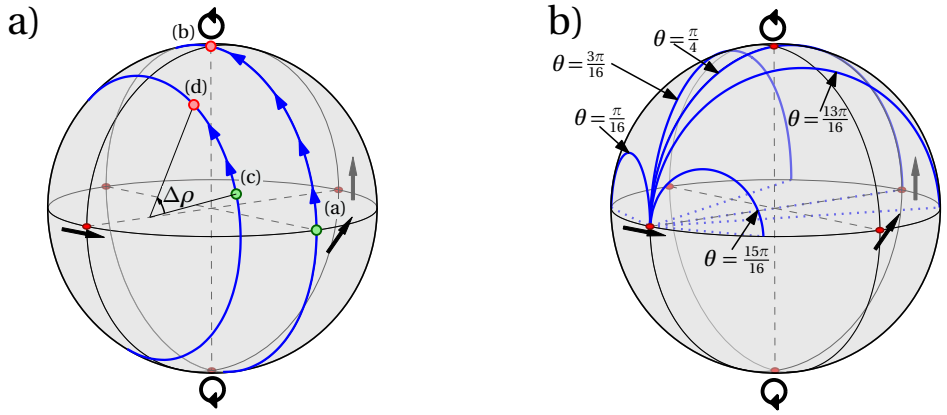

Figure 2.3.: Evolution of the polarization states when a lightwave travels on a polarization phase shifter (a) and a polarization phase shifter with the optical axes rotated θ, (b).

2.2.3. The Stokes parameters

The Stokes parameters constitutes an alternative to the Jones vectors, as they also describe the polarization of a lightwave. However, unlike the Jones vectors, the Stokes parameters are easily measurable. These parameters, denoted by S_0, S_1, S_2, S_3, where proposed by G.G Stokes in 1852 [30]. They are defined in terms of four lightwave observables quantities:

$$\begin{aligned} S_0 &= P_0, \\ S_1 &= 2P_1 - P_0, \\ S_2 &= 2P_2 - P_0, \\ S_3 &= 2P_3 - P_0, \end{aligned} \tag{2.21}$$

where P_0 is the lightwave power, P_1 and P_2 are the power measured when the lightwave passes through a linear polarizer with the transmission axis horizontal and rotated 45º, and P_3 is the power measured when the lightwave passes through a right-handed circular polarizer. Table 2.4 shows the Stokes parameters of common polarization states.

The Stokes parameters are related by the following inequality:

$$S_0^2 \geq S_1^2 + S_2^2 + S_3^2, \tag{2.22}$$

where in the case of totally polarized light (most practical cases) the expression becomes an equality. Furthermore, it is usual to normalize the Stokes parameters to the power of the lightwave, $s_i = S_i/S_0$ with $i = 1,2,3$ so that, the normalized Stokes parameters lie on a sphere of unit radius in the case of totally polarized light:

$$s_1^2 + s_2^2 + s_3^2 = 1. \tag{2.23}$$

These three Stokes parameters (or its denormalized version) are grouped together in a Stokes Vector, that defines the state of polarization of a lightwave: $\mathbf{V} = (s_1, s_2, s_3)'$

Polarization	Stokes Parameters	
Linear Horizontal / Linear Vertical	$\begin{bmatrix} 1 \\ 1 \\ 0 \\ 0 \end{bmatrix}$	$\begin{bmatrix} 1 \\ -1 \\ 0 \\ 0 \end{bmatrix}$
Linear 45º / Linear -45º	$\begin{bmatrix} 1 \\ 0 \\ 1 \\ 0 \end{bmatrix}$	$\begin{bmatrix} 1 \\ 0 \\ -1 \\ 0 \end{bmatrix}$
Right Handed Circular/Left Handed Circular	$\begin{bmatrix} 1 \\ 0 \\ 0 \\ 1 \end{bmatrix}$	$\begin{bmatrix} 1 \\ 0 \\ 0 \\ -1 \end{bmatrix}$

Table 2.4.: Stokes Parameters of the main states of polarization

The Stokes parameters can also be defined in terms of the polarization ellipse parameters as follows:

$$\begin{aligned} S_0 &= P_0, \\ S_1 &= P_0 \cos(2\epsilon)\cos(2\Psi), \\ S_2 &= P_0 \cos(2\epsilon)\sin(2\Psi), \\ S_3 &= P_0 \sin(2\epsilon), \end{aligned} \tag{2.24}$$

where it can be observed that in the case of normalized power, they match the sphere equation. Furthermore, it can be observed that the relation between the Stokes parameters and the polarization ellipse parameters, is similar to the relation between cartesian and spherical coordinates. Thus, the elements of a normalized Stokes vector, constitute the 3 axes of the Poincaré sphere and, provided that the Stokes parameters are related through the equation of a sphere, they will lay on the Poincaré sphere surface when they are represented in a 3D space, as shown in figure 2.4.

2.2.4. Polarization of light in integrated optics

In the previous sections, the general formalisms describing the polarization of a lightwave have been provided. These formalisms, developed in the XX century, were conceived for free space optics. However, they can also be used to describe the state of polarization of a lightwave propagating in an integrated optical waveguide. In the following, the basic polarization characteristics of the integrated optical waveguides are discussed.

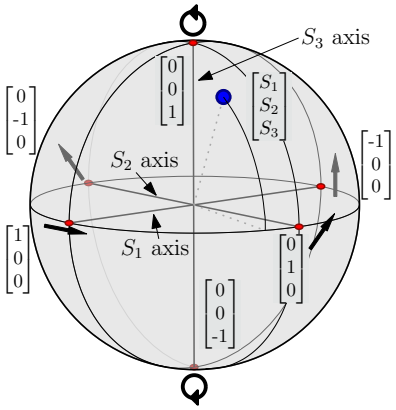

Figure 2.4.: Stokes vectors representation on the Poincaré sphere. As can be observed, the Stokes parameters defines the 3D axes of the Poincaré sphere

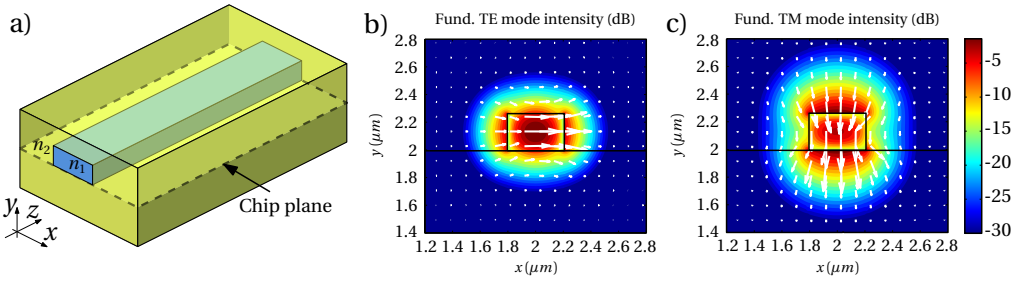

Figure 2.5.: a) A strip waveguide, where light is confined in the blue high refractive index region. Considering the silicon-on-insulator platform at λ 1.55µm, n_1 3.476 and n_2 1.444. Intensity and direction of the electric field of the quasi-TE mode (b) and quasi-TM mode (c) of the strip optical waveguide.

One of the simplest integrated guiding structures is the strip waveguide, depicted in figure 2.5 a). The electric field in the waveguide can be expressed as a linear combination of the supported modes:

$$\mathbf{E}_{\text{total}}(x,y,z) = \sum_{i=0}^{n} c_i \phi_{\mathbf{i}}(x,y) e^{j\beta_i z}, \tag{2.25}$$

where c_i models the excitation of each mode, $\phi_{\mathbf{i}}$ is the mode profile, and β_i is the mode propagation constant. When Maxwell equations are solved in a rectangular waveguide, two families of modes are found: the quasi transverse electric (quasi-TE) modes or TE modes, whose main electric field component is in the x direction, and the quasi transverse magnetic (quasi-TM) modes or TM modes, whose main electric field component is in the y direction [31]. The number modes supported in a waveguide will depend on the waveguide geometry, i.e. height and width, and the operation wavelength. In most cases these waveguides are designed to operate in monomode condition so that only the fundamental modes of each family, depicted in figures 2.5 b) and c), propagate. In that case, assuming that for the TE mode $E_x \gg E_z, E_y$ and for the TM mode $E_y \gg E_z, E_x$, the electric field propagation along the strip waveguide can be expresed as:

$$\mathbf{E}_{\text{total}}(x,y,z,t) = c_{TE}\phi_{TE}(x,y)e^{j(\omega t-\beta_{TE}z)}\hat{\mathbf{x}} + c_{TM}\phi_{TM}(x,y)e^{j(\omega t-\beta_{TM}z)}\hat{\mathbf{y}}, \tag{2.26}$$

that is analogous to expression 2.1 except for the propagation constants. Since the propagations constants are generally different for TE and TM modes, the waveguide behaves like an anisotropic medium. Thus all the the Jones and Stokes formalism described above can be applied considering the fundamental TE and TM mode of the strip waveguide instead of the x and y components of a lightwave. The optical axes in an integrated waveguides are usually defined using the chip plane, as shown in figure 2.5 a). Thus, in integrated optics, the horizontal polarization (x axis) is usually named TE polarization or in-plane, while the vertical polarization (y axis) is named TM polarization or out-of-plane.

Common polarization sensitive system can be implemented in integrated optics. For example, an horizontal polarizer can be implemented using a waveguide that only supports the TE mode. A polarization phase shifter can be implemented with a strip waveguide whose propagation constant are different for the fundamental TE and TM modes, i.e. a birefringent waveguide. In order to implement polarization rotators, it is of fundamental importance to break the symmetry of the whole guiding structure, this can be done for example using asymmetric waveguides [32], or using asymmetric coupled waveguides with different cladding and bottom materials [33].

In the next sections, a further detailed description of the the state of the art of integrated polarization phase shifters and polarization rotators is provided.

2.3. Polarization Phase Shifters in integrated optics

In a monomode waveguide, only the fundamental TE and TM modes propagate. As previously mentioned, in the general case, each fundamental mode will have a different propagation constant (β_{TE}, β_{TM}) and consequently, provided that $\beta = 2\pi n/\lambda$, a

different effective index, (n_{TE}, n_{TM}). The difference between these effective indexes, $\Delta n = n_{\mathrm{TE}} - n_{\mathrm{TM}}$, is defined as the birefringence of the waveguide.

The birefringence of an integrated waveguide is determined by the anisotropy of the material of which the waveguide is made of and from the waveguide geometry itself. The former is a consequence of the orientation of the molecules composing the material, so that at macroscopic scale refractive index has a dependence on the light polarization, while the later results from the different boundary conditions that the waveguide cross-sectional geometry imposes to the TE and TM modes. Thus, in both cases, the Jones matrix that describes the propagation along a birefringent waveguide of length L, $\overline{\overline{M_{\mathrm{BW}}}}$, is given by

$$\overline{\overline{M_{\mathrm{BW}}(\Delta n, L, \lambda)}} = \begin{bmatrix} e^{j\frac{2\pi L\Delta n}{\lambda}} & 0 \\ 0 & 1 \end{bmatrix}, \tag{2.27}$$

that coincides with the Jones matrix of a polarization phase shift in which:

$$\Delta\rho = \frac{2\pi L\Delta n}{\lambda}. \tag{2.28}$$

In many photonics integrated applications, it is more interesting to have tunable polarization phase shifters (TPPS), rather than a static polarization phase shifter. Two main approaches are found in the literature to implement TPPS: by altering the anisotropy of the waveguide core material or by changing the refractive index of the materials in the waveguide core or cladding.

The first approach relies on the tunable anisotropy of materials such as Lithium Niobate ($LiNbO_3$) [34, 35] or nematic liquid crystals [36]. In these materials, the orientation of the molecules is modified by applying an external electric field. Consequently the effective index of the propagating TE and TM modes propagating will change, and thus the polarization phase will be shifted as a function of an applied voltage.

The second approach relies on the different profile of the fundamental TE and TM modes in integrated waveguides. Thus, a change in the refractive index of the different isotropic materials will have a different impact in each mode. The change in the refractive index can be realized for example by directly applying an electric field [37], or by heating the structure [38, 39].

A common figure of merit of the polarization phase shifters, appart from its compactness, is its V_π, defined in this context as the required voltage increment to shift by π rad the SOP phase. Table 2.5 shows some of common tunable polarization phase shifters found in the literature, also known as birefringence controllers or birefringence modulators.

2.4. Polarization Rotation in integrated optics

The birefringence of a given photonic waveguide is an useful characteristic, for example, to implement polarization phase shifters. However, in other applications it may turn into a drawback, as it makes devices polarization sensitive. This polarization sensitivity is particularly significant in high index photonics platforms such as

Ref.	Technology	V_π (V)	Length (mm)	Power (mW)
[35]	$LiNbO_3$	23 V	7	NA
[34]	$LiNbO_3$	23 V	10	NA
[38]	Polymer	3.7	5	70
[37]	InP	1.2	1.8	5.4

Table 2.5.: Main characteristics of TPPS found in the literature

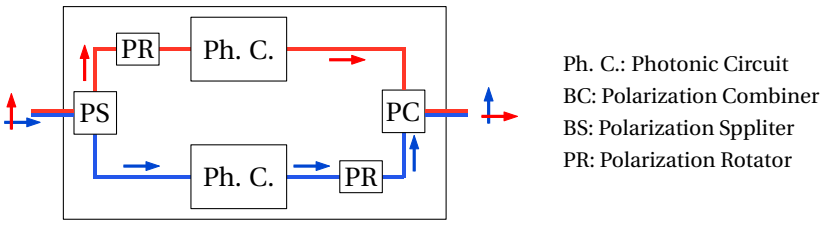

Figure 2.6.: Polarization diversity scheme proposed in [40]. Using this scheme, polarization transparent operation can be achieved, even if the photonics circuits are polarization sensitive. The arrows depict the orientation of the electric field, while the color represent the information carried in each component.

Silicon-On-Insulator. Designers struggle to come up with polarization insensitive devices, that eventually require highly accurate fabrication processes, making these devices unpractical [40]. However, using a polarization diversity scheme an overall polarization independent behavior can be obtained with polarization sensitive devices, as depicted in figure 2.6. A key element in these scheme is the polarization rotator, that transforms TE/TM polarization into TM/TE polarization. Polarization rotators are also a key element in optical dual-polarization coherent communications to provide the polarization multiplexation of the information.

In this subsection, the different integrated approaches used to rotate the state of polarization of light are shown. For the sake of clarity, they are arranged in five different groups: mode evolution based rotators, cross-polarization coupling based rotators, high-order mode evolution based rotators, rotator waveguide sections and periodic loaded asymmetric waveguides.

To compare the different approaches, five figures of merit are employed: on one side, for mode evolution based rotators, rotator waveguide sections and periodic loaded asymetric waveguides, insertion losses (IL), polarization conversion efficiency (PCE) and extinction ratio (ER) are defined, on the other side, for cross-polarization coupling based rotators and high-order mode evolution based rotators the polarization conversion losses (PCL) and the crosstalk are defined.

The insertion losses is defined as the power that is wasted in the polarization conversion:

$$\mathrm{IL\,(dB)} = 10\log_{10}\left(\frac{P_{in}}{P_{out}}\right), \tag{2.29}$$

where P_{in} and P_{out} is the total power in both polarizations, at the input and the output, respectively.

The extinction ratio is defined as the ratio between the power in the desired polarization at the output of the device P_d and the power in the undesired polarization state P_{ud}, as follows:

$$\mathrm{ER} = \frac{P_d}{P_{ud}}. \tag{2.30}$$

The polarization conversion efficiency is defined as the ratio between the desired polarization at the output of the device, and the total power as follows:

$$\mathrm{PCE}\,(\%) = \frac{P_d}{P_{ud} + P_d} \times 100, \tag{2.31}$$

furthermore, the PCE is usually defined in terms of the polarization rotator Jones matrix:

$$\mathrm{PCE}\,(\%) = \left|J_{21}(\theta, \Delta\rho)\right|^2 = \sin^2(2\theta)\sin^2(\Delta\rho/2). \tag{2.32}$$

Both polarization conversion efficiency and extinction ratio are related with the degree of conversion of the input polarization, so they can be related as follows:

$$\mathrm{PCE} = \frac{\mathrm{ER}}{1 + \mathrm{ER}}. \tag{2.33}$$

Regarding the crosstalk and the PCL, they are analogous to the already defined figure of merits, with some differences emerging from the nature of these devices, that rotate and separate polarization simultaneously. The PCL is defined as the fraction of power that is converted from TE or TM at the input to TM or TE at the output:

$$\mathrm{PCL} = \max\left\{10\log_{10}\left(\frac{\mathrm{P}_{\mathrm{out}}^{\mathrm{TE}}}{\mathrm{P}_{\mathrm{in}}^{\mathrm{TM}}}\right), 10\log_{10}\left(\frac{P_{out}^{TM}}{P_{in}^{TE}}\right)\right\} \tag{2.34}$$

The crosstalk is analogous to the ER however, as these devices have two output waveguides, it is more usually to use the crosstalk, defined as the fraction of power in the undesired SOP in each of the output waveguides:

$$\mathrm{Crosstalk}\,(\mathrm{dB}) = 10\log_{10}\left(\frac{\mathrm{P}_{\mathrm{out}}^{\mathrm{TE,TM}}}{\mathrm{P}_{\mathrm{out}}^{\mathrm{TM,TE}}}\right) \tag{2.35}$$

2.4.1. Mode-evolution based integrated polarization rotation

The principle of operation of mode-evolution-based integrated polarization rotator relies on the gradually rotation of the integrated waveguide optical axes. In this way, as the optical axis rotate, the polarization of the light propagating along the structure will rotate.

A mode-evolution based polarization rotator can be implemented by shaping the cross geometry of an integrated waveguide along the propagation direction, as depicted in figure 2.7 [41]. This structure, under adiabatic transition conditions, behaves as a polarization rotator transforming the TM mode of the input waveguide into the TE mode of the output waveguide. The operation of this device is improved for longer

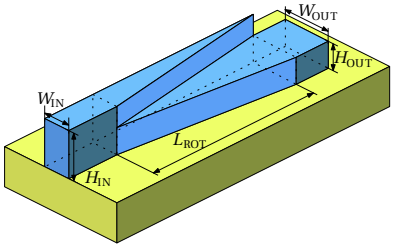

Figure 2.7.: a) Mode evolution based polarization rotator

Ref.	Year	Technology	Fab.	ER (dB)	IL (dB)	L (µm)	BW (nm)
[41]	2005	SiN	No	22	NA	200	300
[42]	2010	SOI	Yes	15	3	40	40
[43]	2011	SiN SOI	Yes	20	1	300	80
[44]	2012	SOI	Yes	14	0.5	100	70
[45]	2013	SOI	No	32	0.14	6	40
[46]	2014	SOI	No	22	0.16	27	40
[47]	2015	SOI	Yes	20	0.5	300	200

Table 2.6.: Mode Evolution based polarization rotators

transition regions and for input and output waveguides with a high aspect ratio, i.e. W/H.

These polarization rotators are poorly tolerant to fabrication deviation, as they require an accurate fabrication of the transition region and a two etch step process. They are mostly implemented in Silicon based platform. Their main benefit is that they can offer a low-loss polarization rotation in a relatively wide bandwidth by sacrifiyng the device compactness. Finally, table 2.6 shows the polarization rotators following this approach, that have been found in the bibliography.

2.4.2. Cross-polarization coupling based integrated polarization rotation

To achieve polarization rotation it is necessary to break the symmetry of the guiding structure both vertically and horizontally, as previously mentioned. In cross polarization couplers, the vertical symmetry is broken by using different top and bottom materials, i.e. air as cladding material and SiO_2 as bottom material. The horizontal symmetry is broken by placing close together two parallel waveguides with different widths, as depicted in 2.8 a). In such geometry light is coupled between the modes of the two different waveguides when the phase matching condition is fulfilled, i.e. the mode effective index, considering the isolated waveguides, are equal. In this way, when effective index of the TM mode in one waveguide equals the effective index of the TE mode in the other waveguide, light couples from TM to TE, performing the polarization rotation.

As an example, figure 2.8 b) shows, as a function of the waveguide width, the effective index of the modes propagating in a SOI waveguide whose height is assumed

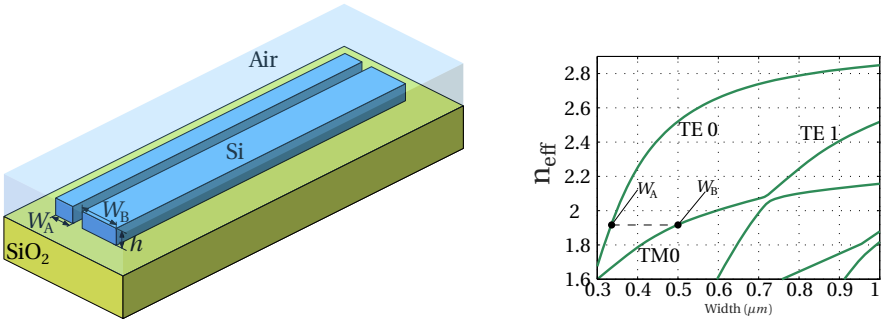

Figure 2.8.: a) Cross-polarization coupling based integrated polarization rotator as proposed in [48]. b) Effective index of the modes propagation in a SOI waveguide whose height is 260 nm and considering air as cladding material.

to be 260 nm and assuming air as a cladding material. It can be observed that the TM mode effective index for a width of $W_B = 0.5\mu m$ equals the effective index of the fundamental TE mode for a width around $W_A = 0.34\mu m$. Consequently, if those waveguides are used to implement the waveguides of the device depicted in 2.8 a), polarization rotation can be achieved. The length of such a rotator can be calculated from the propagation constant of the coupling waveguide hybrid supermodes, that are depicted in figure 2.9. As can be observed, these supermodes have significant field in both x and y polarization components. Thus, polarization rotation is achieved when these modes are shifted π rad, i.e. at the beat length of the structure, defined as:

$$L_\pi = \frac{\pi}{\beta_{HS1} - \beta_{HS2}}, \tag{2.36}$$

where β_{HS1} and β_{HS2} are the propagation constant of the hybrid supermodes.

This device operate as follows: when waveguide A is excited with its fundamental TE mode, it will couple to the TM mode of waveguide B. Similarly, when the structure is excited with the fundamental TM mode of waveguide B, it will couple to the TE mode of waveguide A. However, when TE is injected into the wide waveguide or TM is injected in to the narrow waveguide, they will not couple to the other waveguide as the effective index are different and phase matching condition is not satisfied.

Cross-polarization couplers cannot be used as a pure polarization converter as the separation of the polarization is inherent to its operation principle. However they achieve polarization rotation in a compact device that can be fabricated using single step etching processes, usually implemented in the SOI platform. Furthermore, the bandwidth of these devices is around 40 nm. The main drawback of these devices is the need of using a cladding material different from the BOX to break the vertical simmetry of the waveguide structure [49].

This mechanism to achieve polarization rotation was first proposed by Liu et al. in [48]. Since then, some alternatives that improve the tolerances [50], or the compactness [51], have been proposed. Table 2.7 shows the main characteristics of the different proposed alternatives following this approach.

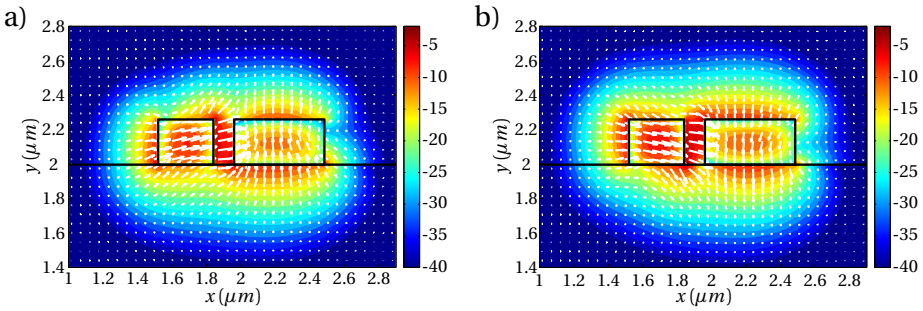

Figure 2.9.: Intensity and direction of the electric field of the hybrid supermodes of a Cross-polarization coupling based integrated polarization rotator.

Ref.	Year	Technology	Fab.	PCL (dB)	Crosstalk (dB)	L (μm)	BW (nm)
[33]	2011	SOI	Yes	-0.6	NA	44	40
[48]	2011	SOI	Yes	-0.6	12	36.8	50
[52]	2012	SOI	Yes	-0.45	NA	140	60
[53]	2012	SOI	No	-0.22	18	17.4	45
[54]	2014	SOI	Yes	-0.31	25	27	30
[50]	2014	SOI	No	-0.13	15	25	40
[55]	2014	SOI	No	-0.1	30	200	160
[56]	2015	SOI	No	NA	25	300	100
[56]	2015	SOI	No	NA	30	400	300
[57]	2015	SOI Plasmonic	No	-0.13	NA	11.2	60
[58]	2016	SOI	Yes	-0.32	12,5	35	50
[59]	2016	SOI	No	-0.5	22	19.6	50
[60]	2016	Si_3N_4+Si	Yes	-0.132	20	50	50
[61]	2016	SOI	No	-0.11	27	80	50
[51]	2016	SOI	No	-0.08	20	9.2	10
[62]	2016	SOI	Yes	-0.13	20	8.77	41
[63]	2017	SOI	Yes	-0.41	18	80	50

Table 2.7.: Cross polarization coupling based polarization rotators

2.4.3. High-order mode-evolution based integrated polarization rotation

Firstly proposed by Dai et al. in [64], this approach makes use of a mode evolution technique to convert the input TM mode into the second order TE mode (TE1). Then some coupling mechanism is used to convert the TE1 into the fundamental TE mode (TE0). Most of the approaches in the literature use either an asymmetrical directional coupler or a waveguide bent to convert the TE1 mode into the TE0 mode.

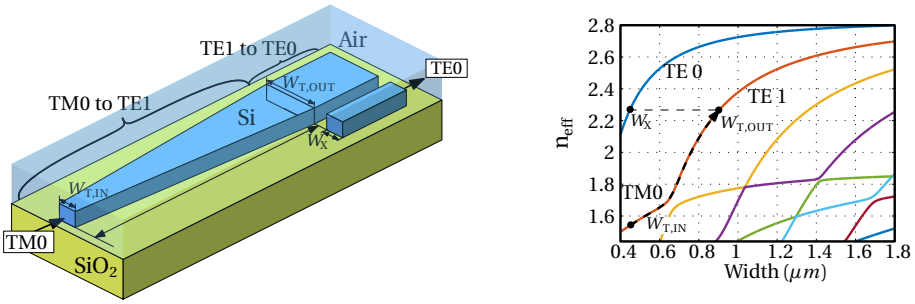

Figure 2.10.: a) High-order mode-evolution based integrated polarization rotator as proposed in [64]. b) Effective index of the modes propagation in a SOI waveguide whose height is 220 nm and considering air as cladding material.

The implementation of the device proposed in [64] is schematically depicted in figure 2.10 a). Thus, in the first part of the device, an adiabatic taper is used to transform the fundamental TM mode into the second order TE mode, taking advantage of the mode hybridization that is produced when the vertical symmetry is broken in such structure [49]. To better understand this mode conversion mechanism figure 2.10 b) shows the mode effective indices as a function of the waveguide width (in this example, a SOI waveguide whose height is 220 nm using air as cladding material, is considered). In this figure it can be observed that, as the waveguide width increases, the fundamental TM mode is converted to the second order TE mode so, by gradually varying the width of the taper from $W_{T,IN} = 0.45\mu m$ to $W_{T,OUT} = 0.86\mu m$, the TM mode is adiabatically transformed into the TE1 mode.

In the depicted scheme, the last region of the device implements an asymmetrical directional coupler, but a bent waveguide could be used instead [65]. In that coupler, the waveguide widths are chosen so that TE1 couples to the TE0 mode of the adjacent narrow waveguide. For example, by regarding figure 2.10 b), it can be noticed that TE1 mode of the wider waveguide will match the phase of the narrow waveguide TE0 for a width of $W_{T,OUT} \approx 0.4\mu m$.

Thus, the launched TM polarization will result in TE polarization at the cross output. Conversely, when TE polarization is injected in the device, there is no mode conversion at all and TE polarization is obtained in the through output.

As with cross-polarization couplers, this polarization rotation device it is not a pure polarization rotator, as it also separates the orthogonal polarization states. It is less compact than the cross-polarization coupling approaches, and its bandwidth is usually limited by the TE1 to TE0 converter, being higher than the bandwidth of cross polarization coupling approaches. Most of the presented approaches are either pro-

posed or fabricated in the SOI platform, as its high contrast eases the TM-TE1 conversion. Regarding the fabrication, this approach presents good fabrication tolerances, but as it occurs with cross-polarization coupling approaches it requires to break the vertical symmetry, which implies either to use a cladding material different from the substrate or use ridge guiding structures. Finally, table 2.8 shows the polarization rotators found in the bibliography that follows this approach.

Ref.	Year	Technology	Fab.	PCL (dB)	Crosstalk (dB)	L (μm)	BW (nm)
[64]	2011	SOI	No	0,04	NA	71	130
[66]	2012	InP	No	0,51	25	1350	84
[67]	2013	SOI	Yes	0,22	12	140	100
[68]	2014	SOI	No	0,11	25	15,3	80
[69]	2014	SOI	Yes	0,46	12	580	50
[70]	2014	SOI	Yes	1,55	19	650	80
[71]	2014	SOI	No	0,46	17	220	40
[72]	2015	SOI	No	0,27	18	470	400
[73]	2016	SOI	No	0,18	16	240	300
[74]	2016	SOI	No	0,2	35	100	200
[75]	2016	SOI	Yes	0,51	NA	71	50
[65]	2017	SOI	Yes	0,81	19,8	20	80

Table 2.8.: High-order mode evolution based polarization rotators

2.4.4. Rotator waveguide sections

A rotator waveguide section (RWS) is, essentially, a photonic waveguide whose horizontal and vertical symmetries are broken. To break the waveguide symmetry different alternatives have been proposed in the literature: using waveguides with a slanted sidewall [76], partially etching the waveguide [77] or even introducing several subwavelength trenches in the waveguide [78], as depicted in figures 2.11 a), b) and c), respectively.

When the symmetry of the waveguide is properly broken, the waveguide will not support TE and TM modes, but two orthogonal hybrid modes, H_1 and H_2. The main field components of these hybrids modes are tilted $+45°$ and $-45°$ from the optical axis, as depicted in figure 2.11 d) and e), where the hybrid modes supported by the waveguide depicted in figure 2.11 c) are shown. To achieve perfect polarization rotation, i.e. transforming TE to TM or vice-versa, the length of the rotator is set to the beat length of the two hybrid modes, L_π, defined as:

$$L_\pi = \frac{\pi}{\beta_{H1} - \beta_{H2}} \tag{2.37}$$

where β_{H1} and β_{H2} are the propagation constants of the hybrid modes H_1 and H_2.

A rotator waveguide section (RWS) is placed between two conventional waveguides. Thus, when the TE or TM mode of the input waveguide is injected into the RWS, it will equally excite both hybrid modes. The hybrid modes will then propagate along the rotator waveguide section with different propagation constants, continuously changing

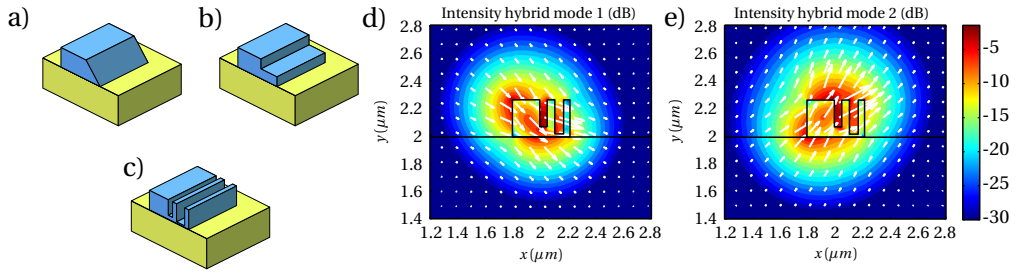

Figure 2.11.: Rotator waveguide sections implemented with a slanted sidewall (a), by partially etching the waveguide (b) and by introducing two subwavelength trenches in the waveguide (c). d) and e) are the hybrids modes of the waveguide schematically depicted in (c).

the polarization state. If the rotator length is set to L_π, at the end of the rotator waveguide section TM or TE mode will be coupled to the output waveguide. Unlike the approaches presented in the previous sections, RWS can be simply modeled using the Jones matrix of a polarization rotator, reproduced here for the sake of clarity:

$$\overline{\overline{J_{\mathrm{RWS}}}}(\theta,\Delta\rho)=\begin{bmatrix} e^{j\Delta\rho}\cos^2\theta+\sin^2\theta & je^{j\varphi/2}\sin\Delta\rho/2\sin2\theta \\ je^{j\Delta\rho/2}\sin\Delta\rho/2\sin2\theta & \cos\theta+e^{j\Delta\rho}\sin^2\theta \end{bmatrix} \tag{2.38}$$

This matrix was defined in terms of two parameters, the optical axis tilt, θ, and the phase shift, $\Delta\rho$. These parameters can be easily calculated from the hybrid modes of the RWS. The optical axis rotation angle can be directly calculated from the electric field of the hybrid modes as follows [39]:

$$\theta=\arctan\left(\frac{\iint_\Omega |E_y|^2\,d\Omega}{\iint_\Omega |E_x|^2\,d\Omega}\right) \tag{2.39}$$

Regarding the phase shift, it is defined as a function of L_π, calculated from the hybrid mode propagation constants, and the length of the rotator waveguide section, L_R:

$$\Delta\rho=\frac{L_\mathrm{R}}{L_\pi}\pi \tag{2.40}$$

This polarization rotation device is usually more compact than the previous approaches, and they have been demonstrated in both silicon and indium phosphide platforms, as shown in table 2.9, where the polarization rotators following this approach, found in the literature, are shown. However, as polarization rotation is achieved interferometrically the bandwidth is rather small. The drawbacks of this approach are the tolerance to fabrication deviations, which is very low and the complexity of the required fabrication process, as in most approaches more than one etch step is required.

Ref.	Year	Technology	Fab.	ER (dB)	IL (dB)	L (μm)	BW (nm)
[79]	1996	GaAs-AlGaAs	No	20	2,5	250	NA
[80]	1996	GaAs-AlGaAs	Yes	7,5	NA	975	NA
[81]	2000	GaAs-AlGaAs	Yes	13,8	0,87	720	NA
[82]	2001	GaAs-AlGaAs	No	20	0,4	320	NA
[83]	2005	InGaAs-InP	No	14	1,3	2	200
[78]	2006	GaAs-AlGaAs	Yes	13,8	0,6	150	NA
[84]	2007	InGaAsP-InP	Yes	15	2,5	291	35
[85]	2008	SOI	Yes	11	1	35	12
[77]	2008	SOI	No	15	0,2	22,5	120
[86]	2009	GaAs-AlGaAs	Yes	6	NA	156	NA
[87]	2009	InGaAs-InP	Yes	95	0,09	210	80
[32]	2012	InP	No	40	0,04	924	35
[88]	2012	SOI	Yes	16	0,7	10	26
[89]	2012	SOI	Yes	9	NA	7	80
[90]	2012	SOI Plasmonic	No	15	2,1	NA	150
[91]	2012	SOI	Yes	6,65	1,75	25	30
[92]	2013	InGaAs-InP	Yes	14	0,1	150	65
[93]	2013	SOI	Yes	13,3	2	4,2	200
[94]	2013	SOI	No	40	0,5	NA	110
[95]	2013	SOI Plasmonics	No	22,4	1,38	3,2	100
[96]	2014	SOI Plasmonics	No	15	0,7	15,2	67
[97]	2014	SOI Plasmonics	No	25,2	2,2	9,7	200
[98]	2014	SOI	No	35	0,15	52,8	60
[72]	2015	NA	No	20	0,4	19	230
[99]	2015	SOI Plasmonics	Yes	11	0,5	10	10
[100]	2015	SOI	Yes	30	NA	23	40
[101]	2016	SOI	No	NA	0,4	7,92	100
[102]	2016	SOI	No	27	0,28	3,3	250
[103]	2016	SOI	Yes	21,1	2,1	67	15
[104]	2016	InGaAsP-InP	Yes	20	NA	700	40

Table 2.9.: Rotator waveguide section polarization rotators

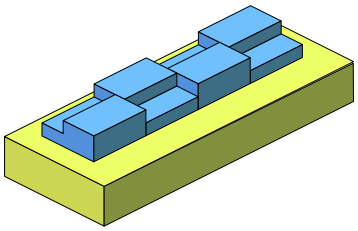

Figure 2.12.: Polarization rotator implemented using periodic loaded asymmetric waveguides

2.4.5. Periodic loaded asymmetric waveguides

These polarization rotation devices are composed of a periodic arrangement of rotator waveguide sections, as depicted in figure 2.12. As can be observed, in the periodic arrangement, the RWS are alternatively mirrored in the horizontal direction. This mirroring would impact on the optical axis rotation angle, being θ and $-\theta$ alternatively. In this device, when the length of each section is set to L_π, the phase matching condition is met and the amount of rotation angle in each section adds constructively [105].

The principle of operation of these devices, can be understood through the Jones matrix of the each RWS. Thus, if the phase matching condition announced in [105] is met, then $\Delta\rho = \pi$. In that case the Jones Matrix of each RWS reads:

$$\overline{\overline{J_{RWS}}}(\theta,\pi) = \begin{bmatrix} \sin^2\theta - \cos^2\theta & \sin 2\theta \\ \sin 2\theta & \cos^2\theta - \sin^2\theta \end{bmatrix} \tag{2.41}$$

Considering the periodic rotator (PR) as the concatenation of N RWS, with alternate optical axis rotation angle, its Jones matrix is given:

$$J_{PR}(N,\theta) = J_R((-1)^{N-1}\theta,\pi)\cdot\ldots\cdot J((-1)^0\theta,\pi) \tag{2.42}$$

Multiplying these matrices and simplifying, the Jones matrix for N consecutive sections can be derived:

$$J_{PR}(N,\theta) = \begin{bmatrix} (-1)^N\cos(2N\theta) & (-1)^{N+1}\sin(2N\theta) \\ \sin(2N\theta) & \cos(2N\theta) \end{bmatrix} \tag{2.43}$$

This matrix, when $2N\theta = \pi/2$ is the matrix of a polarization converter, that was shown in section 2.2.1. Thus, this approach makes perfect polarization rotation feasible even if the RWS do not support 45° tilted hybrid modes, provided that $\theta > 0$.

This approach may result of strong interest in platforms where the technology does not allow to implement RWS with 45° tilted hybrid modes, as occurred in the early days of the fabrication process technologies. Thus, the main advantage of these polarization rotation devices, is that perfect polarization can be achieved in absence of 45° tilted hybrid modes. However, they are longer than non-periodic counterparts and, due to the reflection at the interface of different sections, they may exhibit high insertion losses. As it occurs with the rotator waveguide section, they were first demon-

Ref.	Year	Technology	Fab.	ER (dB)	IL (dB)	L (μm)	BW (nm)
[105]	1991	InP	Yes	99	2,5	3700	20
[106]	1992	InGaAsP-InP	Yes	50	3	825	60
[107]	1992	Proof	No	NA	NA	3153	NA
[108]	1995	InP	Yes	90	NA	1080	NA
[109]	1998	K-Na on glass	Yes	99	0,4	18000	NA
[110]	2001	SiON	Yes	98	3	12000	NA
[111]	2012	InP	Yes	99	1,2	10	NA
[112]	2015	SOI	Yes	27	1	294,4	2,63
[113]	2016	SOI	Yes	93	1,1	15,78	40

Table 2.10.: State of the art of polarization rotators based on periodic loaded asymmetric waveguide

strated in InP platforms, and have been recently proposed on SOI. Table 2.10 shows the polarization rotators based on this approach that have been proposed until now.

3
Integrated polarization control

3.1. Introduction

One of the main applications of controlling the polarization state of light is found in telecommunications. In that context, polarization multiplexing constitutes a cost-effective way to double the capacity of the optical fiber links. As polarization arbitrarily changes along the propagation in the fiber, polarization control was required at the origin of polarization multiplexing optical coherent receivers to unscramble these arbitrary changes, so that the received signal polarization matches the SOP of the local oscillator for maximum interference [114]. Since then, polarization control has found a great variety of applications: it is used in microwave photonics signal processing to implement negative coefficient filters [115]; in optical coherent tomography, providing polarization sensitive imaging that allows to differentiate different organic tissues [14], and it has also been introduced in quantum communications systems, to implement devices for quantum key distribution [15].

Polarization controllers have been successfully implemented in fiber optics, taking advantage of the strain-induced optical birefringence [116]. However, in comparison with its integrated counterparts, they lack the potential of being compact and maintaining an improved stability. Integrated approaches have been successfully demonstrated in $LiNbO_3$ technology [117], but they are not suitable for large scale fabrication, due to their high fabrication cost. In other integrated platforms, such as InP or SOI, the integration becomes challenging due to the high sensitivity to fabrication imperfections of the polarization managing devices, i.e. polarization beam splitters and polarization rotators.

Most of the polarization controllers proposed to date rely on the architectures depicted in figure 3.1. The first architecture, depicted in figure 3.1 a), makes use of polarization beam splitters and combiners and polarization rotators, among others elements. This approach was first proposed in [118] and has been demonstrated in different platforms. The weak point of this architecture is that the performance of the whole device is limited by the performance of the polarization managing elements thus presenting low tolerances to fabrication deviations.

The second architecture, presented in figure 3.1 b), is simpler as only requires two polarization rotators and three tunable polarization phase shifters. For this scheme to work properly, polarization rotators with a PCE of exactly 50% are required. Thus, the

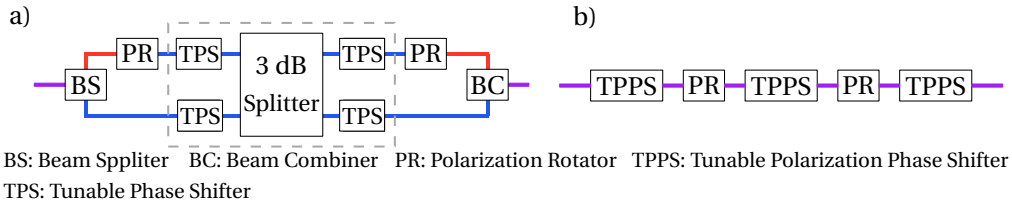

Figure 3.1.: Common schemes used to implement integrated polarization controllers. a) Polarization controller based on beam sppliters and combiners, polarization rotators and tunable phase shifters. b) polarization controller based on polarization rotators and tunable polarization phase shifters. In a) the subsystem in the dashed box can be replicated several times.

operation of the whole device is again hindered by the tolerances of the polarization rotators.

In addition to these polarization controller schemes another approach, based on quantum effects at a macroscopic scale has been proposed, but it requires out-of-plane waveguides [119], which are challenging to fabricate.

In this chapter a fully integrated polarization controller that achieves state-of-the-art performance, in a compact and integrable device is shown. Furthermore, the proposed device shows remarkable tolerances to fabrication deviations. In section 3.2 the device's architecture and principle of operation is shown. Then, in section 3.3 the implementation of the device is outlined. Finally, section 3.4 will be devoted to the characterization of the device.

3.2. Architecture and principle of operation

The proposed scheme is inspired in the well known manual fiber polarization controllers, as the depicted in figure 3.2 a). These controllers use stress-induced birefringence to realize three different rotatable wave-plates, each one implemented by looping an optical fiber around a spool. Thus each wave-plate behaves as a rotator waveguide section, with a fixed $\Delta\rho$ (polarization phase shift) and adjustable θ(optical axis rotation angle), as schematically depicted in 3.2 a). These fiber polarization controllers guarantee the full coverage of the Poincaré sphere by adjusting the rotation angle of each wave-plate. It has to be mentioned that manual fiber polarization controllers using only two paddles have also been proposed but they have stronger requirements on each paddle to work properly.

In integrated platforms, such as SOI, the rotation angle of the rotator waveguide section (RWS) is fixed once the device is fabricated, so a faithful integrated version of the manual fiber polarization controller is unfeasible. However, equivalent operation can be achieved by means of rotator waveguide sections with fixed rotation angles and tunable polarization phase shifters (TPPSs). As it will be shown below, an integrated polarization controller scheme covering the whole Poincaré sphere can be implemented by means of three pairs of RWSs and TPPSs arranged as depicted in figure 3.3 a).

In this scheme RWS with fixed θ and $\Delta\rho$ will change the polarization ratio (PR)

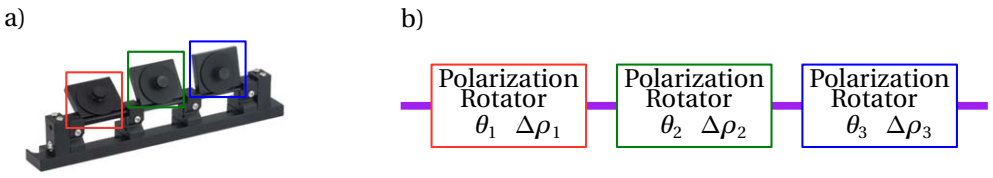

Figure 3.2.: a) Manual fiber polarization controller. b) Systemic model of the manual fiber polarization controller using polarization rotators with different $\Delta\rho$ and θ

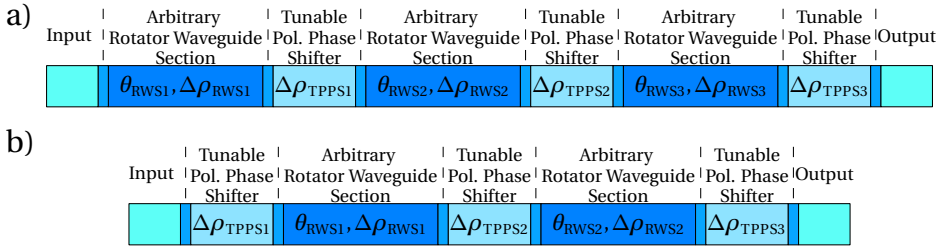

Figure 3.3.: a) Proposed polarization controller scheme. b) Polarization controller scheme proposed in the literature [120, 121].

of the polarization state, and to some extent the polarization phase. On the other side, each TPPS will introduce a polarization phase shift, without altering the PR. It is worth mentioning that polarization phase shifters are not only used to tune the polarization phase of the output SOP, but also to compensate for the deviations in the RWS operation, strongly affected by the fabrication errors.

Analogously to manual fiber polarization controllers, by using three pairs of RWS-TPPS the requirements of the RWS can be further relaxed, while in schemes using only two pairs of RWS-TPPS, as the depicted in figure 3.3 b), the RWS have rigid requirements. Integrated polarization controllers using two RWSs have already been proposed in the literature [120]. These schemes are based on RWS with a determined polarization conversion efficiency,

$$PCE_{RWS} = 0.5, \tag{3.1}$$

so, due to the sensitivity of RWSs to fabrication deviations, its operation is expected to be highly restricted by fabrication deviations. Nonetheless, the proposed scheme, based on three RWS-TPPS pairs, can operate in a broad range of fabrication deviations. It can be demonstrated (see appendix C) , assuming identical RWSs in the scheme, that the proposed scheme can achieve full coverage of the Poincaré sphere, even under the degradation of the RWS operation. Thus, as long as the PCE of the RWS meets the following condition:

$$\frac{1}{4} < PCE_{\text{RWS}} < \frac{3}{4}, \tag{3.2}$$

or equivalently:

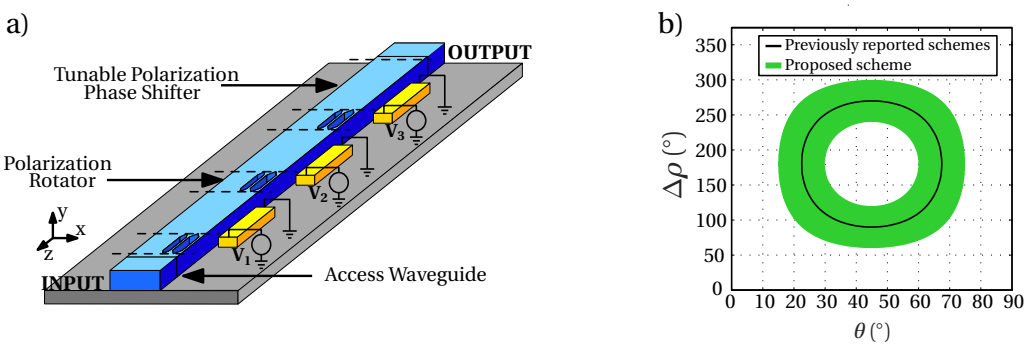

Figure 3.4.: a) Schematic of the proposed polarization controller scheme. b)Tolerance condition of the proposed scheme (green zone) versus the tolerance condition of the scheme based on two RWS (black line).

$$\frac{1}{4} < \left|J_{21,\mathrm{RWS}}\right|^2 < \frac{3}{4}, \tag{3.3}$$

full polarization control of light can be achieved.

Thus, in comparison with previously reported schemes, the proposed scheme, depicted in figure 3.4 a), guarantees the full coverage of the Poincaré sphere for a broad range of rotator waveguide sections PCEs, which ultimately results in higher tolerances to fabrication deviations.

This condition can also be expressed in terms of θ and $\Delta\rho$ (see eq. 2.32), so there are different combinations of θ and $\Delta\rho$ matching the tolerance condition. Figure 3.4 b) shows all the combinations of θ and $\Delta\rho$ that match the tolerance condition in the proposed scheme. The same figure includes the combinations of θ and $\Delta\rho$ that allows for full control of polarization in schemes that only include two RWSs. As can be observed, the range of RWS that match tolerance condition is by far wider than the range of RWS that match the condition of schemes based in two pairs of RWS-TPPS, making it highly tolerant to fabrication errors, in comparison with previously reported schemes.

To understand the principle of operation of the proposed scheme, let's consider an arbitrary input polarization state, defined by its polarization extinction ratio (PR_{in}) and its polarization phase (ρ_{in}), and a desired output polarization state, defined by PR_{des} and ρ_{des}. The first 5 elements of the proposed scheme, i.e. three polarization rotators and two tunable polarization phase shifters, aim to transform the PR_{in} into PR_{des}, provided that the tolerance condition is met. In such case, any arbitrary PR_{in} can be transformed into any arbitrary PR_{des} by properly adjusting the polarization phase shift that is induced in TPPS1 and TPPS2. Thus, before the last TPPS, the state of polarization will have the desired PR and an arbitrary polarization phase. Finally, the last TPPS is used to provide the desired polarization phase shift, so that the output SOP will have both the desired PR and polarization phase.

In order to illustrate the principle of operation, figures 3.5 a) b) and c) shows for a given SOP at the input of the device the evolution of the polarization state along the polarization controller when vertical (a), right handed circular (b) and horizontal (c) polarizations are desired at the output of the polarization controller. In all the three

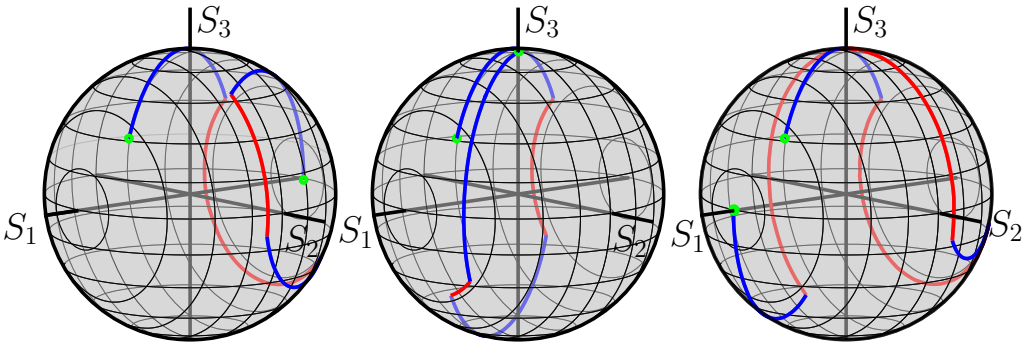

Figure 3.5.: Operation of the proposed scheme, represented on the Poincaré sphere. In all the cases the input polarization state is the same, while the output polarization state is vertical (a), right circular (b) and horizontal (c).

cases the rotator waveguide section is the same, with a PCE of 0.57 ($\theta = 31.5°$, $\Delta\rho = 117°$), that matches the tolerance condition.

3.3. Device Implementation

In order to experimentally demonstrate the operation of the proposed scheme, a prototype has been fabricated in the SOI technology at the Université Paris-Sud. The transversal geometry of the platform is shown in figure 3.6 a), where a silicon waveguide whose dimensions are 490 nm × 260 nm is depicted. Note that the whole device is clad with SU-8 polymer layer. The reason of using such material is that it will ease the implementation of the TPPS, as will be revealed in next sections.

In the next subsections, a deeper insight on the design of the rotator waveguide section design (section 3.3.1) and the tunable polarization phase shifter design (section 3.3.2) is provided. The last subsections is devoted to the discussion of the generated layout.

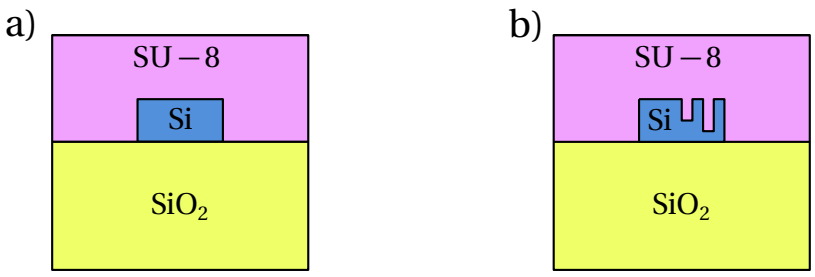

Figure 3.6.: Transversal geometry of the Si-wire (a) and the rotator waveguide section (RWS) (b).

Material	Refractive index (r.i.u.)	Thermo-optic coefficient ($°C^{-1}$)
Si	3.476	1.8×10^{-4}
SiO_2	1.44	1×10^{-5}
SU-8	1.58	-1.1×10^{-4}

Table 3.1.: Refractive index and TO coefficient of the materials used for the implementation of the polarization controller

3.3.1. Rotator waveguide section design

The designed rotator waveguide section follows the approach proposed in [88]. In this RWS, the mode hybridization is achieved by inducing an asymmetry on the waveguide through the inclusion of two subwavelength trenches, as depicted in figure 3.6 b), where the cross section of this RWS is shown. Insertion losses of this RWS geometry is around 0.7 dB [88]. This approach takes advantage of the calibrated reactive ion etch lag effect, that enables the implementation of different trench depths using a single mask and a single etch process. This will be of particular interest for our purpose, as by varying the dose of the etching, RWS with different PCE are easily fabricated.

The designed polarization rotator has the following dimensions: the trenches are ~ 60 nm and ~ 100 nm wide, separated by a ~ 40 nm silicon slice, and placed ~ 60 nm from the waveguide sidewall. Trench depths are determined by the etch-lag effect, being ~ 230 nm and ~ 250 nm nm deep, respectively. The length of the rotator is 20 µm. It has to be noted that the exact dimensions are not crucial for the operation of the device, provided that the RWS exhibit a PCE in the range defined by equation 3.2.

3.3.2. Tunable polarization phase shifter design

The TPPSs are realized by exploiting the thermo-optic coefficients of the platform materials which are shown, together with the materials refractive index, in table 3.1. Figure 3.7 shows the modal intensity of the fundamental TE and TM modes for the Si-wire waveguide depicted in figure 3.6 a). As can be observed, the TM mode strongly senses the SU-8 cladding, while the TE mode is well confined in the waveguide. This difference in the modal confinement together with the negative thermo-optic coefficient of the SU-8 causes the effective index of the fundamental TE and TM modes to change at a different ratio with temperature. To calculate the thermo-optic coefficient for the fundamental TE and TM modes the modal analysis of the structure, considering the thermo-optics coefficient of the materials, is performed. The simulated thermo-optic coefficient for the TE mode is $\mathrm{d}n_{\mathrm{eff}}^{\mathrm{TE}}/\mathrm{d}T = 1.7 \times 10^{-4} \, °C^{-1}$, while for the TM mode is $\mathrm{d}n_{\mathrm{eff}}^{\mathrm{TM}}/\mathrm{d}T = 1.1 \times 10^{-4} \, °C^{-1}$.

To calculate the polarization phase shift induced by a temperature variation ΔT, in a TPPS of length L_{TPPS}, the mode effective index temperature dependence is included in equation 2.14, resulting in:

$$\Delta\rho = 2\pi \frac{L_{\mathrm{TPPS}}}{\lambda} \left[\left(n_{\mathrm{eff}}^{\mathrm{TE}} - n_{\mathrm{eff}}^{\mathrm{TM}} \right) + \Delta T \left(\frac{\mathrm{d}n_{\mathrm{eff}}^{\mathrm{TE}}}{\mathrm{d}T} - \frac{\mathrm{d}n_{\mathrm{eff}}^{\mathrm{TM}}}{\mathrm{d}T} \right) \right]. \tag{3.4}$$

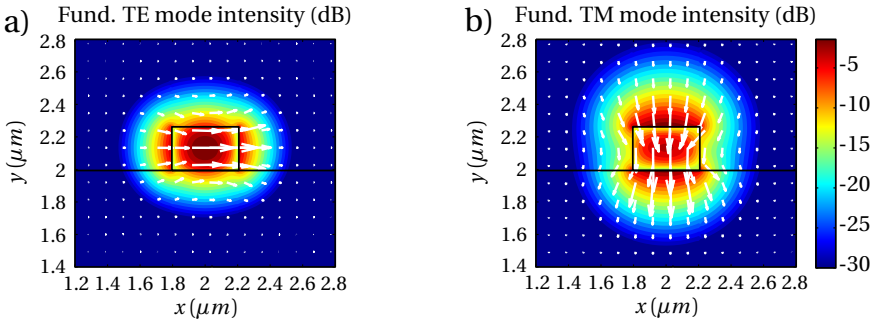

Figure 3.7.: For the waveguide depicted in 3.6 a), intensity and electric field of the fundamental TE (a) and TM (b) modes.

According to this equation, the longer the TPPS, the smaller the temperature increase that is needed to achieve a full 2π polarization phase variation. However, the length of the TPPS will impact the bandwidth of the device. Thus, if we calculate the derivative of equation 3.4 with respect to the wavelength it can be observed that the longer the device the more sensitive it is to wavelength variations, which ultimately limits the operational bandwidth of the polarization controller. Consequently, the design of the TPPS length, L_{TPPS}, requires a trade-off between bandwidth and maximum temperature increase.

To address this trade-off the whole scheme is modeled in Matlab using the Jones matrices of each component, i.e. TPPS and RWS Jones matrices. Then, the bandwidth is calculated as a function of L_{TPPS}, in a range of L_{TPPS} from 200 µm to 1200 µm. To calculate the bandwidth, the device is tuned in order to achieve TM polarization at the output. Once the device is tuned, the operation wavelength is swept, so that the device will be slightly detuned, and the PER of the output SOP will change. The bandwidth is defined as the bandwidth range in which the PER of the output SOP is larger than 16 dB. Figure 3.8 shows the bandwidth as a function of L_{TPPS}.

Besides the bandwidth calculation, from equation 3.4 the required temperature increase for a 2π polarization phase shift can be calculated. The result of this calculation is also depicted in figure 3.8, where, for different maximum temperature increase the induced polarization phase shift is shown as a function of L_{TPPS}.

Comparing the solid curve with the red dashed curve in figure 3.8, it can be observed that the minimum length that achieves a polarization phase shift variation of 2π with a moderate temperature increase of 40 °C is $L_{\text{TPPS}} = 700\,\mu$m. For this length, the simulated bandwidth is around 0.6 nm. However, as the bandwidth is not deemed as critical as the full phase swing, L_{TPPS} has been over-dimensioned to $1000\,\mu$m, so that polarization phase shifts of 2π are guaranteed, reducing the estimated device bandwidth to 0.4 nm.

The last step to design the TPPS is the inclusion of the waveguide heaters. This heaters are implemented through 2 µm wide, 100 nm thick chromium–gold electrodes, placed alongside the waveguide. The distance between the waveguide and the metal structure will determine the efficiency of the heater, so the nearest the waveguide is to the electrode, the more efficient is heat transfer. However, for short dis-

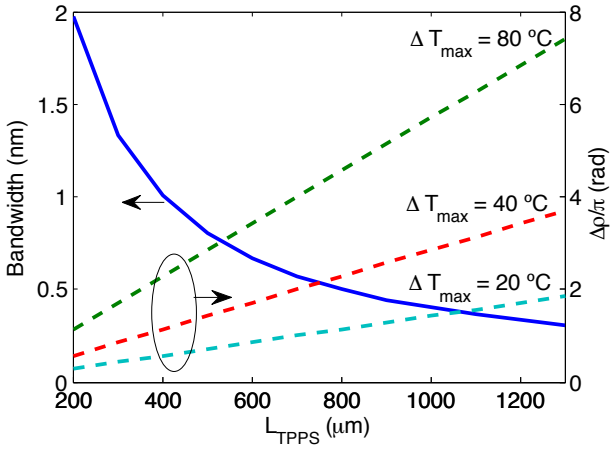

Figure 3.8.: Bandwidth and maximum polarization phase shift

tances the evanescent waveguide field can interact with the metallic electrode, inducing propagation losses. To evaluate the propagation losses, the modal analysis of the whole structure, i.e. waveguide and heater, is realized, calculating the propagation losses as a function of the distance between the waveguide and the heater, the results of this analysis are shown in figure 3.9. It can be observed that the TM mode exhibits higher losses, which is expected due to its higher effective area. However for a spacing of 1µm, the induced propagation losses are below 0.01 dB per TPPS. As power efficiency is not pursued, this spacing is finally set to 2µm, so that losses are negligible.

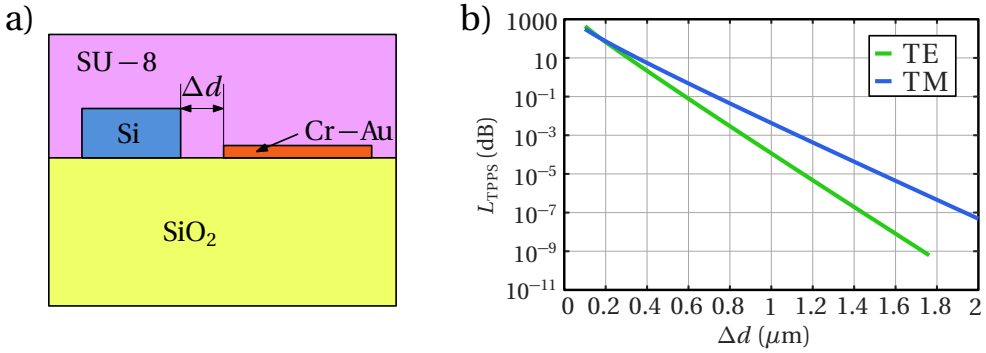

Figure 3.9.: a) Transversal geometry of the TPPS. b) Simulated insertion losses of the TPPS as a function of the distance between the Cr-Au electric wire and the photonic waveguide

3.3.3. Mask design and fabrication

During the design process of the layout, there are many aspect that have to be taken into account, such as the restrictions imposed by the fabrication process, and considerations relating the characterization of the device. In this case, as the fabrication

process is custom made, the layout is conceived mostly taking into account the measurement and characterization.

The designed mask is divided in different cells, where each cell contains four test structures with rotators of different lengths, in order to ensure that polarization rotators with different performance are fabricated. Each test structure contains together with the polarization controller scheme a straight waveguide, used to ease the fiber-to-chip alignment, and a waveguide containing a single rotator waveguide section, required to know if the rotator meets the tolerance condition. This rotator waveguide is placed near the polarization controller, so that we can assume that the rotator waveguide sections included in the controller are similar. The heaters are contacted using metal pads ($150 \times 100 \mu m^2$) that are tapered until the 2 µm wide metal wire is achieved. Thus the heater structure is composed of three metal pads, one for each heater, and a common ground pad. Figure 3.10 shows the layout of a single cell.

Finally, the difference among the cells, is the exposure dose, that will have an impact on the dimensions of the rotator waveguide sections, and consequently provided the RIE lag effect on the trenches depth.

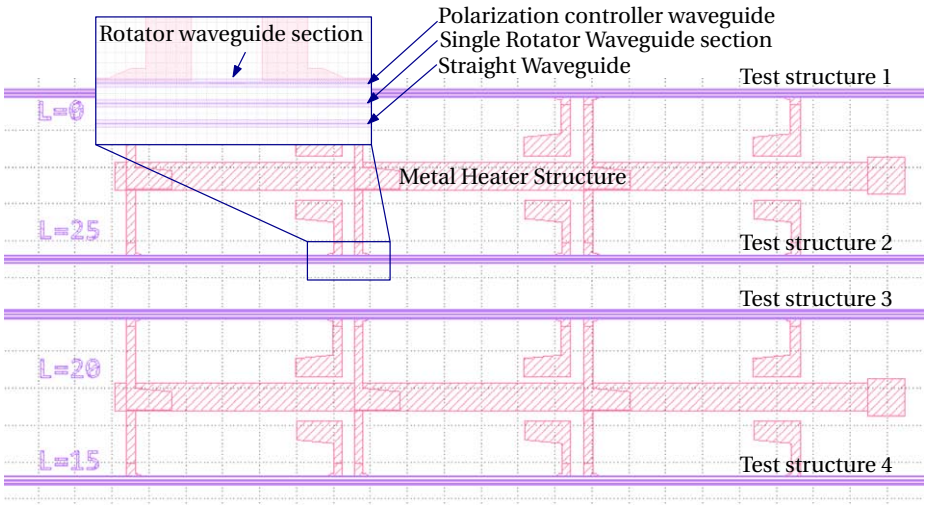

Figure 3.10.: Layout of a fabricated cell. The same cell has been replicated, applying a different exposure dose in each replica.

The photonic structures and isolation regions for metallic contacts were defined with ZEP electron beam (e-beam) positive resist lithography, and transferred to the silicon layer with inductively coupled plasma etching. A single, full etch step was used, leveraging the etch-lag effect to define the partially etched slots in PRs. The waveguide heaters were realized with 100-nm-thick chromium–gold electrodes fabricated with e-beam evaporation and a lift-off process; they had a measured resistance of ~165 Ω. Finally, waveguides were selectively covered with a UV lithography patterned 5 µm thick SU-8 negative resist, facilitating access to the metallic pads. Once thermally cross linked, SU-8 is thermally stable beyond 200°C.

3.4. Device measurements

3.4.1. Set-up

The measurement set-up is schematically illustrated in figure 3.11 a) and a picture of the same is provided in 3.11 b). In this set-up, linearly polarized light from a tunable laser source is launched into the photonic integrated circuit using a polarization maintaining lensed fiber. The fiber is loaded on a rotary mount, used to align the fiber optical axis with the chip optical axis, that is placed on a positioning stage, allowing to accurately realize the fiber-chip alignment.

At the output of the chip, light is collected by a microscope objective and then filtered by a linear polarizer, positioned on a rotation mount. The output of the filter is transmitted to an IR camera and the processed in the computer.

a) b)

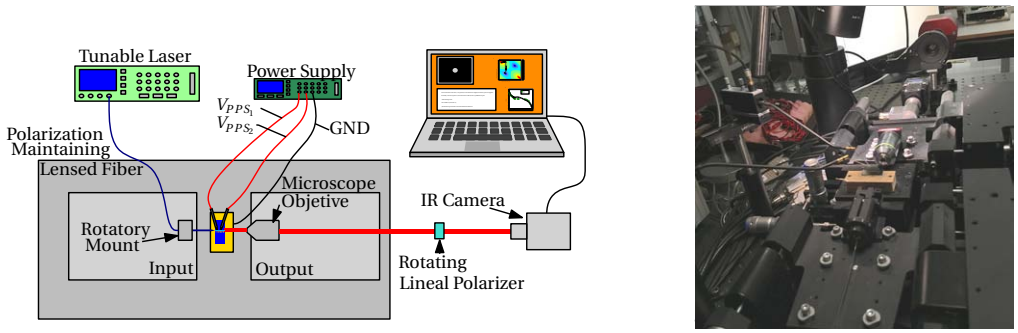

Figure 3.11.: a) Schematic of the measurement set-up. b) Picture of the set-up shown in a)

Figure 3.12a) shows the contour plot of the image captured by the camera, when there is no chip between the input fiber and the microscope objective. The power of such a light beam is measured by integrating the value of each pixels in an "area of interest" that is defined in the camera software. This will result very useful to measure the output of the chip, as it enables us to spatially filter the output signal. Before going deeper in the characterization of the polarization controller, the maximum measurable PER of the set-up has been evaluated. To perform this evaluation, horizontal polarization is set at the polarization maintaining fiber output. Then for different angles of the linear polarizer the optical power is recorded. The result of this experiment can be modelled using the Jones matrix of a rotated linear polarizer (see Table 2.2). Thus, the measured optical output power obeys to:

$$P_{\mathrm{MEAS}} = P_{\mathrm{IN}} \cos^2(\Delta\theta) \tag{3.5}$$

where $\Delta\theta$ is the angle between the polarization maintaining fiber optical axis, and the linear polarizer transmission axis. This expression is also known as the Malu's law, announced long before the Jones Calculus. Figure 3.12b) shows the result of the realized experiment together with the theoretical prediction, where the measured power is normalized to its maximum. A very good agreement between the experimental

measurements and the theoretical model can be observed. From this figure, it is observed that the minimum measurable PER is below -30 dB. The same experiment was repeated having TM polarization at the input, yielding a maximum measurable PER exceeding 30 dB. Thus, we can confirm that the measurable PER range of the set-up is higher than 60 dB.

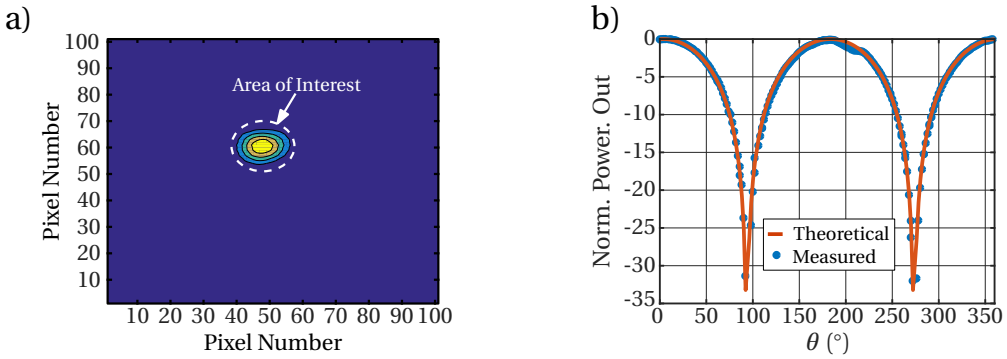

Figure 3.12.: a) Image of a light beam acquired by the IR cam. b) Maximum measurable extinction ratio in the employed set-up.

3.4.2. Polarization Controller experimental characterization

In this subsection, the characterization of the polarization controller is provided. In section 3.4.2.1 the characterization of the individual parts, i.e. RWS and TPPS is address, to ensure the appropriate operation of the device.

Then, in subsection 3.4.2.2, the operation of the device is demonstrated, through four different experiments. This experimental characterization constitutes one of the main results of this thesis.

3.4.2.1. Characterization of RWS and TPPS

As discussed in subsection 3.3.3, polarization rotator schemes with different rotator waveguide sections were fabricated. Thus, before evaluating the operation of the whole polarization controller scheme we need to find out if the included rotator waveguide section matches the tolerance condition, which is done by measuring the ER of the isolated rotators that are placed near the polarization controller scheme. As it is more convenient, the tolerance condition is reproduced here in terms of the ER of the RWS, and expressed in dB:

$$-4.77\,\text{dB} < \text{ER} < 4.77\,\text{dB} \tag{3.6}$$

Figure 3.13 a) shows the ER, in dB, of the different fabricated rotator waveguide sections. We observe that there are several waveguides that meet the tolerance condition, and could be used for the characterization of the whole scheme operation.

The polarization controller scheme also contains tunable polarization phase shifters (TPPS) that have to be characterized to check if polarization phase shifts of 2π are

achievable. Thus, polarization controller schemes with no rotator waveguide sections are used to realize this characterization. Linearly polarized light at 45º is injected in the device, equally exciting both the TE and TM modes of the waveguide. Then, only one of the three TPPS is biased, which will induce a phase shift between the TE and the TM modes. As the applied voltage is increased the output polarization state periodically fluctuates from linear +45, to right-handed circular, to linear -45 to left-handed circular. The resulting output light is then passed through the linear polarizer, rotated 45º with respect to the horizontal plane, and the optical power is measured. Modeling the system using Jones matrix, we obtain:

$$\mathbf{E_{OUT}} = \overline{\overline{M_{POL}(\theta)}}\,\overline{\overline{M_{CHIP}(\Delta\rho)}}\,\mathbf{E_{IN}}, \tag{3.7}$$

$$\mathbf{E_{OUT}}(\theta,\Delta\rho) = \begin{bmatrix} \cos^2\theta & \cos\theta\sin\theta \\ \cos\theta\sin\theta & \sin^2\theta \end{bmatrix} \begin{bmatrix} 1 & 0 \\ 0 & \exp(j\Delta\rho) \end{bmatrix} \frac{1}{\sqrt{2}} \begin{bmatrix} 1 \\ 1 \end{bmatrix}, \tag{3.8}$$

from this expression, the measured power can be obtained:

$$\mathbf{P_{OUT}} = \left|\mathbf{E_{OUT}}(\theta=\frac{\pi}{4},\Delta\rho)\right|^2 = \cos^2\left(\frac{\Delta\rho}{2}\right) = \frac{1}{2}\left(1+\cos\left(\Delta\rho\right)\right), \tag{3.9}$$

so the measured power is expected to change sinusoidally as a function of the induced phase shift. The results of the measurement, together with the theoretical prediction are shown in figure 3.13 b) . From this figure we find that the 2π phase shift is achievable. Furthermore, a tunning efficiency of 70 rad/W is extracted from this figure.

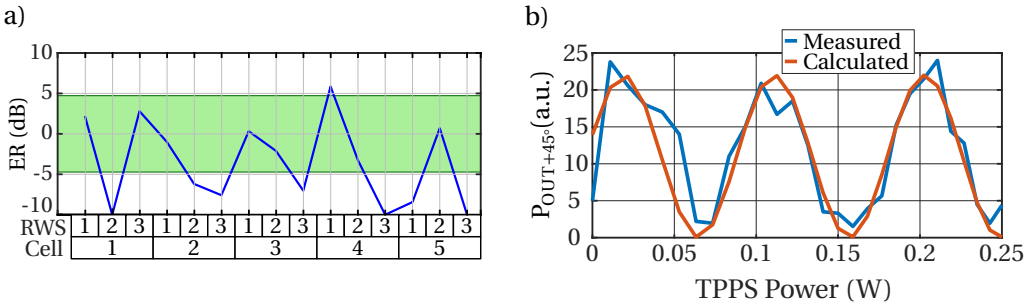

Figure 3.13.: a) ER measured in the different rotator waveguide sections. The green zone represent the range of ER that matches the tolerance condition. b) Result of the characterization of a single TPPS, a $\Delta\rho$ of 2π can be obtained with a power increment of around 100 mW.

3.4.2.2. Polarization controller operation

At this point, both the operation of the RWS and the TPPS have been successfully checked, so the operation of the whole polarization controller can be evaluated. The operation and the characteristics of the device are demonstrated throughout the next sections. To prove that the device effectively operates as a polarization controller, it

has to be demonstrated that polarization states with arbitrary PER and arbitrary polarization phase, are generated at the output of the device. Thus, in the first section, it is demonstrated that output polarization states with arbitrary PER are achieved, while the second section is devoted to demonstrate that for a given PER, the polarization phase of at the output can be arbitrarily chosen. The results of these experiments, will also provide an idea of the Poincaré sphere coverage that is achieved. Finally, the operation of the device in the whole C-Band is demonstrated, and the main characteristics of the polarization controller are provided.

Range of achievable PER In the experiment, horizontal polarization is injected into the polarization controller. In a first step, the polarization controller is tuned in order to obtain polarization states with a high PER, i.e. TM polarization at the output, and polarization states with a low PER, i.e. TE at the output. The maximum and the minimum achievable PER where in the order of ±20 dB, at an operation wavelength of 1.55 µm.

The tuning algorithm relies on minimizing the power in the SOP orthogonal to the desired one, by varying the voltage in one of the TPPSs. Once a minimum is found, the other TPPS is tuned. This process is repeated several times, until desired PER is achieved.

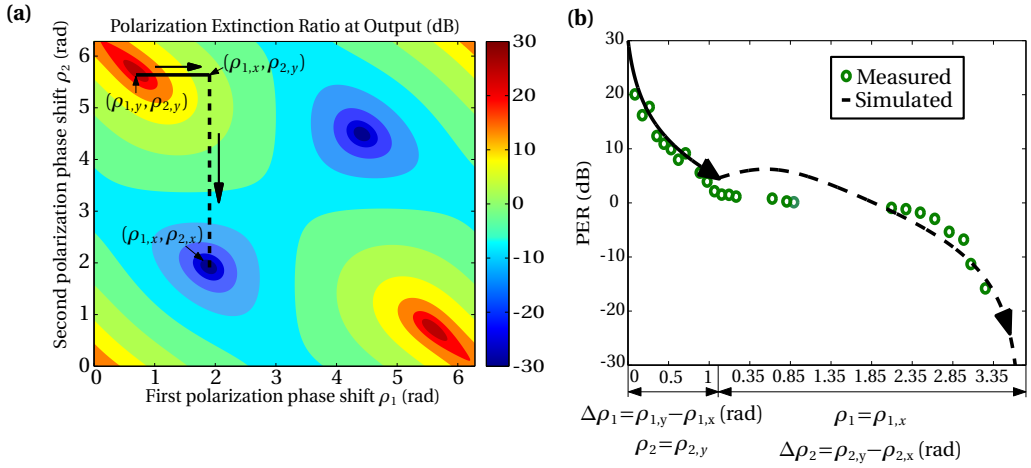

Figure 3.14.: (a) Simulated PER at the output of the polarization controller as a function of the phase shifts introduced in the two first TPPS, when horizontally polarized light is launched into the device at $\lambda = 1.55$ µm. (b) Measured PER compared to the simulated PER corresponding to the path shown in (a).

So far, the maximum and minimum achievable PER have been characterized, demonstrating a PER range of 40 dB. To show that any intermediate PER can be generated, the following experiment is realized: Let $(\rho_{1,y},\rho_{2,y})$ and $(\rho_{1,x},\rho_{2,x})$ be the phase shifts set on the first and second TPPSs in order to achieve vertical and horizontal polarization at the output of the device, respectively. To generate intermediate values of the PER, the phase shift is swept from $(\rho_{1,y},\rho_{2,y})$ to $(\rho_{1,x},\rho_{2,x})$, by changing the applied voltages V_1 and V_2. Thus, we start with $(\rho_{1,y},\rho_{2,y})$, so that TM polarization is achieved at the output. Then, V_1 is swept until $\rho_{1,y}$ reach $\rho_{1,x}$. The same process is repeated

with V_2 so that, at the end of the process, the induced phase shifts are $(\rho_{1,x}, \rho_{2,x})$, with TE polarization expected at the output of the device. Intermediate values of ρ_1 and ρ_2, are expected to produce intermediate PERs. As the ER of the RWS is known, the whole device has been simulated considering a similar RWS. Figure 3.14 a) shows the simulated PER as a function of ρ_1 and ρ_2. In this figure, the combinations (ρ_1, ρ_2) that have been used to demonstrate the intermediated PER values are superimposed. Figure 3.14 b) shows the simulated and the measured PER for the different combinations of (ρ_1, ρ_2). Both curves are in good agreement, indicating that the device can generate polarization states with arbitrary PER at its output.

Output polarization phase shift As previously commented, together with the output PER, it has to be checked that the output polarization phase can be arbitrarily chosen. In this case, the voltage applied on the third heater is swept, so that the output polarization phase changes.

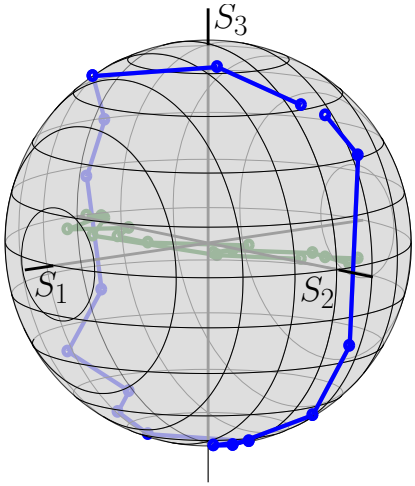

Figure 3.15.: Measured polarization state as an increasing voltage is applied at the third heater (V3), showing that any polarization phase ($\Delta\rho$) can be generated. The blue trace is obtained from the measured data points (green trace) by projection on the surface of the Poincaré sphere.

To measure the polarization phase, we take advantage of the Stokes parameters. In our set-up, s_1 and s_2 can be easily measurable, as it only requires to measure the power at the output of the polarizer for four rotation angles: 0° and 90°, to obtain s_1, and ±45°, to obtain s_2.

To obtain S_3, we take advantage of the Stokes parameters of fully polarized light (as occurs in this case), that lie on the surface of a sphere, thus matching the equation of the sphere. As s_1 and s_2 are measured, s_3 can be calculated as

$$s_3 = \sqrt{1 - {s_1}^2 - {s_2}^2}. \tag{3.10}$$

Figure 3.15 shows, on the Poincaré sphere, the Stokes parameters of the output polarization state when the voltage applied on the third heater is swept. It can be observed that the polarization phase is 2π shifted. Ideally the PER should be constant,

as only V_3 is changing. However, due to the thermal crosstalk, small variations of the PER are observed.

Polarization controller characteristics At this point, the operation of the polarization controller has been demonstrated, achieving full polarization control, in a PER range of 40 dB, which is a world record achievable PER in a CMOS compatible, integrated polarization controller. In this subsection the characteristics of the polarization controller are discussed.

The insertion losses of the polarization controller where measured by comparing the output power of the controller scheme with the reference waveguide and insertion losses below 3 dB were found. The main contribution of these losses comes from the rotator waveguide sections, whose individual insertion losses are in the order of 0.7 dB [88].

The efficiency of the TPPS has also been measured. For the single TPPS, the measured efficiency was 70 rad/W. However, when all the TPPS are activated, the efficiency decreases to 20 rad/W. The average power consumption is found to be around 300 mW, with peaks values in the order of 700 mW.

Regarding the bandwidth of the device it has been measured with TE and TM polarizations at the output. Figure 3.16 a) shows the PER of the output state as a function of the operation wavelength. From these figure it can be observed that the measured bandwidth is around 0.4 nm. As we discussed in the design section, the bandwidth is limited by the TPPS length.

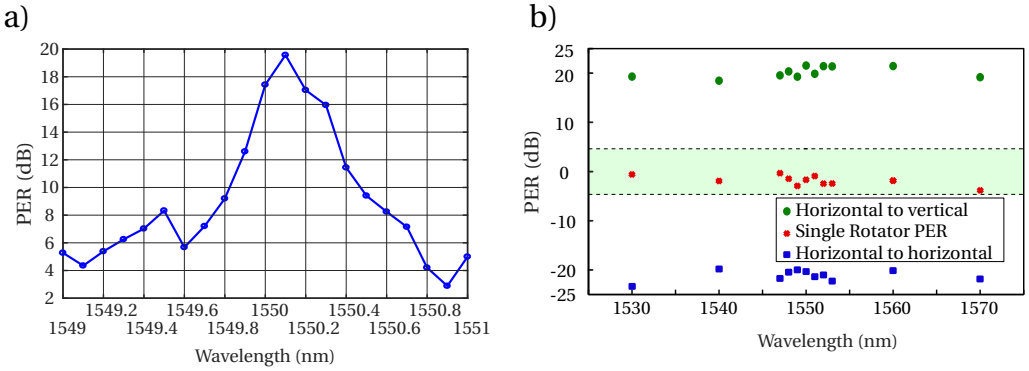

Figure 3.16.: a) Measured polarization controller bandwidth, when horizontal polarization is at the input and the device is tuned to have TM polarization at λ 1550 nm. b) Measured Polarization Extintion Ratio (PER) when horizontally polarized light is launched into the device. Tuning of the integrated polarization controller provides a PER range of $\sim$ 40 dB at any C-Band wavelength.

Finally, the operation of the device is demonstrated in a wide wavelength range. Prior to the tunning of the scheme along C-band, the ER of the rotator waveguide section has been evaluated, to check that the tolerance condition is met along the wavelength range. Then, the device has been tuned to have the maximum and minimum achievable PER at the output. Figure 3.16 b) shows the result of these measurements. In this figure, for each wavelength the ER of the RWS is shown together with

the maximum and the minimum achieved PER.

3.5. Conclusions

In this chapter, a fully integrated polarization controller, implemented in the Silicon-On-Insulator platform has been demonstrated. This polarization controller is implemented using rotator waveguide sections, and tunable polarization phase shifters. This polarization controller is, to the best of the author knoledge, the first fully integrated polarization controller achieving a polarization extinction range in excess of 40 dB, being tunable in the full C-Band.

Besides the wavelength tunability, the tunable polarization phase shifters allows the compensation of fabrication deviations, so, as long as the implemented rotator waveguide sections match the tolerance condition, which is technology independent, full coverage of the Poincaré sphere is guaranteed even in presence of fabrication deviations, which have been until known the main constraining factor in the design of polarization managing devices.

4

Integrated dual polarization coherent receiver design

4.1. Historical background of optical fiber communication systems

The earliest optical fiber communication systems, based on On-Off-Keying (OOK) transmission schemes, arose in the early 1970s, after the advent of both semiconductors lasers and low-loss fibers [122]. In these systems, an intensity modulator generated logical 1s and 0s by turning a laser source on and off, while at the receiver side a simple photodiode directly detected the power of the incoming signal. Those are the reasons why these systems are called IM-DD (Intensity Modulation-Direct Detection). Together with their low-cost and simplicity, these systems had the advantage of being tolerant to fluctuations in phase and polarization of the optical signal as it propagates along the fiber, because the transmission is based solely on field intensity. In absence of optical amplification (Erbium doped fiber amplifier –EDFAs– were developed in the early 1990s) IM-DD systems are shot-noise limited for long distances [123], so during the 1980s coherent optical systems were proposed as an alternative.

In coherent systems, the information is transmitted on both the amplitude and the phase of the optical field so a local oscillator (LO) used as a reference signal, is required on the receiver side. Coherent optical systems introduced two advantages to overcome the shot-noise limitations of these first IM-DD systems without optical amplification. The first one is that coherent modulations are more robust against noise than intensity modulations, i.e. Binary Phase Shift Keying (BPSK) modulation provides 6 dB improvement in signal to noise ratio (SNR) over OOK [124,125]. The second one is the coherent gain: as the transmitted signal is mixed with the local oscillator, by increasing the power of the local oscillator it is possible to overcome the shot-noise limitations [126, 127]. At that time, polarization multiplexing, i.e. carrying two different information signals in two orthogonal polarization states, was also proposed [18]. The drawback of this technique was that due to polarization mode dispersion (PMD), the signal suffers arbitrary rotations during the propagation, so it was necessary to track the evolution of the polarization in the receiver, and compensate for it.

Many integrated coherent systems were demonstrated during the 1980s [128, 129],

but they had two drawbacks: from a commercial point of view, the proposed solutions were not cost-effective for the data rates required at that time, and from a technical point of view issues relating the laser line-width and the required high speed electronics made these systems almost impractical. With the advent of the EDFA in the early 1990s IM-DD systems overcame the shot-noise limitation, thereby depriving coherent systems of their main advantage. Consequently, the interest in coherent systems declined, and the research and development in the area during the next ten years were rather limited. Hence, IM-DD systems, together with wavelength division multiplexing (WDM) techniques, played the central role in optical fiber communications, achieving data rates up to 10 Gbps in commercial scenarios with transmission distances up to 2000 km [130].

With the ever-increasing bandwidth demand IM-DD systems reached their limit at the end of 1990s, because the dispersive effects of the fiber made long distance (>1000 km) transmission of OOK modulated signals for data rates higher than 20 Gbps infeasible [127, 131]. Thus, at the beginning of 2000s, coherent reception started to attract interest for the second time in history. The first step was to employ differential phase modulation formats that improved the spectral efficiency without using an LO signal at the receiver, as they are based on interferometric direct detection [125, 132]. These schemes were also combined with polarization multiplexing techniques, doubling the channel capacity in a cost-effective way, and data rates up to 200 Gbps were reported [10]. However, such a high data rates were demonstrated only in laboratory experiments, while commercial solutions achieved data rates up to 40 Gbps [133,134].

The next step was the inclusion of coherent detection techniques in the receiver, claimed as the most promising detection techniques [9]. As the optical field is fully detected, i.e. phase, amplitude and polarization are recorded simultaneously, coherent detection holds two enormous advantages. The first one is that multilevel modulation formats, i.e. M-ary Quadrature Amplitude Modulation (M-QAM), can be employed, improving the spectral efficiency. The second advantage is that signal processing in the electrical domain can be applied to equalize the detected signal, thus compensating for the channel impairments. This signal processing is performed in the digital signal processor (DSP), which has been a key element in the success of the coherent communications. Due to the advances in high speed electronics [127], optical problems such as carrier synchronism or polarization tracking, can be translated to the electrical domain, and solved through digital signal processing algorithms in a cost-effective way. Furthermore, coherent detection schemes held the potential to offer higher data rates than direct detection schemes while keeping the deployed infrastructures.

In 2010, the **Optical Internetworking Forum (OIF)** released the first implementation agreement for integrated dual-polarization coherent receivers, specifying the key aspects of integrated coherent receivers targeting 100 Gbps per channel on a 50 GHz grid. In the same year, a monolithically integrated dual polarization coherent receiver prototype was demonstrated [135], achieving 112 Gbps. Just one year later, the first commercial coherent 100 Gbps system became available [136].

As bandwidth demand continues growing exponentially, 400 Gbps per channel coherent communications have emerged as the next target. The path towards 400G is more technologically challenging that it was for 100G, with trade-offs between modu-

lation formats, subcarrier multiplicity (using several subcarriers simultaneously) and symbol rates, so different applications (metro, long-haul, short-haul...) will rely on different implementations [137]. Systems reaching 400 Gbps have recently been demonstrated in lab experiments [138,139]. However the industry is far from 400G standardization, even if some commercial devices are already available [7].

Future coherent communication systems are expected to be flexible, adapting the traffic resources to the bandwidth demands. This flexibility will rely on the characteristics of three different elements: the transceiver, which will be expected to adapt the bit rate to the traffic needs, the WDM granularity, which has to be further reduced to properly adapt the network capacity to the traffic demands, and the advent of a new spatial dimension, that will arise from the use of multiple fibers or space-division multiplexing (SDM) techniques [140].

4.2. Dual polarization coherent optical fiber communication system

We will now focus on the implementation of a dual polarization coherent system, as depicted in figure 4.1, comprising a transmitter, the channel and a receiver. The functionality of each block is concisely described below.

- Transmitter: the optical carrier, generated in a laser source, is split and then feeds two different IQ (In-phase and Quadrature) modulators. Each modulator also has two electrical inputs. The signals at these inputs will modulate both the phase and the amplitude of the optical field, generating the in-phase and quadrature components of the transmitted signal. At the output of each modulator an optical IQ signal is generated. In the proposed schematic shown in figure 4.1, both modulators will encode the information in the same state of polarization. In order to realize the polarization multiplexing, it will be necessary to rotate the polarization of one IQ modulator; this is done by a polarization rotator (PR). Then, the two beams, which have orthogonal polarizations, are combined in the polarization beam combiner (PBC).

- Channel: models the transmission medium, usually an optical fiber. During the propagation along the optical fiber, the transmitted signal will suffer of linear impairments such as attenuation, chromatic dispersion (CD), polarization mode dispersion (PMD), polarization dependent losses (PDL) and non-linear impairments such as cross phase modulation (XPM), four-wave mixing (FWM) and non-linear phase noise (NLPN) [141]. It is worth mentioning that due to PMD, arbitrary polarization rotation will occur during the propagation. All these impairments will be treated in the receiver, specifically in the digital signal processor (DSP) [141, 142].

- Receiver: is in charge of retrieving the originally transmitted data. As depicted in figure 4.1, it is composed of three elements: the local oscillator, the dual polarization IQ downconverter, also called optical front-end, and the digital signal processor (DSP). The local oscillator generates a continuous wave optical signal, **LO**, that is combined with the input signal, $\mathbf{S^{RX}}$, in order to perform the

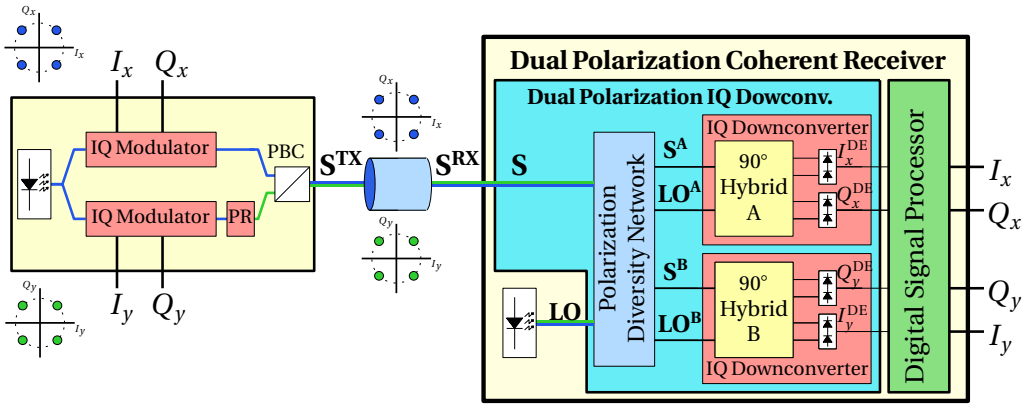

Figure 4.1.: Schematic of a dual polarization coherent optical communication system. In the transmitter two IQ signals are encoded in two orthogonal polarization states. The receiver, composed of a dual polarization IQ downconverter and a digital signal processor, is able to compensate for the channel impairments, thus recovering the original transmitted signals. PR: Polarization Rotator, PBC: Polarization beam combiner, LO: Local Oscillator

demodulation. The optical front-end contains the photonic circuitry, including the photodiodes, where the optoelectronic conversion takes place. Then, the photodiode output signals, are converted to the digital domain through analog-to-digital converters, and sent to the DSP. However, the digital received IQ signals from both polarizations will differ from those originally encoded at the transmitter, mostly due to the channel impairments and the non-ideal behavior of the receiver. To compensate for these undesired effects, signal processing algorithms are applied in the DSP, which is of fundamental importance for the correct coherent receiver operation [142]. DSP functions mainly include:

- De-skew and orthonormalization, that compensate for optical front-end imperfections with algorithms such as Gram-Schmidt [143].
- Static and dynamic channel equalization, targeting CD compensation and PMD compensation [141], implemented through algorithms such as the constant modulus algorithm [144, 145], that essentially performs a digital polarization demultiplexation.
- Timing recovery, that focus on the mismatch between the symbol clock and the ADC sample rate [146].
- Frequency and phase carrier recovery, aiming to reduce the differences between the frequency and phase of the local oscillator and the signal carrier. This includes algorithms for carrier frequency estimation such as the proposed by Ip and Kahn in [147], and algorithms for carrier phase estimation as the so-called Viterbi and Viterbi algorithm [148] .

As this chapter is devoted to the implementation of an integrated dual polarization coherent downconverter, the following section will further explain the principle of operation and the subsystems of a dual polarization coherent downconverter.

4.3. Dual polarization coherent downconverter

As shown in figure 4.1, the optical front-end is formed by two different subsystems: the polarization diversity network, and the IQ downconverters.

The polarization diversity network manages the polarization of the incoming signal (**S**) and the local oscillator (**LO**) in such a way that, after being down-converted, the IQ signals encoded in each polarization are correctly retrieved. The IQ downconverters, one for each polarization, comprises a 90° optical hybrid and two pairs of balanced photodiodes. These elements will separate the in-phase and quadrature components of the incoming optical signal, and perform the frequency downconversion. It is worth mentioning that the 90° hybrids are the core elements of a coherent receiver.

For this analysis we will employ an ideal incoming on-chip signal **S**, this signal is related to the received signal, $\mathbf{S^{RX}}$, by a projection matrix, $\overline{\overline{M_C}}$, which projects the optical fiber polarization axis on the chip polarization axis:

$$\mathbf{S} = \overline{\overline{M_C}}\mathbf{S^{RX}} \tag{4.1}$$

At the same time, as the transmitted signal ($\mathbf{S^{TX}}$) suffers arbitrary polarization rotation, $\mathbf{S^{RX}}$ is a lineal transformation of $\mathbf{S^{TX}}$:

$$\mathbf{S^{RX}} = \overline{\overline{M_F}}\mathbf{S^{TX}} \tag{4.2}$$

where $\overline{\overline{M_F}}$ models the arbitrary rotation during the fiber propagation. Thus, each of the polarizations states of **S** have a contribution of both polarization multiplexed transmitted signals, according to the following expression:

$$\mathbf{S} = \overline{\overline{M_C}}\,\overline{\overline{M_F}}\mathbf{S^{TX}} \tag{4.3}$$

The DSP will be in charge of unscramble the arbitrary polarization rotation. Thus, for the sake of clarity in the following subsections, we will abstract from this problem by considering **S**, (or it single-polarization counterpart S) as the input signal of the different subsystems.

4.3.1. The IQ downconverter

As previously stated, this subsystem is composed of a 90° hybrid and four photodiodes, as depicted in figure 4.2 a). The photodiodes are usually disposed in a balanced configuration, thus rejecting DC components [114].

In the following paragraphs, the operation of the ideal single polarization downconverter, assuming homodyne detection, i.e. the frequency of the incoming signal and the local oscillator are the same, is described. To do so, we will consider the single polarization complex amplitudes of the incoming signal, S, and the local oscillator, LO. S and LO are combined in the 90º hybrid, which is modeled with its ideal transmission matrix [114]:

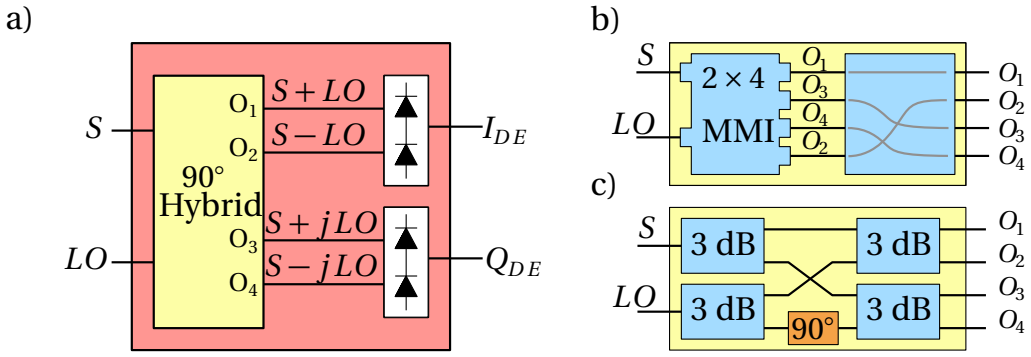

Figure 4.2.: a) Schematic of an IQ downconverter, composed of a 90° hybrid, and two pairs of balanced photodiodes. b) and c) are two different implementations of the 90° hybrid. b) is composed of a 2×4 MMI, and an output network to route the hybrid outputs to the correct photodiode pair. c) is composed of 3 dB couplers, and a 90° phase shifter.

$$\overline{\overline{M}}_{90^\circ} = \frac{1}{2}\begin{bmatrix} 1 & 1 \\ 1 & -1 \\ 1 & j \\ 1 & -j \end{bmatrix} \tag{4.4}$$

Thus, at the output of the 90° hybrid there will be four different combinations of S and LO [figure4.2 a)]:

$$\begin{bmatrix} O_1 \\ O_2 \\ O_3 \\ O_4 \end{bmatrix} = \overline{\overline{M}}_{90^\circ}\begin{bmatrix} S \\ LO \end{bmatrix} = \frac{1}{2}\begin{bmatrix} \sqrt{P_S}e^{j\theta_S} + \sqrt{P_{LO}} \\ \sqrt{P_S}e^{j\theta_S} - \sqrt{P_{LO}} \\ \sqrt{P_S}e^{j\theta_S} + j\sqrt{P_{LO}} \\ \sqrt{P_S}e^{j\theta_S} - j\sqrt{P_{LO}} \end{bmatrix} \tag{4.5}$$

where P_S is the power of the incoming signal, P_{LO} is the power of the local oscillator, and θ_S is the phase of the incoming signal.

In order to correctly retrieve the in-phase (I) and quadrature (Q) components of S, the signals in which the LO is 180° phase-shifted are combined in each pair of balanced photodiodes, i.e. O_1 and O_2 in one pair, and O_3 and O_4 in the other one, as depicted in figure 4.2 a). In each photodiode, ideally modeled with its quadratic response and a responsivity R, a photocurrent proportional to the incoming power will be generated: $i_k = R|O_k|^2$ with $k = 1,...,4$. Thus, the photocurrents at the output of the balanced photodiodes, $I_{DE} = I_1 - I_2$ and $Q_{DE} = I_3 - I_4$, can be easily calculated, resulting in:

$$\begin{aligned} I_{DE} &= R|O_1|^2 - R|O_2|^2 = R\left(\sqrt{P_S P_{LO}}\cos(\theta_S)\right) \propto I \\ Q_{DE} &= R|O_3|^2 - R|O_4|^2 = R\left(\sqrt{P_S P_{LO}}\sin(\theta_S)\right) \propto Q \end{aligned} \tag{4.6}$$

where it is assumed that all the photodiodes have the same responsivity. Note that, the output photocurrents are proportional to the in-phase and quadrature components of the incoming signal. It should be emphasized that the amplitude of the output signals, I_{DE} and Q_{DE}, are proportional to the local oscillator power. Thus, by

increasing the LO power, the outputs photocurrents are boosted. This is known as the coherent gain that is employed to overcome the shot-noise of the receiver circuit.

Concerning the implementation of 90° hybrids, many approaches has been proposed in the bibliography [149–152], but here we will focus on the more commonly used architectures, which are depicted in figure 4.2 b) and c).

The schematic depicted in figure 4.2 b) shows the simplest implementation, which is a 2×4 multimode interferometer (MMI), i.e. a 4×4 MMI where only two inputs are used [150]. This implementation inherently provides the required phase-shift relations, in a single and passive device. The main drawback of this approach is that the output ports with *LO* phase-shifted by 180° are not adjacent, so it will be necessary to include an output network to correctly place the outputs. This network has to be designed in such a way that the four paths are identical (i.e. same length, same number of crossings, same curves...).

An alternative design is depicted in figure 4.2 c): in this case it is composed of four 3 dB couplers, and a 90° phase-shifter. The main advantage of this implementation is that by properly locating the phase shifter, i.e. as shown in 4.2 c), the output ports with *LO* phase-shifted by 180° are adjacent, so the connection with the balanced photodiodes does not require any special attention. However, the inclusion of the phase shifter represents the weak point of this design: phase shifters are quite sensitive to fabrication variations and usually requires an active control, thus increasing power consumption and receiver complexity.

Due to its compactness and absence of active control elements, the 2×4 MMI based 90° hybrid is the preferred option, being implemented in most of the coherent receivers reported to date [135, 153, 154].

As it will be useful in section 4.4, we will now extend the previous analysis to a more general case, considering that the input signal *S* and *LO* are not single polarization:

$$\mathbf{LO} = \begin{bmatrix} LO_x \\ LO_y \end{bmatrix} \quad \mathbf{S} = \begin{bmatrix} S_x \\ S_y \end{bmatrix} \tag{4.7}$$

If we assume that the 90º hybrid behaves ideally for both polarizations, and there is no polarization conversion, the four 90º outputs read:

$$\begin{bmatrix} \mathbf{O}_1 \\ \mathbf{O}_2 \\ \mathbf{O}_3 \\ \mathbf{O}_4 \end{bmatrix} = \begin{bmatrix} \mathbf{S}+\mathbf{LO} \\ \mathbf{S}-\mathbf{LO} \\ \mathbf{S}+\mathbf{jLO} \\ \mathbf{S}-\mathbf{jLO} \end{bmatrix} \tag{4.8}$$

These dual polarization signals feed the photodiodes. As previously mentioned, the photocurrent generated in a photodiode is proportional to the signal power exciting it. The power of a dual polarization signal is the combination of the power in each polarization, i.e. $P_{\mathbf{S}} = |S_x|^2 + |S_y|^2$. Thus, if the photodiode is excited for example with $\mathbf{S}+\mathbf{LO}$, then the generated photocurrent will be proportional to the addition of the total power in each polarization:

$$i = R(|S_x + LO_x|^2 + |S_y + LO_y|^2) \tag{4.9}$$

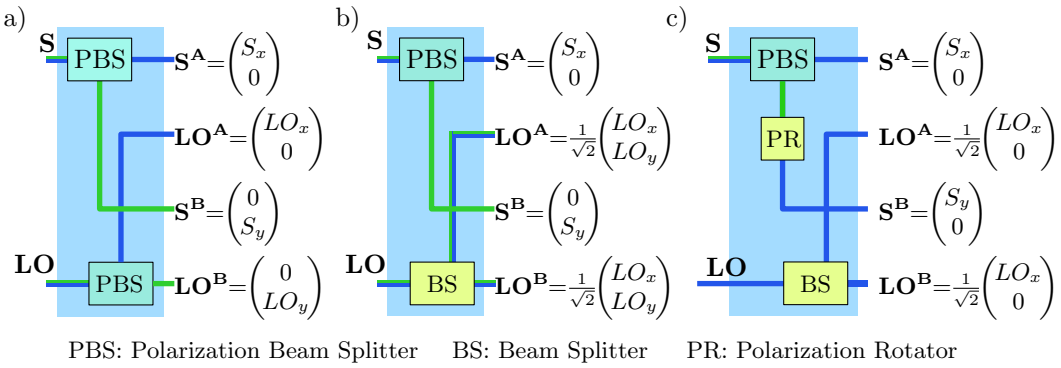

Figure 4.3.: a) and b) Polarization diversity network schemes proposed by the OIF. c) Polarization diversity network that operates with just one "on-chip" polarization

where the same responsivity is assumed for x and y polarizations. Neither the 90º hybrid nor the photodiodes produce polarization conversion. Consequently the previous analysis can be independently applied for each polarization, resulting in:

$$\begin{aligned} I_{DE} &= R\left(\sqrt{P_{S_x}P_{LO_x}}\cos\left(\theta_{S_x}\right)\right) + R\left(\sqrt{P_{S_y}P_{LO_y}}\cos\left(\theta_{S_y}\right)\right) \propto I_x + I_y \\ Q_{DE} &= R\left(\sqrt{P_{S_x}P_{LO_x}}\sin\left(\theta_{S_x}\right)\right) + R\left(\sqrt{P_{S_y}P_{LO_y}}\sin\left(\theta_{S_Y}\right)\right) \propto Q_x + Q_y \end{aligned} \tag{4.10}$$

Hence, the in-phase and quadrature retrieved signals carry indistinguishable contributions from both polarizations. In practice, as one would like to separate the contribution of each polarization, a polarization diversity network is required. The functionality of the polarization diversity network is further described in the next section.

4.3.2. The polarization diversity network

In the conventional architecture of dual polarization coherent receiver, the polarization diversity network aims to separate the information carried in each polarization state of the incoming signal. The OIF, proposes two different implementations of the polarization diversity network [20], which are also the most common schemes for polarization diversity networks in the literature [20, 135, 153–156]. These two schemes, depicted in figure 4.3 a) and b) are compared in the following paragraphs, considering the inputs signal $\mathbf{S} = [S_x, S_y]^T$ and $\mathbf{LO} = [LO_x, LO_y]^T$, where the subscripts refer to the x and y polarizations on-chip. At the output of the network, signals with same superscript are directed to the same IQ downconverter.

The structure shown in figure 4.3 a), which is the most intuitive solution, is composed of two polarization beam splitters (PBS). These devices will separate the horizontal from the vertical polarization so that each IQ downconverter will receive a different polarization component:

$$\mathbf{S^A} = \begin{bmatrix} S_x \\ 0 \end{bmatrix} \quad \mathbf{S^B} = \begin{bmatrix} 0 \\ S_y \end{bmatrix} \quad \mathbf{LO^A} = \begin{bmatrix} LO_x \\ 0 \end{bmatrix} \quad \mathbf{LO^B} = \begin{bmatrix} 0 \\ LO_y \end{bmatrix} \tag{4.11}$$

Thus, in this implementation, each IQ downconverter has to manage a different polarization. This results in a problem when one of the polarizations is not recom-

mended in the platform (for example, in the 220 nm silicon thickness platform, the vertical polarization is not supported).

The schematic depicted in figure 4.3 b) makes use of a beam splitter (BS) instead of a PBS in the LO branch. In this case, the four outputs are:

$$\mathbf{S^A} = \begin{bmatrix} S_x \\ 0 \end{bmatrix} \quad \mathbf{S^B} = \begin{bmatrix} 0 \\ S_y \end{bmatrix} \quad \mathbf{LO^A} = \frac{1}{\sqrt{2}} \begin{bmatrix} LO_x \\ LO_y \end{bmatrix} \quad \mathbf{LO^B} = \frac{1}{\sqrt{2}} \begin{bmatrix} LO_x \\ LO_y \end{bmatrix} \tag{4.12}$$

In this approach the *LO* signal is power divided so every downconverter receives an *LO* signal with both polarization components. As previously mentioned, in the photodiodes only components with the same polarization are mixed, so half of the *LO* power is wasted, resulting in a 3 dB sensitivity penalty. The main advantage of this configuration is that it only uses one PBS, making it a simpler alternative in practice.

There are others alternatives, such as the one depicted in figure 4.3 c). This alternative avoids having to design the rest of the receiver for both polarizations, as all the polarization diversity network outputs are in the horizontal polarization. This scheme was also proposed by the OIF in the early days. However, the stringent fabrication tolerances of polarization rotators hindered its implementation.

One of the main problems that current dual-polarization coherent receivers are facing is the integration of the polarization diversity network. The main reason is that polarization management devices, i.e PBSs and PRs, usually are very sensitive to fabrication deviations [84, 157], leading to very low fabrication yields. Fabrication tolerances can be relaxed through the inclusion of active tuning elements [126, 158], but this approach will increase the power consumption of the receiver. This unsolved problem has led the OIF to establish the integration of the PBS [20] as non-mandatory, resulting in devices with PBS implemented in bulk optics [154], and difficulting the integration and miniaturization of the receiver, which ultimately increments the cost of the receiver.

Future integrated coherent optical communication systems are envisioned to further reduce the power consumption and thus the operational cost. One way to reduce these costs, involves the full passive integration of the polarization diversity network. In the next subsection, an alternative to the conventional polarization diversity networks, which avoids the use of polarization management devices, is presented [21].

4.4. The PBS-Less dual-polarization IQ downconverter

The PBS-Less dual polarization IQ downconverter was first proposed in [21]. Figure 4.4 shows the architecture of this approach, where the main novelty is in the polarization diversity network. Instead of PBSs, the polarization diversity network is implemented with two polarization independent BS and a polarization-phase assisted network, comprised of four passive polarization phase shifters (PPS). Polarization phase shifters induce a different phase-shift to each polarization, as explained in chapter 2. The outputs of the polarization diversity network are directed to two IQ downconverters. As stated in section 4.3.1 the outputs of an IQ downconverter excited with two polarization-states, include contributions of both polarizations, which are in principle indistinguishable. However, by judiciously choosing the polarization phase shift,

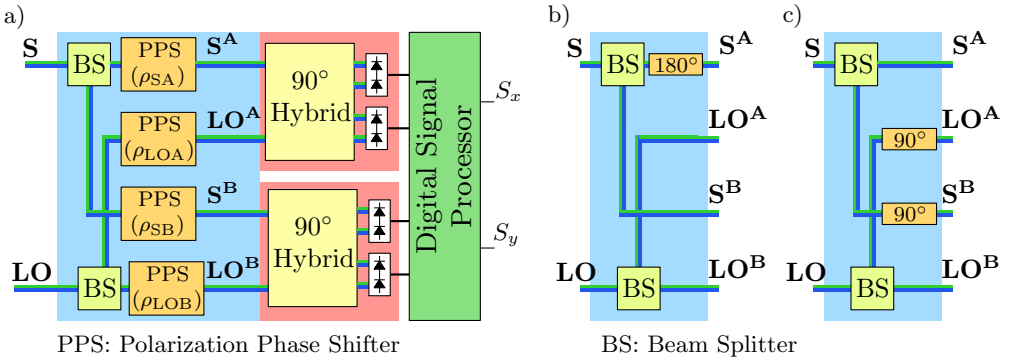

Figure 4.4.: a) PBS-Less dual polarization IQ downconverter. b) and c) are two particular cases of induced polarization phase shifts, that are further analyzed.

the original IQ signals of each polarization can be correctly recovered from the outputs of the two IQ downconverters.

The operation of the PBS-Less is illustrated in the following, assuming ideal components. We will again consider the complex amplitudes of the incoming signal and the local oscillator for both polarizations, described by their Jones vectors as follows:

$$\mathbf{S} = \begin{bmatrix} S_x \\ S_y \end{bmatrix} = \begin{bmatrix} I_x + jQ_x \\ I_y + jQ_y \end{bmatrix} \quad \mathbf{LO} = \begin{bmatrix} LO_x \\ LO_y \end{bmatrix} \tag{4.13}$$

Each signal, after being split, will be fed into a polarization phase shifter (PPS), whose Jones matrix is:

$$\overline{\overline{J}}_{PPS} = \begin{bmatrix} e^{j\varphi_x} & 0 \\ 0 & e^{j\varphi_y} \end{bmatrix} = e^{j\varphi_y} \begin{bmatrix} e^{j\rho} & 0 \\ 0 & 1 \end{bmatrix} \tag{4.14}$$

where $\rho = \varphi_x - \varphi_y$. In the following calculations it will be considered $\varphi_y = 0$. Thus, the outputs of the polarization diversity network are given by the following expressions:

$$\begin{aligned} \mathbf{S^A} &= \frac{1}{\sqrt{2}} \begin{bmatrix} S_x e^{j\rho_{SA}} \\ S_y \end{bmatrix} \quad \mathbf{LO^A} = \frac{1}{\sqrt{2}} \begin{bmatrix} LO_x e^{j\rho_{LOA}} \\ LO_y \end{bmatrix} \\ \mathbf{S^B} &= \frac{1}{\sqrt{2}} \begin{bmatrix} S_x e^{j\rho_{SB}} \\ S_y \end{bmatrix} \quad \mathbf{LO^B} = \frac{1}{\sqrt{2}} \begin{bmatrix} LO_x e^{j\rho_{LOB}} \\ LO_y \end{bmatrix} \end{aligned} \tag{4.15}$$

In order to recover the originally transmitted symbols, the phase shifts should ideally fulfill the condition [21, 23, 130]:

$$\phi_{Dist} = (\rho_{SA} - \rho_{LOA}) - (\rho_{SB} - \rho_{LOB}) = (2p+1) \cdot \pi, \quad p = 0, 1, \ldots \tag{4.16}$$

As long as this condition is satisfied, perfect dual-polarization demodulation is performed. If this condition is not satisfied the demodulation will be performed, but in that case a degradation in the sensitivity is produced [130]. Figure 4.5 illustrates this degradation as a function of the differential phase shift error, which is defined as $\varepsilon_{\phi_{Dist}} = 180° - \phi_{Dist}$.

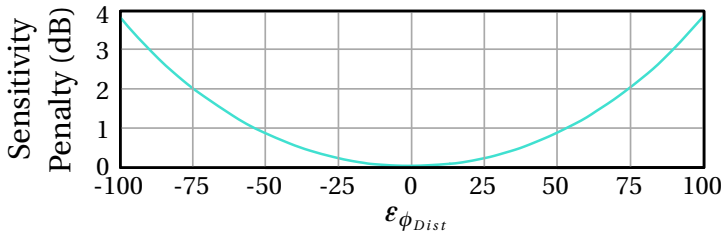

Figure 4.5.: Sensitivity as function of the differential phase shift error ($\varepsilon_{\phi_{Dist}}$).

Table 4.1 shows the signals obtained at the output of the downconverter, and their combinations to correctly retrieve the original transmitted signals, for different scenarios of the polarization phase shift combinations.

In order to easily illustrate the working principle, we will set ρ_{LOA}, ρ_{SB}, ρ_{LOB} to 0, and ρ_{SA} to π, as depicted in figure 4.4 b) so that the above condition is satisfied. For the sake of clarity we will assume $LO_x = LO_y = 1$. Equation 4.15 then reads:

$$\mathbf{S^A} = \frac{1}{\sqrt{2}}\begin{bmatrix} S_x e^{j\pi} \\ S_y \end{bmatrix} \quad \mathbf{S^B} = \frac{1}{\sqrt{2}}\begin{bmatrix} S_x \\ S_y \end{bmatrix} \quad \mathbf{LO^A} = \frac{1}{\sqrt{2}}\begin{bmatrix} 1 \\ 1 \end{bmatrix} \quad \mathbf{LO^B} = \frac{1}{\sqrt{2}}\begin{bmatrix} 1 \\ 1 \end{bmatrix} \tag{4.17}$$

These four signals, grouped in two pairs, are the inputs for the IQ downconverters. Hence, the analysis performed in section 4.3.1 can be applied to each IQ downconverter. The inputs of each downconverter are $\mathbf{S^A}$ together with $\mathbf{LO^A}$, and $\mathbf{S^B}$ together with $\mathbf{LO^B}$. Thus, equation 4.10 applied to each downconverter is:

$$\begin{aligned} \text{Downconv. A:} &\begin{cases} I^A_{DE} = \frac{R}{2}\left(\sqrt{P_{S_x}}\cos\left(\theta_{S_x}+\pi\right)\right) + \frac{R}{2}\left(\sqrt{P_{S_y}}\cos\left(\theta_{S_y}\right)\right) \propto -I_x + I_y \\ Q^A_{DE} = \frac{R}{2}\left(\sqrt{P_{S_x}}\sin\left(\theta_{S_x}+\pi\right)\right) + \frac{R}{2}\left(\sqrt{P_{S_y}}\sin\left(\theta_{S_y}\right)\right) \propto -Q_x + Q_y \end{cases} \\ \text{Downconv. B:} &\begin{cases} I^B_{DE} = \frac{R}{2}\left(\sqrt{P_{S_x}}\cos\left(\theta_{S_x}\right)\right) + \frac{R}{2}\left(\sqrt{P_{S_y}}\cos\left(\theta_{S_y}\right)\right) \propto I_x + I_y \\ Q^B_{DE} = \frac{R}{2}\left(\sqrt{P_{S_x}}\sin\left(\theta_{S_x}\right)\right) + \frac{R}{2}\left(\sqrt{P_{S_y}}\sin\left(\theta_{S_y}\right)\right) \propto Q_x + Q_y \end{cases} \end{aligned} \tag{4.18}$$

Again, the output IQ signals in each downconverter are an aggregate of the IQ signals from both polarizations. However, this combination is not the same for both downconverters, so the original IQ signals can be retrieved by linearly combining this four outputs as shown in table 4.1 Scenario B. Nevertheless, in practice, there is no need to explicitly combine the signals: the same algorithms that the DSP employs to compensate for the arbitrary polarization rotation along the fiber will realize this combination [21]. Hence, this architecture not only enables polarization diversity avoiding the use of PBS, but also employs the same DSP algorithms that are already used in conventional dual polarization coherent receivers. A more detailed analysis of the PBS-Less scheme, regarding SNR penalty, can be found in [130].

Figure 4.4 c) shows another combination of polarization phase shifts. This option is advantageous from an implementation point of view, as will be explained in next sections. For this implementation, the outputs of the polarization diversity network are:

	Polarization Phase Shift	Downconverter Outputs	Outputs Combination
Scenario A	$\rho_{SA}=0 \quad \rho_{LOA}=0$ $\rho_{SB}=0 \quad \rho_{LOB}=0$	$I^A_{DE} \propto I_x + I_y$ $Q^A_{DE} \propto Q_x + Q_y$ $I^B_{DE} \propto I_x + I_y$ $Q^B_{DE} \propto Q_x + Q_y$	There is no way to recover I_x, Q_x, I_y, Q_y from the downconverter outputs
Scenario B	$\rho_{SA}=\pi \quad \rho_{LOA}=0$ $\rho_{SB}=0 \quad \rho_{LOB}=0$	$I^A_{DE} \propto -I_x + I_y$ $Q^A_{DE} \propto -Q_x + Q_y$ $I^B_{DE} \propto I_x + I_y$ $Q^B_{DE} \propto Q_x + Q_y$	$I_x \propto I^B_{DE} - I^A_{DE}$ $Q_x \propto Q^B_{DE} - Q^A_{DE}$ $I_y \propto I^B_{DE} + I^A_{DE}$ $Q_y \propto Q^B_{DE} + Q^A_{DE}$
Scenario C	$\rho_{SA}=0 \quad \rho_{LOA}=\frac{\pi}{2}$ $\rho_{SB}=\frac{\pi}{2} \quad \rho_{LOB}=0$	$I^A_{DE} \propto Q_x + I_y$ $Q^A_{DE} \propto -I_x + Q_y$ $I^B_{DE} \propto -Q_x + I_y$ $Q^B_{DE} \propto I_x + Q_y$	$I_x \propto Q^B_{DE} - Q^A_{DE}$ $Q_x \propto I^A_{DE} - I^B_{DE}$ $I_y \propto I^A_{DE} + I^B_{DE}$ $Q_y \propto Q^B_{DE} + Q^A_{DE}$

Table 4.1.: In this table, each row shows a different configuration of the polarization diversity network shown in figure 4.3 a). Scenario A shows a combination of polarization phase shifts that does not satisfy equation 4.16. Conversely scenarios B and C satisfy equation 4.16, and the original IQ transmitted signals can be recovered. Scenario B is proposed for the principle of operation explanation, while scenario C is shown as it will be the chosen configuration for the implementation, as discussed in the next section.

$$\mathbf{S^A} = \frac{1}{\sqrt{2}}\begin{bmatrix} S_x \\ S_y \end{bmatrix} \quad \mathbf{S^B} = \frac{1}{\sqrt{2}}\begin{bmatrix} S_x e^{j\pi/2} \\ S_y \end{bmatrix} \quad \mathbf{LO^A} = \frac{1}{\sqrt{2}}\begin{bmatrix} e^{j\pi/2} \\ 1 \end{bmatrix} \quad \mathbf{LO^B} = \frac{1}{\sqrt{2}}\begin{bmatrix} 1 \\ 1 \end{bmatrix} \tag{4.19}$$

The theoretical calculation of the outputs of the PBS-Less downconverter for this configuration yields:

$$\begin{aligned} \text{Downconv. A:} &\begin{cases} I^A_{DE} \propto Q_x + I_y \\ Q^A_{DE} \propto -I_x + Q_y \end{cases} \\ \text{Downconv. B:} &\begin{cases} I^B_{DE} \propto -Q_x + I_y \\ Q^B_{DE} \propto I_x + Q_y \end{cases} \end{aligned} \tag{4.20}$$

It is observed that the outputs of the downconverters for this polarization phase shift configuration are different from the previous configuration. However, it is possible to similarly combine them, as depicted in table 4.1 Scenario C, and obtain the

original IQ signals. In the next section an implementation of a PBS-Less downconverter, with this polarization phase shift combination is presented.

4.5. PBS-Less dual polarization downconverter design

In this section the design of the PBS-Less dual polarization downconverter is presented. After introducing the photonic fabrication platform, the design of the polarization diversity network and the IQ downconverters will be described. The polarization diversity network, which has been schematically depicted in figure 4.4 a), is composed of two beam splitters, each one implemented with a 1×2 MMI, and four polarization phase shifters, implemented with birefringent waveguides. By judiciously design the birefringence and the length of these waveguides, the polarization phase shift needed for the correct operation of the device is obtained. The IQ downconverters are implemented with 2×4 MMIs, so an output network is required to properly interconnect the MMI's outputs with the photodidodes' input, as shown in figure 4.2 b).

4.5.1. The HHI InP photonic platform

To implement the PBS-Less downconverter, the chosen integrated photonic platform has to meet some specific requirements:

- High-speed polarization independent photodiodes (i.e. 40 to 60 GHz bandwidth).
- Polarization independent fiber to chip couplers.
- Birefringent monomode waveguides, for the polarization phase shifters implementation.
- Low birefringent multimode waveguides, to implement polarization independent multimode interferometers

Among the main integrated photonics platforms, i.e. Silicon (Si) or Indium Phosphide (InP), InP is the better suited candidate in order to meet the specified requirements. For our application the high index contrast of Si platforms makes challenging the design of polarization independent devices, i.e photodiodes and MMIs, which are key elements for the operation of the device. However, InP platforms satisfy most of the specified requirements: high speed polarization independent photodiodes and high performance polarization insensitive fiber coupling have already been demonstrated [151] while polarization insensitive behavior of MMIs was reported [159] long ago. Furthermore the research group holds prior experience in the design of InP photonic devices.

Many InP photonics platforms are available in Europe, such as Oclaro, HHI and COBRA [160]. For prototyping purposes, these platforms are usually accessed through multi-project wafer (MPW) runs, where the InP wafer is divided into many user areas that are shared among several customers, thus reducing the fabrication unitary cost.

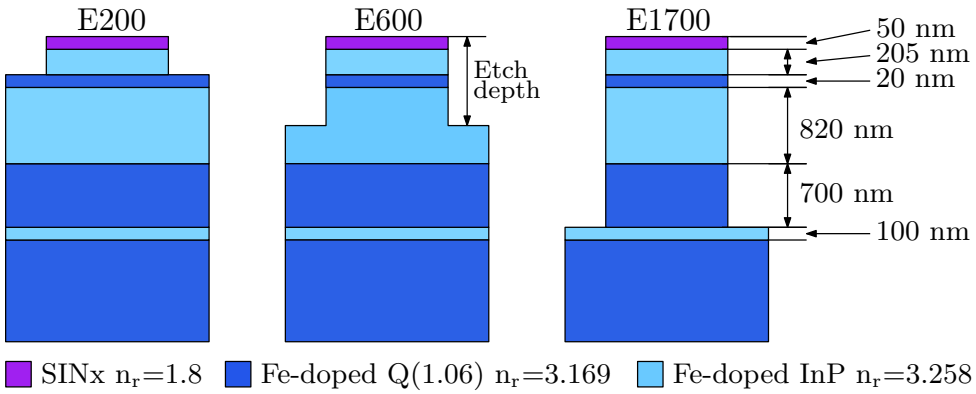

Figure 4.6.: Waveguides offered in the InP HHI platform.

However, MPW platforms establish design rules that ultimately constrain the design, as will be detailed in the next section.

For our design, HHI InP photonic platform is chosen as the research group has previously developed successful projects in this platform [158, 161]. Furthermore, polarization independent high speed photodiodes and low insertion losses fiber to chip couplers, are available in this platform.

HHI InP offers three different etch depths for the waveguides, as depicted in figure 4.6 a). E200 waveguides are mostly used for photodiode and fiber-to-chip couplers, however its low modal confinement makes it an undesired option to implement waveguide curves as the required curve radii are in the order of mm, being discarded for the receiver design. Alternatively, E600 and E1700 are used for passive components such as interconnecting waveguides, waveguide tapers, multimode interferometers, etc. The election between E600 and E1700 depends on the application, while E600 exhibits better fabrication tolerances in waveguide widths than E1700 (50 nm vs. 100 nm) its lower modal confinement results in a lower capacity of integration [162].

4.5.2. Design Considerations

Before going further into the different subsystems it is worth to consider the main design constraint: the maximum length of the user area in the MPW run, that is limited to 6 mm, because of the fiber to chip couplers fabrication process. Thus, in our case the total purchased area is $3 \times 6\,\text{mm}^2$.

To estimate the arrangement of the different subsystems composing the receiver, a preliminary schematic of the receiver layout is shown in 4.7. Within the total available area, fiber-to-chip couplers (1.2 mm long), photodiodes (1 mm long) and waveguides etch depth converters (0.2 mm long) have to be included, reducing the longitudinal available space from 6 to 3.4 mm [162].

As can be observed in 4.7 the layout is divided into three different parts: polarization diversity network (I), 90º hybrids (II) and output network (III). In this preliminary layout it can be checked that both I and III regions contains several waveguide curves. In total two 90° waveguide bends are needed in I, while III contains two 45° waveguide

bends and a 90° waveguide bend (estimated based on previous experience in the design of output networks), so at least, a longitudinal space of four times the bending radius is needed for the waveguide bending. According to the design manual, the recommended waveguide bent radii are 250 μm and 480 μm for E1700 and E600 waveguide etch depth, respectively. This makes prohibitive the use of E600 waveguide etch depth, as there is not enough space for the design of the rest of elements. For this reason E1700 waveguides are chosen to implement our design.

Several subsystems composing the receiver, such as the photodiodes, the fiber to chip couplers, transitions between E200 and E1700 etch depth, are taken from the foundry building block library, while the rest are designed in this work:. 2×4 MMI, crossings, bends, 1×2 MMI, tapers ... as detailed in figure 4.7.

4.5.3. Polarization diversity network design

Two different subsystems compose the polarization diversity network: the beam splitters and the polarization phase shifters. Beam splitters are implemented through 1×2 MMIs, while the polarization phase shifters includes the design of birefringent waveguides and its interconnection elements, namely waveguide crossing and curves, as depicted in figure 4.7. In this subsection the layout of the polarization diversity network is described and then the process design of each element composing the polarization diversity network is detailed.

4.5.3.1. Polarization diversity network layout design

The birefringent waveguides are the core element of the polarization diversity network, and will simultaneously induce the required polarization phase shift and connect the beam splitters outputs to the downconverters inputs. The birefringence of a waveguide is defined as the difference between the propagation constants of the horizontal (x) and vertical (y) on-chip states of polarization:

$$B = \beta_x - \beta_y \tag{4.21}$$

Thus, the polarization phase shift induced in a waveguide, ρ, depends on its birefringence, B, and its length, L, according to the following expression:

$$\rho = BL \tag{4.22}$$

In order to meet the generic phase shift condition described in the previous section (4.16) different alternatives can be taken, such as maintain the length of the waveguides and modify their birefringence or vice-versa. In this design, the waveguide birefringence is chosen to be the same, so the polarization phase shift is induced by controlling the waveguide length, as depicted in figure 4.8.

Provided the beam splitter and the IQ downconverter positions, the simplest and best solution is to implement a symmetric network, as shown in figure 4.8, where $L_{SA} = L_{LOB}$ and $L_{SB} = L_{LOA}$. Furthermore, it can be demonstrated that this symmetric approach includes some advantages regarding the tolerance to fabrication deviations, and saving spacing in the longitudinal dimension. Thus, each of the four paths contains the same elements: four waveguide tapers, two 90° bends, one waveguide

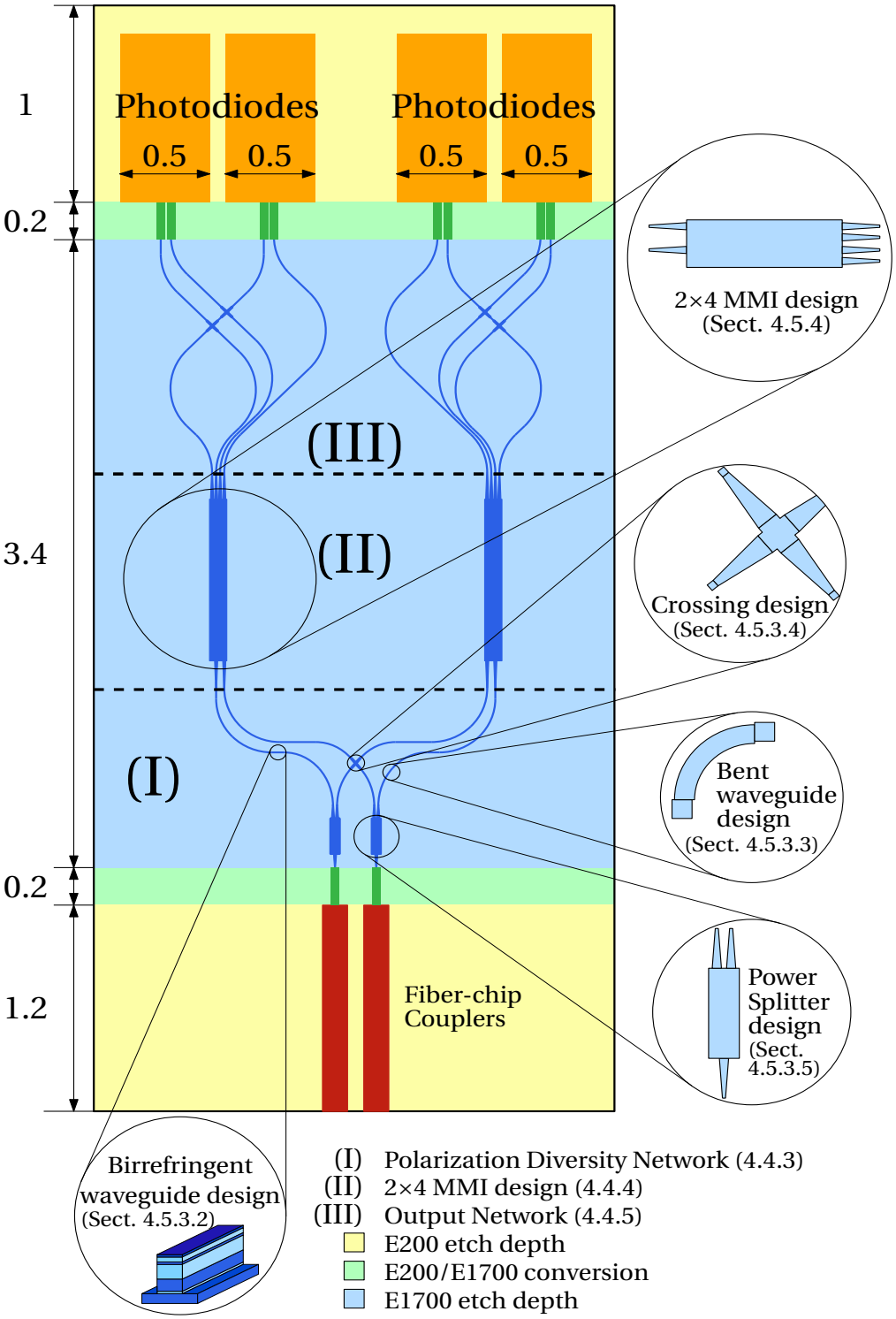

Figure 4.7.: Schematic view of the preliminary PBS-Less receiver layout, including the three main parts of the design and a detailed view of some of the designed elements together with the section in which the design is detailed.The total area is $3 \times 6\,\mathrm{mm}^2$.

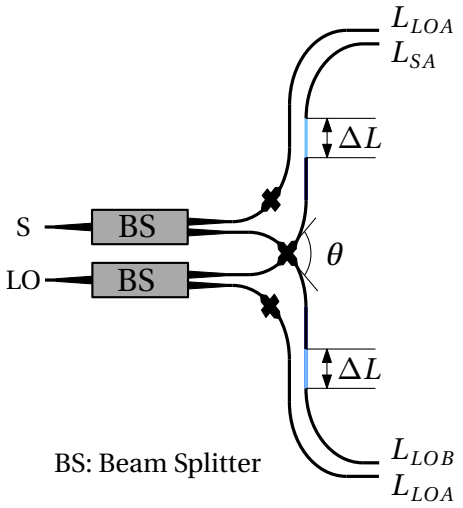

Figure 4.8.: Schematic layout of the polarization diversity network. The polarization phase shift is induced by the differential length between the interconnecting waveguides. L_c is the length of the common elements appearing in each path.

crossing and a straight waveguide with variable length: in the paths $L_{SA}$and L_{LOB} crossing the length is L, while in L_{SB} and L_{LOA}, this length is set to $L+\Delta L$.

Thus, the mentioned phase shift condition can be particularized for the proposed layout, being expressed as a function of the differential length:

$$\phi_{Dist} = 2B\Delta L = \pi \tag{4.23}$$

where B is the birefringence of the four waveguides, dependent on the waveguide width, and ΔL is the differential length (see figure 4.8). For perfect operation, the differential waveguide length, ΔL, can be expressed in terms of the birefringence: $\Delta L = \pi/2B$, so the design of the polarization phase shifters is reduced to the choice of the waveguide width.

4.5.3.2. Birefringent waveguides design

Figure 4.9 shows the birefringence of the simulated E1700 waveguide, in this figure it can be observed that as the waveguide increases, the calculated birefringence is higher and less sensitive to variations in waveguide width, resulting in a more compact and tolerant design. However, there is another constraint that have to be taken into account: for wider waveguides the second order mode is not cut-off, which ultimately can damage the operation of the device. Thus, the chosen waveguide width should be a trade-off between high birefringence, low sensitivity to fabrication deviations, and monomode operation.

First of all, the maximum waveguide width is analyzed using the commercial tool Fimmwave [163], in order to ensure that the second order mode in the worst case is sufficiently attenuated. Figure 4.10 a) shows the leakage losses for TE and TM polarization of the second order mode as a function of the waveguide width. It is shown that for the nominal width recommended in the designer manual, 2 µm, the leakage

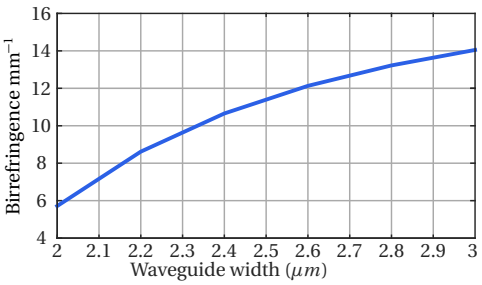

Figure 4.9.: Birefringence of the E1700 waveguide as a function of the waveguide width.

losses are around 160 dB/cm, while for widths higher than 2.8 µm the leakage losses are negligible. On other side, regarding the effective index of the second order mode, it can be observed in figure 4.10 b) that the effective index is lower than the minimum refractive index of the stack layer (3.169) for widths lower than 2.8 µm which roughly indicates that the mode is almost radiated/low confined. Taking in to account that in a real scenario the propagation losses are expected to be higher due to the waveguide roughness, and being conservative, the waveguide width has been established to 2.4 µm. For this width, figure 4.10 c) and d), shows the intensity of the fundamental and the second order mode. As can be observed, for this width the second order mode has a very low confinement, which in practice will rather limit is propagation. For this width, the birefringence value is 10.6 mm^{-1} so the differential waveguide length, ΔL that produces the required polarization phase shift is 147 µm (calculated from equation 4.23).

The next step is to analyze the impact of the fabrication tolerances on the birefringence around the chosen waveguide width. Figure 4.11 a) shows the main sources of fabrication deviations on the E1700 waveguide: the waveguide width, that similarly affects to the whole layer stack, and errors due to the epitaxial growth, that only affect to the thickness (t_{FeQ}) and refractive index (n_{FeQ}) of the intermediate Fe-Doped layer, red-colored in 4.11 a). According to the design manual, errors in waveguide width are in the range ± 100 nm, while for the intermediate Fe-Doped layer the nominal thickness is 820 nm with ± 5 % variation, and its refractive index is 3.258 riu , with a variation of ± 0.004 riu.

Figure 4.11 b) shows the birefringence variation range as a function of the waveguide width, considering the different error sources. It can be inferred that errors in waveguide width have an stronger impact on birefringence as the waveguide width diminishes. Figure 4.11 c) shows for each value of the waveguide width the maximum birefringence deviation, calculated taking into consideration the influence of different error sources and plotting the worst case (maximum deviation).

As the differential length is fixed, deviations in the birefringence will induce a differential phase shift error $\varepsilon_{\phi_{Dist}}$, defined in 4.4. This differential phase shift error can be expressed in terms of the birefringence (B) and its deviation (ΔB):

$$\varepsilon_{\phi_{Dist}} = \pi \frac{\Delta B}{B} \tag{4.24}$$

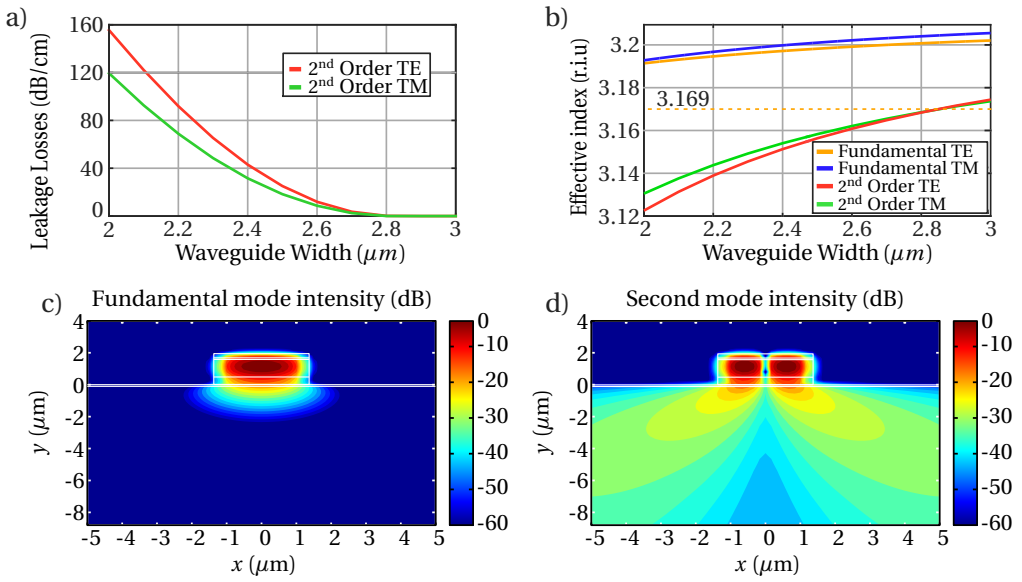

Figure 4.10.: a) Second order leakage mode losses as a function of the waveguide width. b) Effective index of the fundamental and second order modes, for both polarizations. c) Intensity of the fundamental TE mode d) Intensity of the second order TE mode. The waveguide width in c) and d) is 2.4µm.

The differential phase shift error $\varepsilon_{\phi_{Dist}}$ that can be achieved is shown in figure 4.11 c) (right axis) as a function of the waveguide width. For the established waveguide width (2.4 µm), the maximum differential phase shift error is 45°. This differential phase shift error can be mapped on sensitivity penalty using figure 4.5. For the chosen waveguide width, the maximum sensitivity penalty is around 1 dB.

Finally, provided the trade-off between monomode operation, low sensitivity to fabrication deviations and high birefringence, the chosen waveguide width is 2.4µm. For this width, the second order mode is expected to have around 40 dB/cm propagation losses, the birefringence deviation its lower than 3 mm^{-1} and its value is 10.6 mm^{-1}, requiring ΔL to be 147µm in order to produce the required polarization phase shift.

4.5.3.3. Bent waveguide design

To design the bend, we will study the system schematically depicted in figure 4.12 a), composed by an input straight waveguide, a bent waveguide, and an output straight waveguide. A bent waveguide can be modeled as a perturbed straight waveguide, in which the refractive index suffers a transformation [164]. This linear transformation leads the modes of the bent waveguide to be different from the modes propagating along the straight waveguide, as depicted in figures 4.12 b) and c). Consequently, when a bent waveguide is excited with the fundamental mode of its straight counterpart, both its fundamental and higher order modes are excited. Then, during the propagation along the bent waveguide these modes will be beaten and, depending on the bend length, a certain fraction of the input power will excite the output wave-

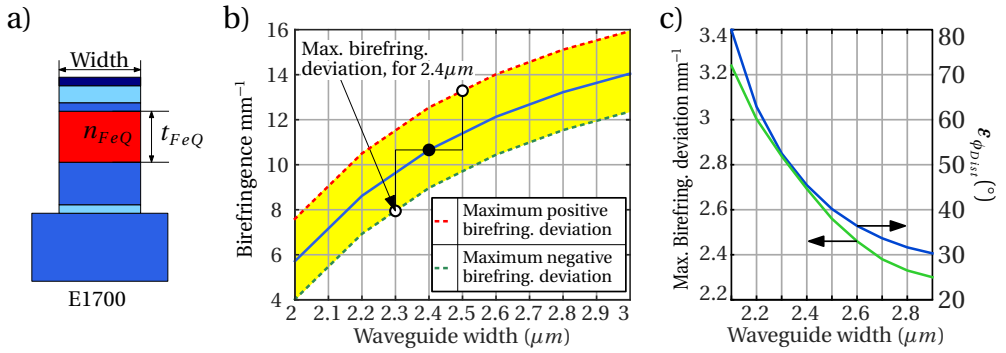

Figure 4.11.: a) E1700 HHI waveguide, including the main sources of errors during the fabrication process. b) Birefringence of the E1700 waveguide as a function of the waveguide width, considering variations in the effective index and thickness of the intermediate Fe doped layer (n_{FeQ}, t_{FeQ}). c) Worst case variation in the birefringence for each value of the waveguide width, and its corresponding differential phase shift error.

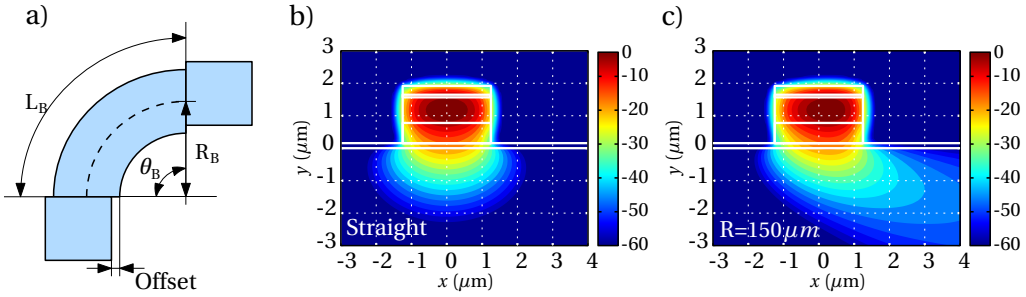

Figure 4.12.: a) Schematic view of a bent waveguide. b) Fundamental TE mode profile of the E1700 straight waveguide. c) Fundamental TE mode profile of the E1700 bent waveguide, for radius of 150µm.

guide higher order modes. Besides the problem of the second order mode excitation, a bent waveguide also presents insertion losses that essentially come from the transition losses, due to the mode mismatching between the straight and bent waveguides, and the bending radiation losses, that models the power radiated along the waveguide bent.

An ideal waveguide bent should present low insertion losses and low second order mode excitation. While the radiation losses are minimized by choosing a bend radius (R_B) large enough, the excitation of the second order mode and the mode mismatching are minimized by introducing an offset between the input and output waveguides and the bent waveguide.

The bent waveguide design procedure is as follows: First of all the radius and width of the waveguide are chosen in order to ensure low radiation losses. Then, the value of the offset is swept, extracting the value of second order mode excitation for both polarizations. Finally, the offset that minimizes the second order mode in both polar-

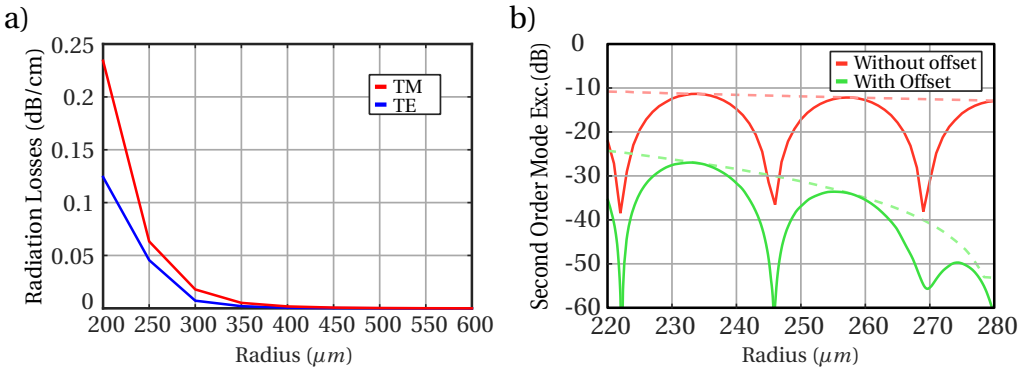

Figure 4.13.: a) Radiation losses as a function of the bend radius, for both polarizations. b) Excitation of the second order mode, as a function of the bend radius, when the optimum offset (115 nm) is set, for a radius of 250 μm and a width of 2.4 µm.

izations is chosen. It is worth to mention that for this optimum offset, the insertion losses of the waveguide bent are inherently minimized.

The radiation losses of a 2.4 µm wide bent waveguide, are shown in figure 4.13 a). It is observed that radiation losses are very low for radii in the range of interest (200 µm to 300 µm) and negligible for radii higher than 300 µm. Regarding the second order mode excitation, figure 4.13 b) shows the improvement that is achieved by judiciously set the offset between the straight and bent waveguides for the nominal design, i.e. waveguide width of 2.4 µm and a bending radius of 250 µm. In this case, it is shown for the TE polarization a reduction of almost 20 dB in the second order mode TE excitation, with an input offset of -115 nm. For this offset, the total insertion losses are below 0.2 dB per 90° bent.

This procedure is repeated for different radius and different waveguide widths, and the main results are included in the next table (table 4.2).

Radius (µm) \ Width (µm)	2	2.1	2.2	2.3	2.4
200	-70	-85	-105	-120	-145
250	-60	-70	-80	-100	-115
300	-50	-60	-70	-80	-95

Table 4.2.: Optimum offset (nm) for different waveguide bend radii and widths.

4.5.3.4. Crossing design

Provided the distribution of the polarization diversity network, see figure 4.8, it is unavoidable to employ waveguide crossings. Different waveguide crossings implementation alternatives are presented in the bibliography, such as [165, 166]. However, for our design a more simple alternative, which consist in widening the crossing waveguides, is used. The schematic of the waveguide crossing is depicted in figure 4.14 a), being defined by its waveguide width, W, and its crossing angle, θ_X. Waveguide tapers

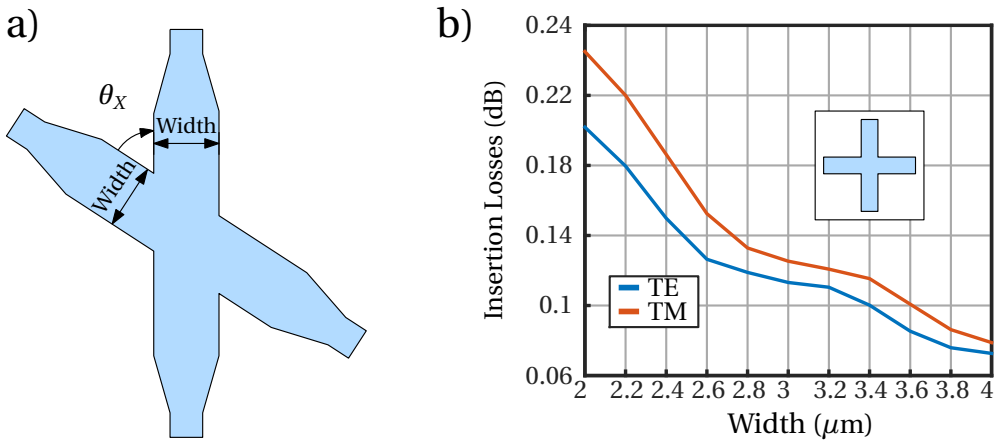

Figure 4.14.: a) Schematic view of a waveguide crossing. b) Insertion losses of a waveguide crossing with θ_X=90°, as a function of the waveguide and cross waveguide widths.

are also a part of the crossing design, but its design is described in section 4.5.3.6.

In waveguide crossings it is of fundamental importance to avoid crosstalk between the waveguides while maintaining low insertion losses. The design of the waveguide crossing have been done in two different steps:

In a first step we simulate a waveguide crossing with θ_X = 90°, for different waveguide widths, in order to find the width that minimizes the insertion losses. Figure 4.14 b) shows the insertion losses as a function of the crossing waveguide width. From this step, we set the crossing waveguide width to 4 micrometers.

The second step is to simulate the waveguide crossing in order to evaluate the crosstalk and the second order mode excitation. In these simulations, they have been evaluated for different crossing angles. Figure 4.15 shows the results of these simulations. Thus, crossing angles in the range 90° to 60° the values of crosstalk and second order mode excitation are below 20 and 40 dB respectively, while the insertion losses are below 0.15 dB. Consequently, the waveguide width for the crossing angle is set to 4µm, while the angle will be in the range 90° to 60° (the exact value will be given in the layout section).

4.5.3.5. 1 × 2 MMI design

The 1 × 2 MMIs are used to implement the beam splitters, located at the input of the polarization diversity network. As depicted in figure 4.16, it is composed of one input and two outputs. It is worth to mention that, for our application polarization independent operation is desired.

To design the 1x2 MMI, a general procedure for MMI design [167] is followed. First of all, the excitation type, that defines the interference mechanism [159], is chosen. For 1x2 MMIs, the best option is the symmetric interference mechanism, as the length of the MMI is minimized with respect to the other alternatives, and both outputs are in phase. Following the procedure, the width of the input and output waveguides

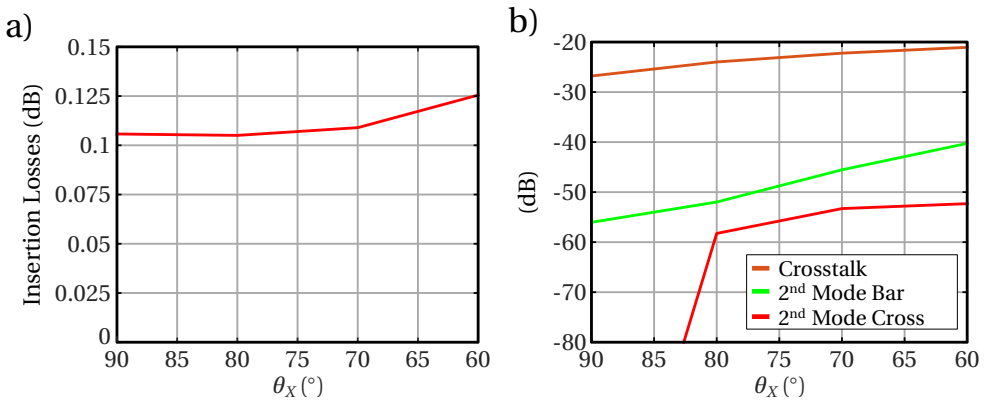

Figure 4.15.: a) Insertion losses of a waveguide crossing as a function of the crossing angle, θ_X, for a 4µm waveguide width. b) Crosstalk and second order mode excitation as a function of the crossing angle, for a 4µm waveguide width.

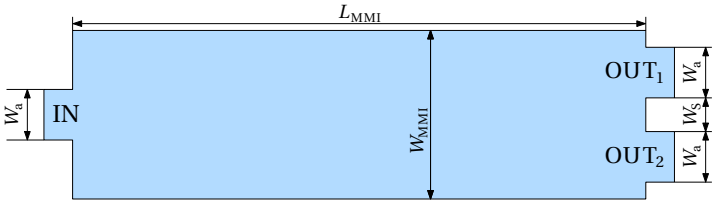

Figure 4.16.: Schematic view of a 1x2 symmetric MMI.

(W_a) and the separation between the waveguides (W_s) are then chosen: W_a is set to 3µm, as it is a good compromise between device compactness and insertion losses, while W_s is set to 1.5µm, adopting a conservative strategy, as the recommended minimum gap between waveguides is 1µm. For this separation, no coupling between the output waveguides is observed. The MMI width (W_{MMI}) can be expressed in terms of W_a and W_s, as for symmetric excitation the separation between the two replicas is $W_{MMI}/2$, so: $W_{MMI} = 2(W_a + W_s)$ [168]. Finally the MMI length (L_{MMI}) can be estimated from from its width [159]:

$$L_{MMI} = \frac{4 n_r W_{MMI}^2}{3\lambda_0} \tag{4.25}$$

with n_r the effective refractive index of the multimode region. Thus, the theoretic values of W_{MMI} and L_{MMI} are 9µm and 84µm respectively.

Typical figures of merit for beam splitters are the imbalance and the excess losses, however due to the symmetry of the proposed device the imbalance is null, and will not be considered. The excess losses are defined as the fraction of input the power that is not transferrer to any output, expressed as a function of the S-parameters:

$$\mathrm{EL(dB)} = -10\log_{10}\left(\sum_j |S_{j1}|^2\right) \tag{4.26}$$

with $j = 2, 3$.

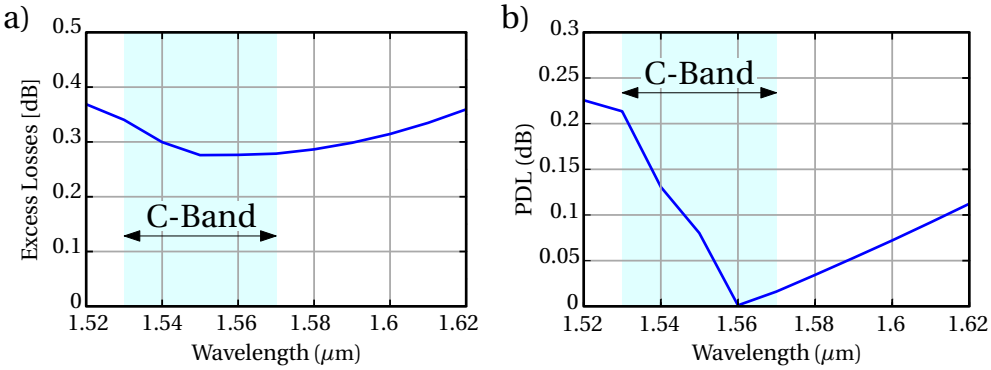

Figure 4.17.: a) Excess Losses of the designed 1x2 MMI, as a function of the wavelength. b) Polarization dependent losses (PDL) of the designed 1x2 MMI, as a function of the wavelength

For our purpose, we will also consider an additional figure of merit, the polarization dependent losses, that will be defined as:

$$PDL(dB) = |EL_{TE}(dB) - EL_{TM}(dB)| \tag{4.27}$$

At this point, the whole device is simulated using Fimmprop [163], varying the values of both L_{MMI} and W_{MMI} in the range 8.5µm to 9.5µm and 70µm to 90µm, respectively. From these simulations, we conclude that the optimum values, in terms of EL and PDL, of L_{MMI} and W_{MMI} are 86µm and 9.1µm, respectively. These values are rather close to the theoretically obtained. Finally, for these dimensions, a wavelength analysis is performed. The results of this analysis are shown in figure 4.17 a) and b), showing excess losses below 0.35 dB and polarization imbalance below 0.25 dB in the full C-Band.

4.5.3.6. Taper design

Waveguide tapers are of fundamental importance in order to obtain adiabatic transitions between different waveguides. In our design, they are used to adapt the width of the interconnecting waveguides and:

- Crossings (4µm width)
- 1 × 2 MMIs inputs and outputs (3µm width)
- 2 × 4 MMIs inputs and outputs (4µm width)

The width of the interconnecting waveguides is 2.4µm in the polarization diversity network, and 2µm in the output network (section 4.5.5.2). For our purpose a linear taper is chosen to properly adapt the different widths, as it is the simplest alternative. The schematic of a linear taper is shown in figure 4.18 a). This taper is defined by the input and output waveguide widths, W_{in} and W_{out}, respectively, and the length of the taper, L_{taper}.

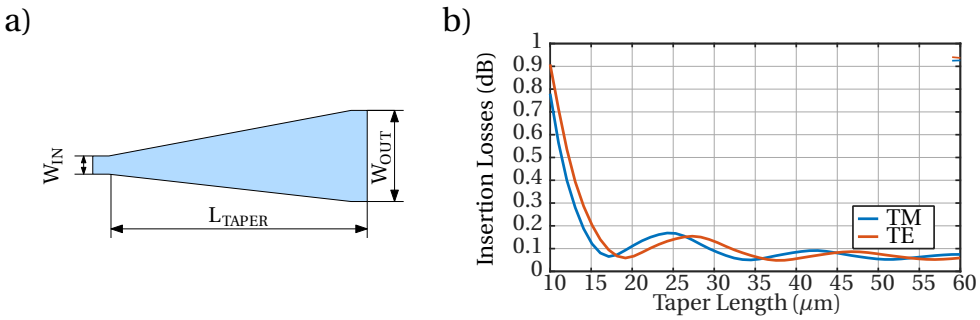

Figure 4.18.: a) Schematic view of a waveguide width taper. b) Insertion losses of a 2 µm to 4 µm waveguide width taper, as a function of its length.

In order to simplify the receiver design process, a single taper adapting 2 µm to 4 µm waveguide widths is designed. The value of W_{out} is fixed by the crossing design and the 2 × 4 MMI inputs and outputs, while for W_{in}, the recommended waveguide width is chosen, because it will be used in the output network, as explained in section 4.5.5.2. As all the required transitions are less abrupt than the designed one, the same taper is used in all the transitions of the receiver.

The design process of this taper is very simple, as only requires to modify the length of the taper until the insertion losses are reduced. Figure 4.18 b) shows the taper insertion losses as a function of the taper length. For our design, 40µm is chosen as the length of the taper, ensuring insertion losses below 0.1 dB and negligible polarization dependent losses.

4.5.4. 2 × 4 MMI design

The 2 × 4 MMI, is used to implement the 90º hybrids. As previously commented, it consist of a 4 × 4 MMI, in which only two inputs are used. The design process will be similar to the employed with the 1 × 2, except for the interference mechanism, that in this case is the general interference mechanism [159]. The schematic draw of the 2 × 4 MMI is depicted in figure 4.19. Following the same design process, W_a and W_s are firstly chosen: W_s is set to 1.5µm, adopting the same conservative strategy that was used for the 1 × 2 MMI design, while W_a is set to 4µm in order to further reduce the insertion losses [169]. For general excitation, the spacing between images is W/N, where N is the number of images of the device, so W_{MMI} can be expressed in terms of W_a and W_s: $W_{MMI} = 4(W_a + W_s)$ [168]. Again, L_{MMI} can be estimated from W_{MMI} using equation 4.25, being respectively 22µm and 990µm.

Before going further into the optimization of the 2 × 4 MMI design, its typical figures of merit, which are the excess losses, the imbalance, the phase error and the common mode rejection ratio, are defined:

- The excess losses (EL) are defined as the amount of power from any input i that is not transferred to any output j. Thus, the EL of the device is defined as the maximum EL for any input. It can be expressed in terms of the device

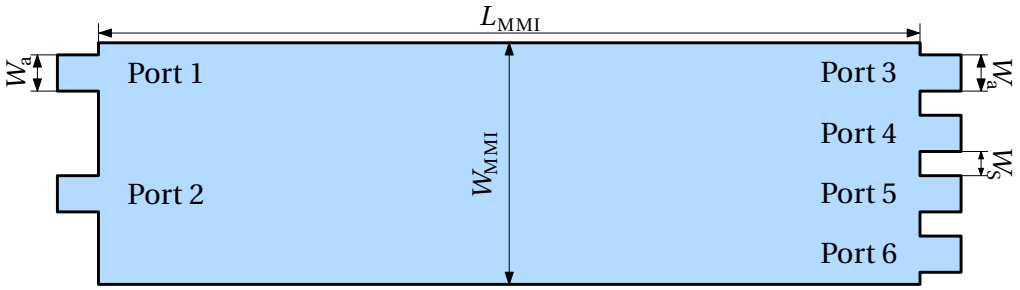

Figure 4.19.: Schematic view of the 2×4 MMI, based on general interference mechanism.

S-parameters, as:

$$\mathrm{EL(dB)} = \max_{\mathrm{i}}\left\{-10\log_{10}\left(\sum_{\mathrm{j}}\left|S_{ji}\right|^2\right)\right\} \tag{4.28}$$

where $i = 1,2$ and $j = 3,4,5,6$.

- For each input i, the imbalance (IB) represents the power difference between two outputs, j and k. The imbalance of the device is also defined as the maximum imbalance, between any input and two any outputs. It is defined as a function of the S-parameters as follows:

$$\mathrm{IB(dB)} = \max_{i,j,k}\left\{10\log_{10}\left(\left|S_{ji}\right|^2/\left|S_{ki}\right|^2\right)\right\} \tag{4.29}$$

where $i = 1,2$, $k, j = 3,4,5,6$ with $k \neq j$.

- The phase error (PE) is defined as the phase deviation from the ideal relative phase [159], that two waves coming from the different inputs combines at the same output, j. As the previous parameters, the phase error of the device is defined as the maximum phase error:

$$\mathrm{PE}(^\circ) = \max_{j}\left\{\angle\frac{S_{j1}}{S_{j2}} - \phi_j\right\} \tag{4.30}$$

where $j = 3,4,5,6$ and ϕ_j is the ideal relative phase. For our 2×4 MMI, the ideal relatives phases are: $\phi_1 = 0^\circ$, $\phi_2 = 90^\circ$, $\phi_3 = 270^\circ$, $\phi_4 = 180^\circ$, [150, 159].

Together with these figures of merit, a fourth one is defined for our particular application: the common mode rejection ratio (CMRR). The CMMR is defined by the OIF in its implementation agreement [20] and applies to the whole receiver. However, assuming an ideal output network and ideal photodiodes, the CMRR strongly depends on the 2×4 MMI CMRR:

$$\mathrm{CMRR}_i^{\mathrm{I}}(dB) = 10\log_{10}\left(\frac{\left||S_{6i}|^2 - |S_{3i}|^2\right|}{|S_{6i}|^2 + |S_{3i}|^2}\right) \tag{4.31}$$

$$\mathrm{CMRR}_i^{\mathrm{Q}}(dB) = 10\log_{10}\left(\frac{\left||S_{5i}|^2 - |S_{4i}|^2\right|}{|S_{5i}|^2 + |S_{4i}|^2}\right) \tag{4.32}$$

where $i = 1,2$ and I and Q stands for the In-Phase and Quadrature components. The CMRR of the device is the maximum CMRR, defined as:

$$\mathrm{CMRR}(dB) = \max_i\left\{\mathrm{CMRR}_i^{\mathrm{I}}(dB), \mathrm{CMRR}_i^{\mathrm{Q}}(dB)\right\} \tag{4.33}$$

Two different observations can be made from these expressions: the first one is that the CMRR is highly related with the imbalance, the better the imbalance, the better the CMRR. The second one is that provided that the photodiodes are in balanced configuration, the CMRR represents the dynamic range of the balanced photodiodes output signals, as is defined as the ratio between the optical signals that achieve the maximum and the minimum electrical signals of the photodiode.

It is worth to mention that all the figure of merits here presented have to be evaluated for both polarizations. Thus, the initial geometry of the MMI is simulated, and then for both polarizations the length and width are optimized in order to obtain the best performance in the full C-Band. In this case the optimum L_{MMI} and W_{MMI} are 982 and 21.7 μm, respectively. Figure 4.20 summarizes the performance of the device as a function of the wavelength: the imbalance of the device is lower than 0.5 dB in the full C-Band, while the excess losses remain under 1.5 dB in the same wavelength range. Regarding the phase error and the CMRR, they are OIF compliant, as they are below 5° and -20 dB respectively.

4.5.5. Output Network design

4.5.5.1. Output Network layout design

Provided that the 90º hybrids have been implemented using a 2 × 4 MMI, an output network is required to properly combine the 2×4 MMI outputs, connecting them with the balanced photodiodes. The main restriction taken into account to design this network is that the four paths composing the network have to be as similar as possible, in order to ensure that the output network do not degrade the 2 × 4 imbalance.

Figure 4.21, shows the layout used for the output network, which is composed of bends, crossings and straight waveguides. A similar layout can be found in the literature, i.e. in [151]. As can be observed, all the paths contain the same number of elements, i.e. waveguide bends and crossings, being necessary to introduce dummy crossings (orange colored in figure 4.21). The degrees of freedom available to properly design this network, are the length of the straight waveguides, which have been dark-blue colored in figure 4.21, the radius of the bent waveguides, and the crossing angle. The bend radii and crossing are the same in the four paths in order to maintain the similarity. Hence, the only degree of freedom that allows to properly interconnect the MMIs and the photodiodes, while maintaining similar path lengths is the straight waveguide length.

4.5.5.2. Output Network elements design

All the elements employed in the output network have already been analyzed in section 4.5.3. Thus, in this section we will only justify the design values of the different

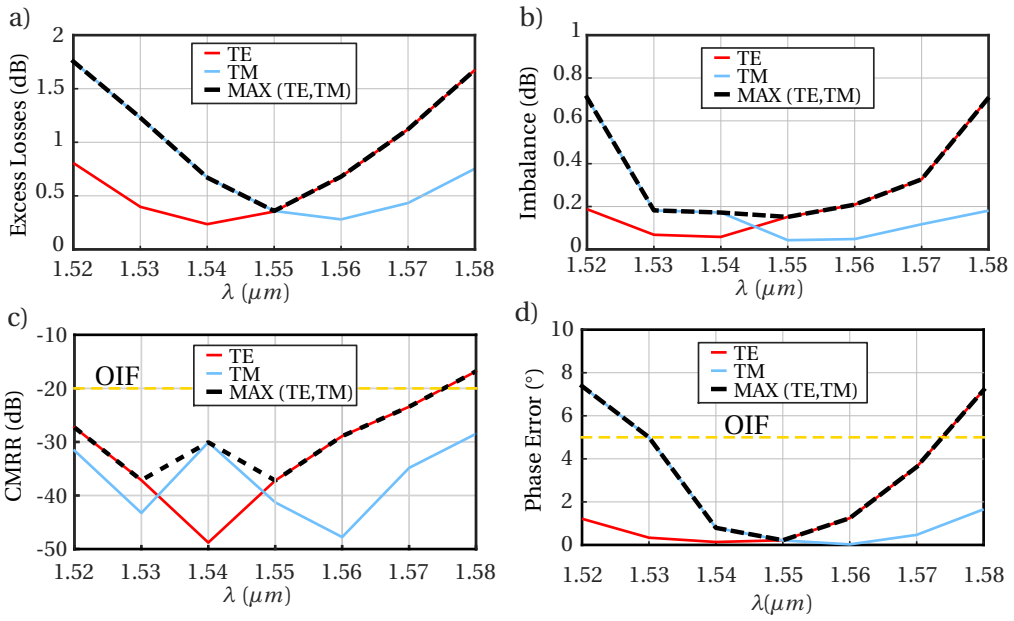

Figure 4.20.: a) b) c) and d) shows the excess losses (EL), the imbalance (IB), the CMRR and the phase error (PE) of the device for both polarizations, together with its maximum value (worst case). IB and EL are below 0.5 and 1.5 dB, respectively, in the C-Band. The CMRR -20 dB along C-Band and the phase error in the C-Band is around 5°, both of then complying the OIF recommendation.

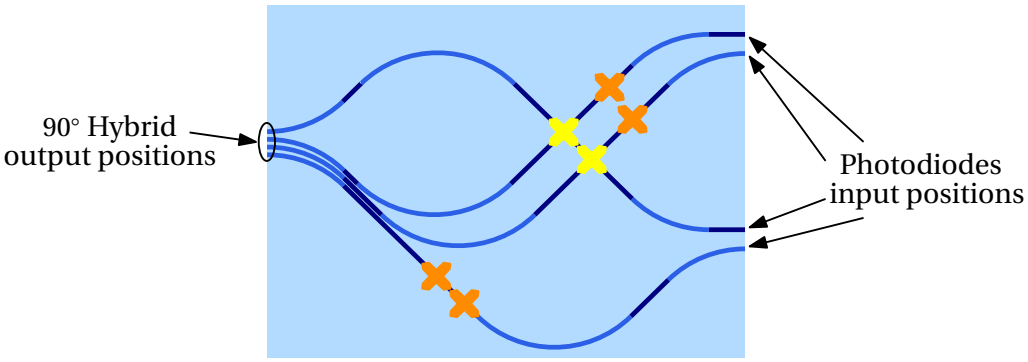

Figure 4.21.: Output network layout, in which the dummy crossings are orange colored. To properly design the network, the length of the dark-blue straight waveguides is judiciously chosen to maintain the length of the pads as similar as possible. The position the of each pair of balanced photodiodes is given by its building block, while the distance between them depends on the dimension of the building block.

elements: straight waveguides, crossings, bent waveguides and tapers.

Regarding the straight waveguides, the monomode width recommended in the design manual (2µm) is employed. The lengths of the different straight waveguides (dark-blue colored in figure 4.21) are carefully designed to maintain the total length of each path as similar as possible.

The radius of the waveguide bends is set to 250µm, to ensure low propagation losses. For this radius, the offset that minimizes the insertion losses and the second order mode excitation is 60nm, as shown in table 4.2.

For the waveguide crossings, the angle is set to 90º, which is the simplest solution and there is no need to employ smaller crossing angles.

Finally, as commented in section 4.5.3.6, all the tapers employed in the design are similar, so the same are used in this network.

4.5.6. PBS-Less receiver layout design

In the previous section, all the subsystems composing the receiver have been designed, and even some parts of the layout have already been proposed. In this section, the whole layout of the receiver is shown, and the guidelines followed during its design are described. It is worth mentioning that the layout generation was realized in a close collaboration with the Universidad de Zaragoza.

The design of the receiver layout consist of the distribution of the different subsystem that compose the receiver. These elements are the fiber to chip couplers, the polarization diversity network, the 2×4 MMIs, the output network, the photodiodes, and the electrical pads used for the photodiodes biasing and RF signal extraction.

The first elements to be placed are the photodiodes. They are placed at the end of the chip, and its position have to facilitate the routing of the electrical pads, that need to be placed next to the chip edge, as depicted in figure 4.22 a). As the available space was rather restricted, the separation between photodiodes is determined by the metal routing.

Once the position of the photodiodes is fixed, the output network and the 2×4 MMI positions are established, thus setting the layout of the IQ downconverter. The space between both IQ downconverters is also determined by the photodiodes positions. At this point, the layout of each IQ downconverter, and their relative positions are defined, so the output position of the polarization diversity network outputs is fixed, as shown in 4.22 b).

The next step is to place the polarization diversity network. However, a new constraint have to be satisfied: The separation between the fiber to chip couplers, which is 250µm, is fixed by the foundry, defining the input of the polarization diversity network, as depicted in 4.22 c). To properly place the polarization diversity network two degrees of freedom can be employed: the radius of the bend waveguide that is placed between the beam splitters and the fiber to chip couplers, and the absolute length of the birefringent waveguides (the differential length is chosen to meet the phase condition). The final layout is shown to scale in figure 4.22 d).

Even if the total purchased area is 3×6 mm^2, two different designs were allowed to be included in the layout submitted to the foundry. As the polarization diversity network is expected to be the most critical subsystem of the receiver in terms of sensi-

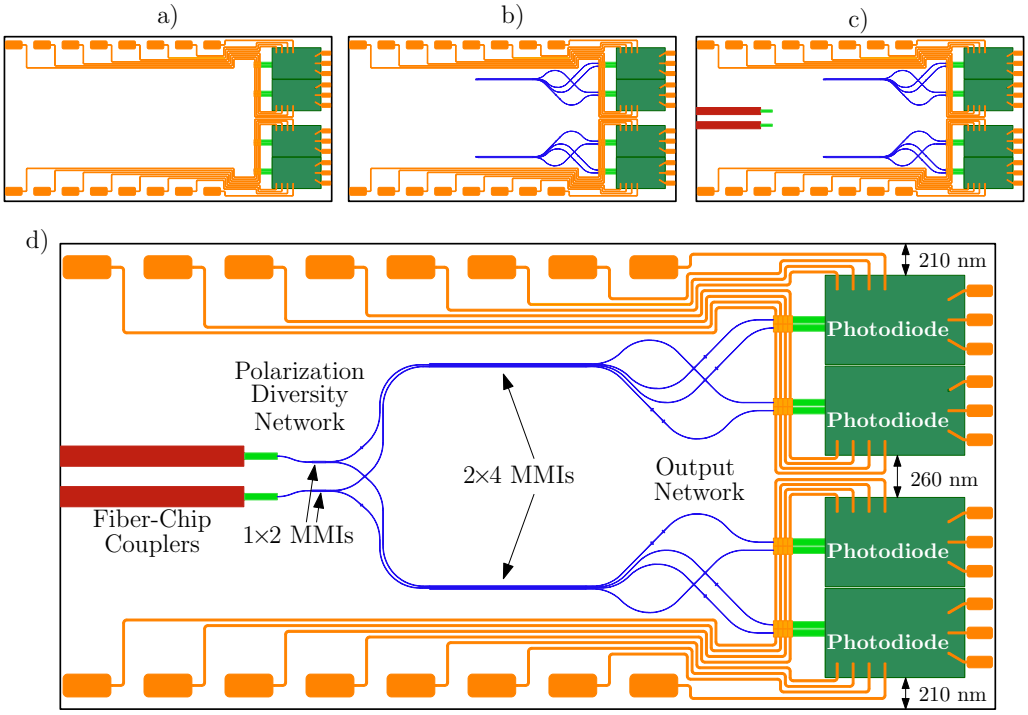

Figure 4.22.: a) Placement of the photodiodes together with the metal pads and routing. b) Placement of the output networks and the 2×4 MMIS. c) Placement of the Fiber to chip couplers. d) Layout of the PBSLess coherent receiver (scale 1:30, approx.).

tivity to fabrication tolerances, each design includes a different polarization diversity network design. Hence, the width of the polarization diversity network nominal waveguide is set to 2.3 and 2.5 μm in each design. This values are chosen because they are expected to properly work even considering maximum fabrication errors. The differential length of the birefringent waveguides is set to 166 and 127 μm, respectively. The following tables summarize the dimensions of the main elements included in the receiver.

		Pol. Div. Net.			Out. Net.
		Nominal	Design 1	Design 2	
Wg. Width (μm)		2.4	2.5	2.3	2
ΔL (μm)		147	166	127	-
Tapers (μm)		$W_{IN} = *$, $W_{OUT} = *$, L=40			
Curves	Radius (μm)	250			
	Offset (nm)	115	115	115	60
	Width (μm)	2.4	2.5	2.3	2
Crossing	Angle (°)	76	82	70	90
	Width (μm)	4	4	4	4

Table 4.3.: Dimensions of the main elements composing the polarization diversity network and the output network, respectively. * The input and output width depends on the waveguides they are adapting.

	MMI 1x2	MMI 2x4
Width (μm)	9.1	21.7
Length (μm)	86	982
Wg. Separation (μm)	1.5	1.5
Access. wg. width (μm)	3	5

Table 4.4.: MMI's dimensions summary

4.6. Preliminary fabrication results

The designed layout were sent to the foundry at the end of April 2015. Almost a year later the fabrication process finished, and a simple characterization of two samples was performed in the detectors group of HHI [170]. This characterization, evaluated the responsivity of the chip, ignoring the polarization response of the same.

To perform the characterization a tunable laser is coupled to one of the input ports, and the electric photocurrent generated in each photodiode is measured, as depicted in figure 4.23. Hence, the global responsivity of the receiver as a function of the wavelength is obtained. As the bandwidth of the receiver is limited by the 90º hybrids bandwidth, the measured response is essentially the wavelength response of the 90º hybrids, depicted in figure 4.24 a), except for an scaling factor that includes the insertion losses of the elements comprising the receiver. Taking into account these in-

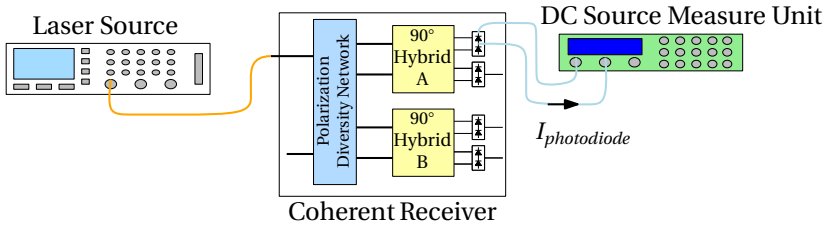

Figure 4.23.: Set-up used for the characterization of the receiver responsitivity.

sertion losses, shown in table 4.5 for the sake of clarity, and the responsivity of the photodiodes (0.9 A/W), the maximum responsitivity should be around 0.05 A/W. This estimation agrees with the maximum measured response from figure 4.24 b). However, the wavelength dependence of the responsitivity presents a different behavior, indicating that some issues may have happened during the fabrication process.

	Losses	# elements	Total Losses
Fiber to chip couplers	1,2 dB/device	1	1,2
E200-E1700 wg. transitions	0,14 dB/device	2	0,28
Waveguide tapers	0,1 dB/device	10	0
MMI 1x2 IL	3 dB/device	1	3
MMI 1x2 EL	0,15 dB/device	1	0,15
90 Bend waveguides	0,2 dB/device	4	0,8
Waveguide Prop. losses	2 dB/cm	0,25	0,5
Waveguides Crossings	0,11 dB/device	3	0,33
MMI 2x4 IL	6 dB/device	1	6
MMI 2x4 EL	0,3 dB/device	1	0,3

Table 4.5.: Insertion Losses of the different elements composing the receiver

From the measurements, it is clear that the 2×4 MMIs do not operate as expected. During the design process, a tolerance analysis of the 2×4 MMIs was performed in order to check that they behave properly at $\lambda = 1.55\mu m$, even considering the maximum deviations in the multimode region width (± 100 nm) which is the error source that have an stronger impact on the MMI operation. As the measured response is completely different from the expected in the worst case, bigger deviations in the multimode region width are considered. Figure 4.24 c) to e) shows for different errors in the multimode region width, the transmission S-parameters of the device. As can be observed in this figure, the MMI transmission response strongly depends on the multimode region width. Furthermore, if a deviation of -600 nm is considered, the simulated transmission S-parameters, are found in good agreement with the measured response.

The conclusion of this first characterization is that the errors in the waveguide width are around 600 nm, exceeding the 100 nm deviation that was specified in the design manual. Thus, the receiver is not expected to work. After some discussions with the foundry, it was agreed to realize a new fabrication run of the same receiver. At the time of writing this thesis, the second run was still under processing.

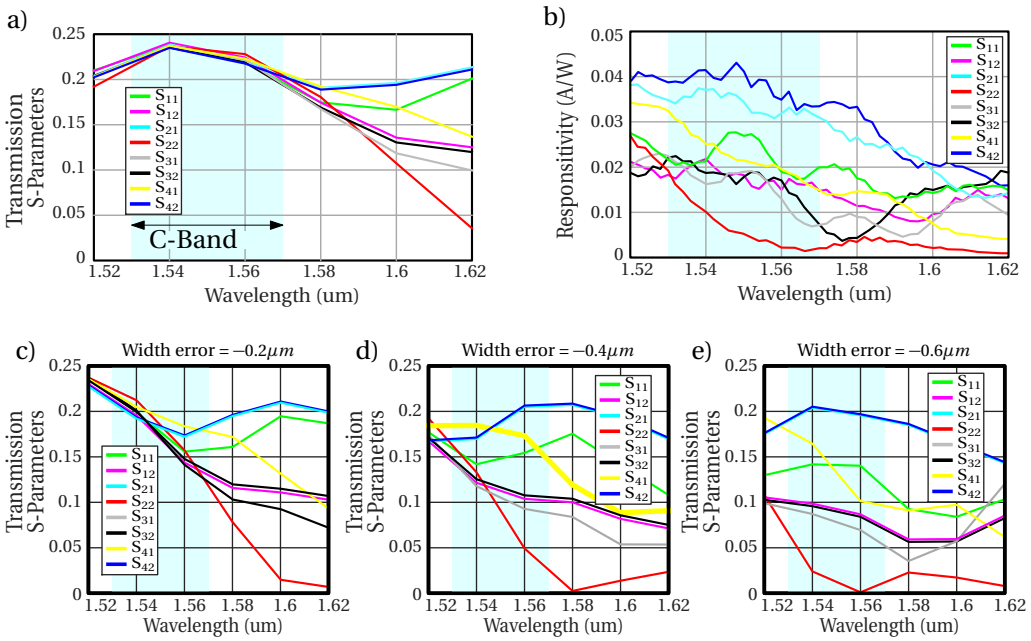

Figure 4.24.: a) Transmission S-parameters of the designed 2×4 MMI. b) Measured responsivity of the receiver. c-e) Transmission S-parameters of the designed 2×4 MMI for different multimode region width errors.

5

Leakage Losses in SWG waveguides

5.1. Introduction

Subwavelength gratings (SWG) are photonic periodic structures, with a period smaller than half the wavelength of the propagating field, so that diffraction effects are suppressed. Thus, a SWG behaves as a metamaterial whose optical properties, i.e. refractive index, dispersion and birefringence can be engineered. In contrast to other periodic structures, in SWGs light is neither radiated, as it occurs when diffraction effects are not suppressed, nor reflected, as happens when the grating periodicity is half the wavelength of the propagating field, i.e. the Bragg condition is met.

The first SWG application in integrated photonics were proposed at the beginning of the 90s, but the fabrication technology at that time made infeasible its implementation [22]. However, the recent improvements in lithographic processes have enabled a widespread implementation of SWG based devices, most of them in the Silicon-on-Insulator (SOI) platform [11, 171]. Designs based on the effective index engineering have enabled high performance fiber to chip couplers [24–26], sensitivity improvement in evanescent field sensors [172], low-loss waveguide crossings [173], ultra-compact optical true time delay lines [174] and fabrication tolerant mode multiplexers [175]. Alternatively, dispersion engineering have enabled the design of high bandwidth devices such as directional couplers [176], grating couplers [177], and ultra-broadband multimode interferometers [12]. Due to the inherent anisotropy of

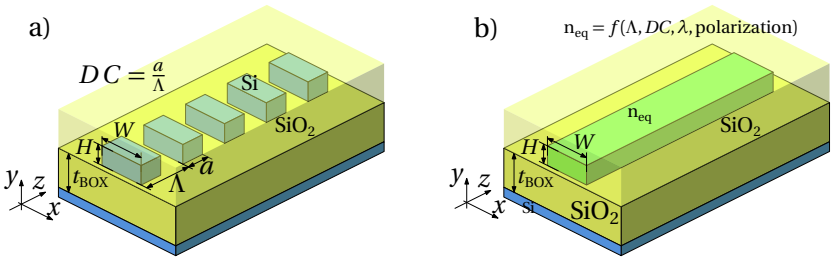

Figure 5.1.: a) SWG waveguide implemented in the SOI platform. The cladding material is SiO_2. b) Equivalent homogeneous waveguide.

the SWG, recents works have also taken advantage of the possibility of design the birefringence of the metamaterial implementing polarization managing devices such as polarization splitters [50] and polarizers [178].

Figure 5.1 a) shows a SWG waveguide implemented in the Silicon-On-Insulator platform. The geometry of this waveguide is defined by the grating pitch (Λ), the duty cycle (DC), the height (H) and the width (W). As can be observed, a SWG waveguide is the concatenation of periodically interlaced segments of two different materials, in this particular case Si and SiO_2.

In SWG waveguides light propagates in the form of Bloch-Floquet modes, that are confined by total internal reflection, as occurs with the modes of conventional waveguides. Thus, a SWG waveguide behaves as an homogeneous equivalent waveguide, as depicted in figure 5.1 b), whose equivalent refractive index, n_{eq}, depends on the geometry of the SWG waveguide together with the polarization and wavelength of operation. In most practical cases, n_{eq} is calculated using numerical calculations, but in the case the ratio Λ/λ is small enough, the equivalent refractive index can be calculated using the Rytov's formulas [11].

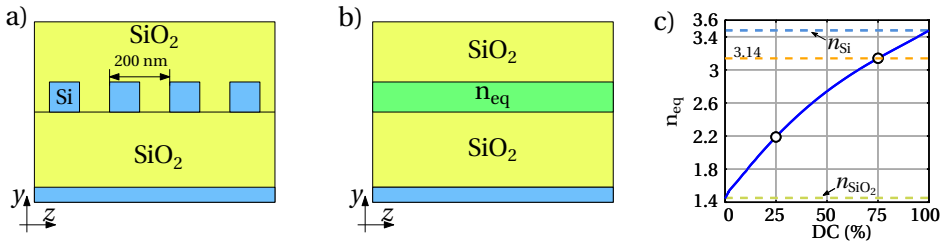

Figure 5.2.: a) 2D geometry of an infinitely wide SWG waveguide in SOI. b) 2D Equivalent homogeneous infinitely wide waveguide. c) Relation between the DC of the SWG waveguide amd the refractive index of the equivalent homogeneous waveguide, considering TE polarization at λ= 1550 nm and infinite waveguide width.

For the purpose of this work, the equivalent homogeneous waveguide is defined as the homogeneous waveguide with the same height and width and an equivalent effective index that makes the fundamental mode to have the same propagation constant than the Bloch-Floquet mode propagating along the SWG waveguide. As an example of the similarities between the SWG waveguide and the equivalent homogeneous waveguide behavior, the equivalent refractive index has been calculated as a function of the DC for a SWG waveguide with $H = 220\,\text{nm}$ and $\Lambda = 200\,\text{nm}$, in the SOI platform. For the sake of simplicity, the width of the waveguide is considered to be infinite, so that 2D simulations can be employed, considering the 2D geometry depicted in figures 5.2 a) and b). Figure 5.2 c) shows the equivalent refractive index as a function of DC, for TE polarization and $\lambda = 1.55\,\mu\text{m}$. It is shown that SWG waveguides with DC in the range 0-100% are modeled using homogeneous waveguides with core refractive indexes in the range 1.44 to 3.476. This is an intuitive result, as in the case of DC = 0% and DC =100%, the waveguide is no longer periodic, and the equivalent refractive indexes are the indexes of the waveguide material, i.e 1.44 (SiO_2) for DC=0 and 3.476 (Si) for DC=100%.

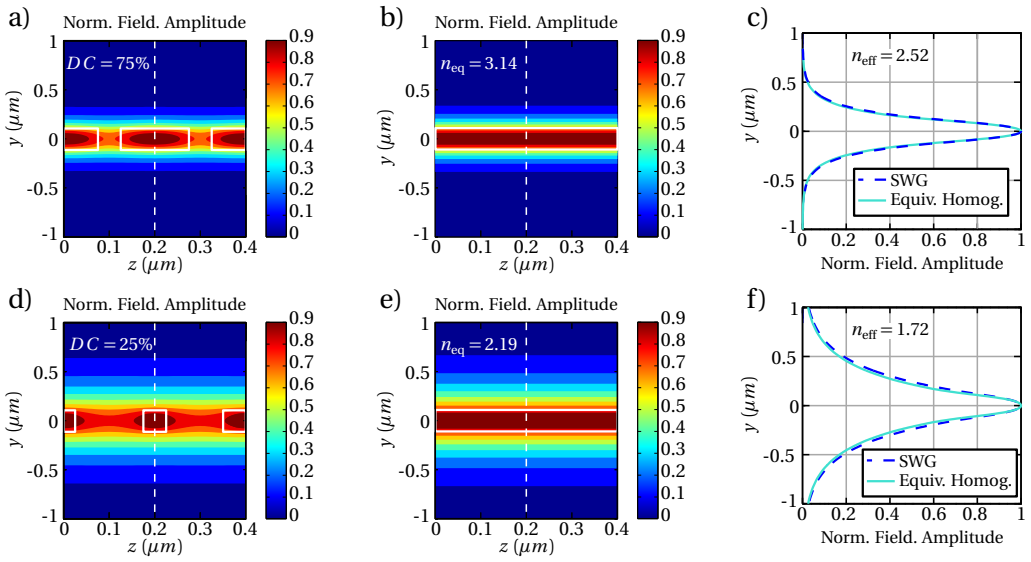

Figure 5.3.: a) Propagation in a SWG waveguide with DC=75 % and Λ=200 nm. b) Propagation in the homogeneous equivalent waveguide of a). c) Amplitude of the field in z=0.2 µm of figures a) and b). d) Propagation in a SWG waveguide with DC=25% and Λ=200 nm. e) Propagation in the homogeneous equivalent waveguide of d). f) Amplitude of the field in z=0.2 µm of figures d) and e). Similar field amplitudes are observed in c) and d) for the SWG waveguides and its corresponding equivalent homogeneous waveguides. Lower modal confinement is observed for lower DC.

In order to show that the homogeneous equivalent waveguide properly models the SWG waveguide, the field propagation on the waveguides depicted in 5.2 a) and b) are shown for two different values of DC, and consequently different values of n_{eq}, signaled in figure 5.1 c). Figure 5.3 a) shows the 2D propagation of the optical field in the SWG waveguide (DC = 75%), while 5.3 b) shows the propagation in the equivalent homogeneous waveguide, $n_{eq} = 3.14$. For these propagations, the fields at $z = 0.2$ µm are plotted in figure 5.3 c). The same modeling has been performed for a SWG waveguide with a DC of 25 % and an equivalent homogeneous waveguide with $n_{eq} = 2.19$, as shown in figures 5.3 d-f). In both cases, similar fields amplitudes along the y axis are observed, which indicates that the used definition of equivalent waveguide SWG not only properly models the modal effective index, but also the field profile. From figures 5.3 c) and f) it can be also observed that the smaller the DC, the more expanded is the optical field. Thus, as DC<100% in SWG waveguides, the modal confinement is always lower than the modal confinement of a silicon wire of the same height and width.

In silicon-on-insulator platform, the thickness of the buried-oxide (BOX) layer, t_{BOX} in figure 5.1 is chosen among other factors, to provide optical isolation between the waveguide core and the substrate. Usually 2-3 µm is enough to provide a large isolation, abstracting designers from the problem of leakage losses towards the substrate. However, when SWG devices are designed in silicon-on-insulator, the already estab-

lished buried oxide layer thickness may not be enough to fully isolate the optical field from the substrate, as the modal confinement diminishes. Thus, the leakage losses have to be checked in any SWG design, in order to prevent from inoperable devices or unexpected operation.

An example of unexpected operation in SWG based devices is found in [174, 179], where SWG waveguides are used to implement optical true time delay lines. Thus, different delays are implemented by tunning the DC of SWG waveguides. In those works, for low DC SWG waveguides, unexpected transmission losses are observed, which can be attributed to the leakage losses.

The rigorous simulation of leakage losses is non-trivial in conventional waveguides [180], becoming rather challenging for the Bloch-Floquet modes in SWG devices. It is well known that leakage losses are related to the modal confinement, increasing as the modal confinement diminishes. At the same time, the modal confinement is related with the mode effective index. From these relations, the possibility of establish a relation between effective index and leakage losses, can be considered. That relation, would avoid the explicit calculation of the leakage losses, thus expediting the design process of SWG devices.

In this chapter, an approach to estimate the leakage losses of SWG waveguides from the Bloch-Floquet mode effective indexes is provided. Thus, after describing techniques to adequately simulate periodic structures (sect. 5.2), a numerical demonstration of the relation between the effective index and leakage losses in SWG waveguides is provided (sect. 5.3). Finally, an experimental demonstration of this relation is provided (sect. 5.4) and some conclusions are drawn (sect. 5.5).

5.2. Simulation of periodic structures

This section aims to explain the simulation procedure that has been employed to numerically demonstrate the relation between effective index and leakage losses in SWG waveguide as the depicted in figure 5.1 a). If the reader is more interested in the relation itself, the reading of this section can be omitted.

5.2.1. 2D simulation of periodic structures

2D simulations are less computationally demanding than its 3D counterpart, due to the relatively reduced complexity. However, they require to transform the real 3D problem to an equivalent 2D problem by means of an approximate method such as the effective index method (EIM) [181]. Figure 5.4 a) shows the original 3D structure. For our purpose, the EIM method has been applied in the x-direction. It is worth mentioning that by applying this approximation, geometrical variations in the x-direction, such as the waveguide width, are translated into changes in the refractive index, n_{core}. In order to calculate n_{core} for the in-plane polarization, the 1D slab show in figure 5.4 b) is solved and n_{core}, used in the 2D approximation is the effective index of its fundamental TM mode. The final 2D periodic structure, is shown in figure 5.4 c).

Once the effective index method is applied, a complex Bloch-Floquet modal analysis is performed on the structure depicted in figure 5.4 c). In this work, simulations

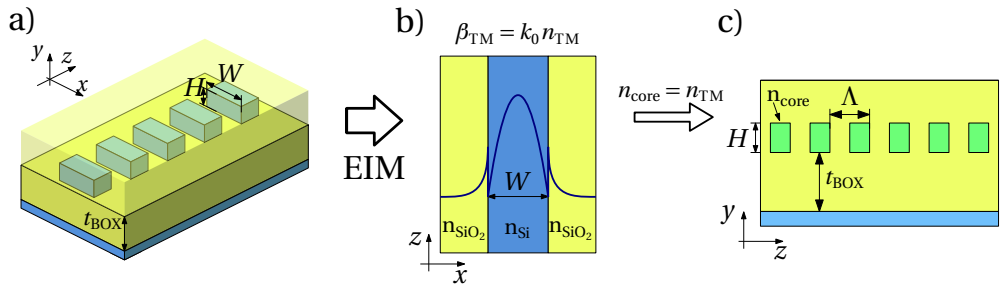

Figure 5.4.: a) Original 3D SWG waveguide. b)1D slab solved to calculate the refractive index of the silicon blocks n_{core} in the equivalent 2D structure. c) Equivalent 2D structure

are carried out with FEXEN, our in-house Fourier-type 2D vectorial simulation tool, which is highly efficient in the analysis of periodic structures [182]. The effective index of the Bloch-Floquet mode is directly obtained from the real part of the complex effective index, $n_{eff}^{BF} = \Re(\gamma_{eff}^{BF})$, while the leakage losses are calculated from the imaginary part of the complex effective index, $\Im(\gamma_{eff}^{BF})$, as follows:

$$L(\text{dB/cm}) = 10\log_{10}\left(\exp\left(\frac{2\pi\Im(\gamma_{eff}^{BF})}{\lambda(cm)}\right)\right) \tag{5.1}$$

As previously mentioned, 2D simulations have the advantages of being faster and lower computing demanding than 3D simulations. Nevertheless, as the 2D simulated structure is an approximation of the "real" 3D problem, the results obtained in 2D simulations differs from the results obtained using 3D simulations. Thus, 2D simulations can offer a valuable approximation, but there is a need to properly address the uncertainty of the solution.

5.2.2. 3D simulation of periodic structures

The 3D simulation of the leakage losses is more accurate than its 2D counterpart as no approximate methods are required. However, it has two drawbacks: on one hand the computation time increases dramatically as a more complex problem is solved; on other hand, different simulations are needed to calculate effective index and leakage losses. In the following subsections the techniques that have been used to simulate the effective index and the leakage losses in 3D simulators are detailed.

5.2.2.1. Real part of the Bloch-Floquet mode effective index calculation

There are several approaches to calculate the real part of the 3D Bloch-Floquet mode effective index, n_{eff}^{BF}. In this thesis, n_{eff}^{BF} has been calculated using 3D full vectorial FDTD simulations. For this purpose a single period of the SWG waveguide whose n_{eff}^{BF} will be characterized is simulated, as shown in figure 5.5 a). The applied boundary conditions are periodic in both $z = 0$ and $z = \Lambda$ planes, while in the rest of the boundaries perfect matched layers (PMLs) are used. To calculate n_{eff}^{BF}, resonant modes of the cavity with an arbitrary phase shift, ϕ, between the $z = 0$ and $z = \Lambda$ planes are sought.

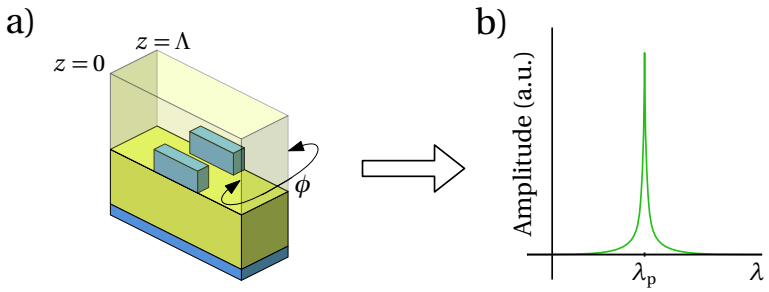

Figure 5.5.: a) Single SWG waveguide period used for the effective index calculation in a FDTD 3D solver. b) Fourier transform of the electric field recorded when the structure in a) is simulated.

The structure is excited with a short Gaussian input pulse. Then, the resonance wavelength (λ_p) of the structure is found through the Fourier Transform of the recorded electric field, as shown in figure 5.5 a) . At the resonance wavelength and for the imposed phase shift, ($n_{\text{eff}}^{\text{BF}}(\lambda_p)$) can be easily determined, as the period of the structure is known:

$$\begin{aligned} \phi = \beta L = \tfrac{2\pi}{\lambda_p} n_{\text{eff}}^{\text{BF}}(\lambda_p)\Lambda \\ n_{\text{eff}}^{\text{BF}}(\lambda_p) = \tfrac{\phi\lambda_p}{\Lambda 2\pi} \end{aligned} \tag{5.2}$$

As the resonant wavelength will depend on the imposed phase shift, this process has to be repeated several times (usually 3-4 iterations are enough), considering different phase shifts until the resonance wavelength coincides with the operation wavelength.

5.2.2.2. Leakage losses calculations

The calculation of leakage losses is not as straighforward as the calculation of the real part of the effective index. When then leakage losses are calculated using modal analysis, a complex solver is required thus increasing the required computing resources. Furthermore, as the substrate have to be included in these simulations, substrate modes can appear, difficulting the modal analysis of the waveguide leakage losses. Leakage losses can also be calculated using FDTD simulations, however, in order to measure leakage losses long structures are used, thus requiring a large amount of compunting resources and time. The techniques presented in this subsection, require either a huge computation time or a multiple step process to calculate the leakage losses of a SWG waveguide. Two different techniques to simulate the leakage losses are presented: The first one, makes use of 3D FDTD simulations, while the second one is based on the modal analysis of an equivalent homogeneous waveguide.

Calculation of leakage losses using 3D FDTD fully vectorial simulations

In the first mentioned technique, in order to calculate the leakage losses, two different 3D FDTD fully vectorial simulations are needed. First of all, a back-to-back

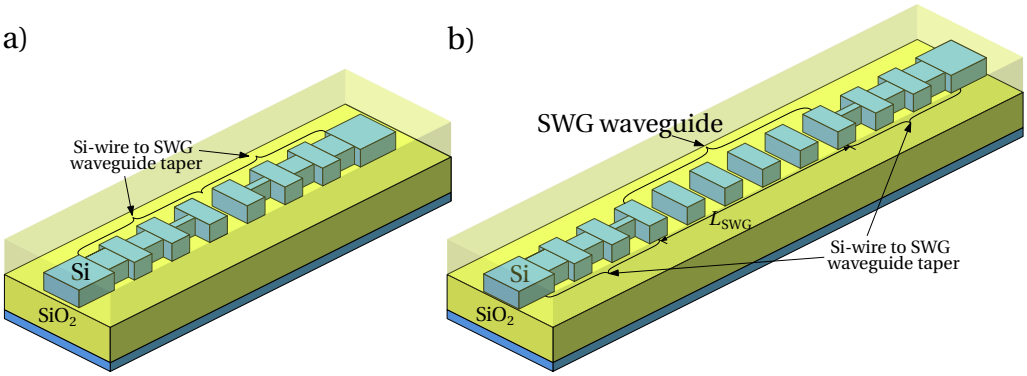

Figure 5.6.: a) Back-to-back structure of a Si-wire to SWG waveguide taper. b) The same that a), containing a SWG waveguide of L_{SWG}.

structure consisting of a Si-wire waveguide and a SWG taper, as depicted in figure 5.6 a), is simulated. This structure is excited with the fundamental mode of the Si-wire, and a power monitor is located on the substrate, measuring the amount of power that leaks towards the substrate. The second structure, adds a SWG of a certain length, L_{SWG}, to the first structure as depicted in figure 5.6 b). Then, the same simulation is performed, measuring the power leaked to the substrate. Thus, the losses attributed to the leakage of the SWG waveguide are the difference of the measured powers.

Calculation of leakage losses using 3D modal analysis

The second technique lays on the approximation of the SWG waveguide as an equivalent homogeneous medium, that was already presented in the introduction. By using this approximation, the leakage losses of a SWG waveguide, see figure 5.7 a) can be calculated from the modal analysis of its equivalent homogeneous waveguide, as depicted in figure 5.7 b). Using perfect matched layers as a boundary condition and a complex solver, the structure of 5.7 c) can be simulated, and the leakage losses can be calculated from the complex propagation constant, using equation 5.1.

The leakage losses calculated using both simulation techniques are similar. The FDTD simulations that have been used to calculate the leakage losses take around 6 hours per simulation, as a long structure is needed in order to measure small leak-

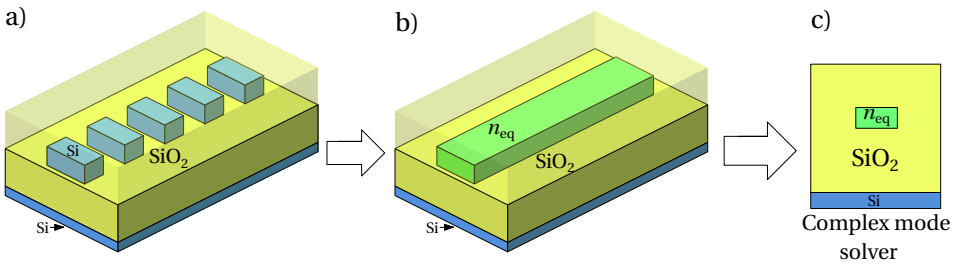

Figure 5.7.: SWG waveguide a), and its homogeneous equivalent waveguide b). c) Structure used to simulate the waveguide depicted in b).

age losses. On the other side, the simulations based on the equivalent homogeneous waveguide can take a few minutes, but require to previously calculate the equivalent refractive index. In the following, results coming from 3D simulations are based on this second technique, having been double checked some of them using the first technique.

5.3. Numerical Demonstration of the relation between effective index and leakage losses

As discussed in the previous section, the calculation of leakage losses in SWG devices is a tricky and time consuming task. On other side, the calculation of the real part of the Bloch-Floquet mode effective index (referred in the following as modal effective index), is further easy and quick. Thus, if we could estimate leakage losses from the modal effective index, the design of SWG devices would be expedited, avoiding the explicit calculation of the leakage losses.

In this section a numerical demonstration of the relation between effective index and leakage losses is provided. This demonstration is performed in the silicon-on-insulator platform, considering a waveguide height of 220 nm, two different BOX thicknesses of 2 and 3 µm, and a SiO_2 cladding of 700 nm. Furthermore, TE polarization and operation in the wavelength range from 1.5 µm to 1.6 µm are considered.

First of all, a SWG waveguide is simulated in both 2D and 3D simulators, and the results of these simulations are compared. In these simulations the DC is swept, while the rest of structural parameters are: waveguide width 400 nm, SWG pitch 200 nm and BOX thickness 2 µm. 2D and 3D simulations are performed as described in the previous section, with the 3D leakage losses calculation realized using the technique based on the modal analysis of the equivalent waveguide. The results of these simulations are shown in figure 5.8 a) and 5.8 b), where the leakage losses and the modal effective index are respectively represented as a function of the SWG duty cycle, for 3D and 2D simulations.

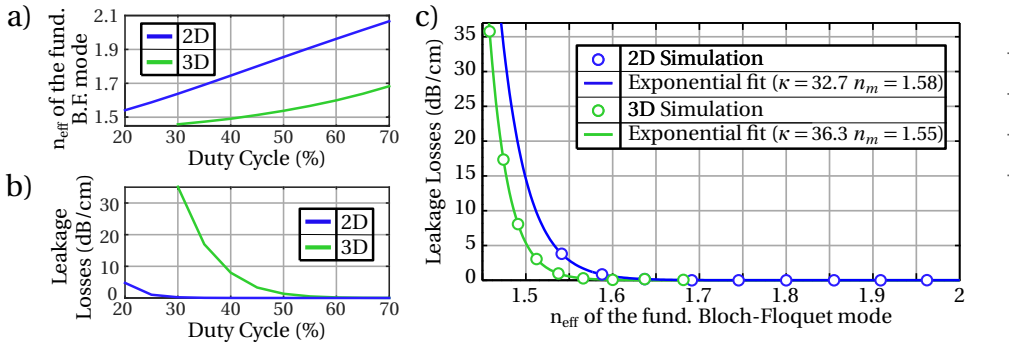

Figure 5.8.: a) and b) Effective index and leakage losses of the fundamental TE Bloch-Floquet mode as a function of the duty cycle, for 3D and 2D simulations. c) For 3D and 2D simulations, leakage losses vs. modal effective index.

Comparing the curves on figures 5.8 a) and b), the following observation can be

made:

- For the same DC, 2D simulations overestimate the modal effective index. The reason lying this effect is found on the application of the EIM method that assumes an infinite long waveguide, ignoring the dislocation of the electric field in the z-direction [172].
- Additionally, 2D simulations shows smaller leakage losses than 3D simulations. As leakage losses are related with the delocalization of field, and the higher the effective index, the lower the delocalization of the field, it is expectable that 2D simulations, yielding a high modal effective index, have a low leakage losses.

In summary, from figures 5.8 a) and b) it can be concluded that 2D simulations overestimate effective index and underestimate the leakage losses for a given SWG waveguide.

To show the dependence between modal effective index and leakage losses, they are plotted together in figure 5.8 c). This figure shows a clear relation between leakage losses and modal effective index in both 3D and 2D simulations. In this figure, the continuous curves are obtained by fitting the simulation points to an exponential curve defined as

$$\text{Loss (dB/cm)} = e^{-\kappa(n_{\text{eff}}-n_{\text{m}})}. \tag{5.3}$$

So far, an exponential relation between leakage losses and effective index is found in both 3D and 2D simulations. However, as shown in figure 5.8 c), the curve obtained using 2D simulations slightly differs from its 3D counterpart. From the comparison of these curves, it can be concluded that abstracting from the physical structure, for a given modal effective index the leakage losses calculated using 2D simulations are slightly higher. This provides an upper bound of the leakage losses, particularly in the region where the leakage losses are low (<1 dB/cm), which is the region of interest in most practical designs. Therefore, since the interest lies in the relation between effective index and leakage losses, this relation can be obtained using 2D simulations, as in a low-loss regime the rigorously calculated (3D) leakage losses can be estimated as the leakage losses of an equivalent 2D waveguide that yields the same effective index as the 3D waveguide.

At this point, the exponential relation between the modal effective index and the leakage losses can be deeply examined using 2D simulations. Thus, for two different values of the BOX thickness, different combinations of DC, Λ, equivalent core refractive index (n_{core}) and operating wavelength (λ) are considered. Figure 5.9 a) shows the calculated leakage losses as a function of the effective index of the fundamental Bloch-Floquet mode. The height of the waveguide is found to have a negligible impact, as shown in figure 5.9 b).

From this figure it can be concluded that for a constant BOX thickness, all the variations in the SWG structural parameters lead to a pair (n_{eff}, Leakage losses) that lay on a single exponential curve. Thus, according to these results, the leakage losses can be estimated from the modal effective index, being virtually independent on the specific SWG waveguide geometry, in the considered range of parameters.

As it would be useful for the comparison with the measurements, the same relation can be expresed as a function of the group index instead of the effective index,

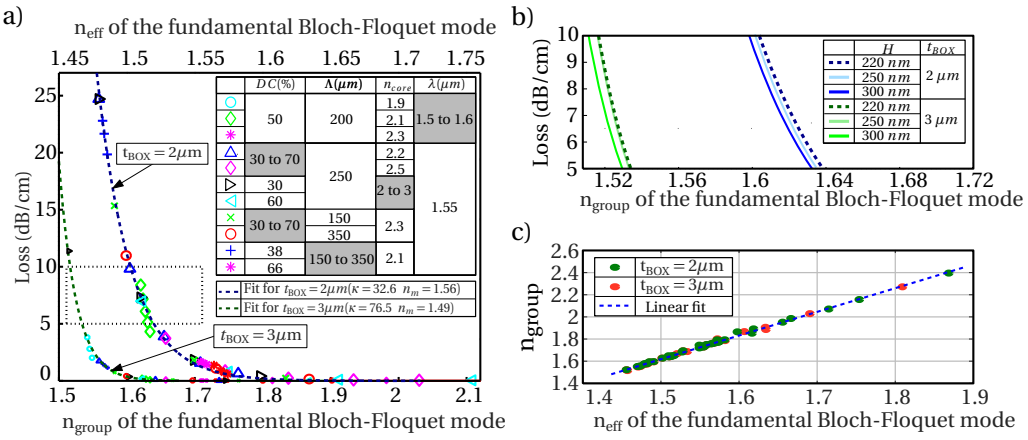

Figure 5.9.: a) Calculated leakage losses as a function of the effective index and the group index of the fundamental Bloch-Floquet mode. BOX thickness are 2µm and 3µm respectively, and waveguide height is 220 nm. Markers show calculated results for different SWG waveguide geometries, as summarized in the legend. Curves are exponential fits. In the legend of panel a, grey background indicates that the parameter has been swept. b) Detail of the dashed rectangle region of (a), adding the fits obtained from simulations similar to (a), with different waveguide heights. c) Relation between the calculated modal effective index and the group index.

provided the linear relation between effective index and group index, which is shown in figure 5.9 c). For the considered range of parameters, this linear relation obeys to $n_{\text{group}} \approx 2.14 n_{\text{eff}} - 1.6$.

5.4. Experimental demonstration of the relation between effective index and leakage losses

5.4.1. Test Structures

The simplest test structure to measure the group index and leakage losses of a SWG waveguide is a Mach-Zehnder Interferometer (MZI), in which one of the arms implements a Si-wire waveguide, while the other arm contains a SWG waveguide, as depicted in figure 5.10 a). As can be observed in the same figure, SWG tapers are used to provide a transition between the Si-wire interconnecting waveguides and the SWG waveguide. The length of these tapers is much smaller than the length of the SWG waveguide, so in the following analysis their impact on group index and leakage losses is ignored.

The transmittance spectrum of a MZI, which is qualitatively depicted 5.10 b), inherently provides information about the differential group index,

$$\Delta n_{\text{group}} = n_{\text{group}}^{\text{wire}} - n_{\text{group}}^{\text{SWG}}, \tag{5.4}$$

and the differential propagation losses,

$$\Delta\alpha = \left|\alpha^{\text{SWG}} - \alpha^{\text{wire}}\right| \tag{5.5}$$

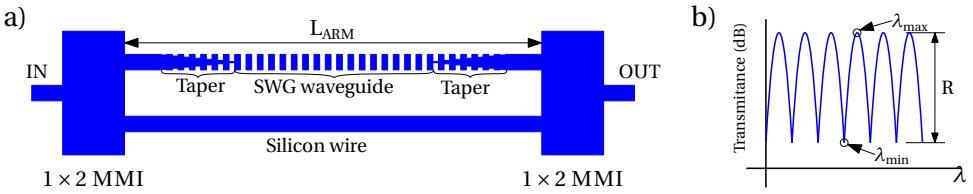

Figure 5.10.: a) Mach-Zehnder interferometer (MZI) used to indirectly measure the group index and the leakage losses of the SWG waveguide. b) Schematic interferogram of a MZI.

From the wavelengths corresponding to the minima and the maxima of the transmittance spectrum it is possible to obtain Δn_{group} as follows:

$$\Delta n_{\text{group}} = \frac{\lambda_{\text{max}}\lambda_{\text{min}}}{2L_{\text{arm}}(\lambda_{\text{max}} - \lambda_{\text{min}})}. \tag{5.6}$$

where L_{arm} is the length of both arms. Regarding the losses, they are calculated from the difference between the maximum and the minimum transmittance, R in figure 5.10 b), using the following expression:

$$\Delta\alpha = \frac{1}{L_{\text{arm}}[\text{cm}]}\left[20\log\left(\frac{10^{R/20}+1}{10^{R/20}-1}\right)\right] \quad [\text{dB/cm}], \tag{5.7}$$

the deduction of this expressions from the MZI systemic model can be found in appendix A.3.

The structural parameters of the designed SWG waveguides are shown in table 5.1, while the Si-wire, that is the same in all the MZIs, is 450 nm wide and 220 nm high. Both arms have the same length, which is $L_{\text{arm}} = 3$ mm, while the length of the SWG tapers is 30 µm.

SWG wg.	DC (%)	Λ (μm)	h (nm)	w (nm)
A	50	200	220	450
B	50	250	220	450
C	50	300	220	450
D	66	300	220	450

Table 5.1.: Structural parameters of the SWG waveguides included in the test structures.

5.4.2. Fabrication

The SWG waveguides together with the test structures were fabricated in the Silicon-on-Insulator platform offered at CEA-LETI. In this platform the silicon layer is 220 nm thick, and the BOX thickness is 2 µm. After the patterning of the structures, a 700 nm SiO_2 upper cladding is deposited by Plasma Enhanced Chemical Vapor Deposition (PECVD). To assure significant leakage losses, waveguides were slightly over-etched,

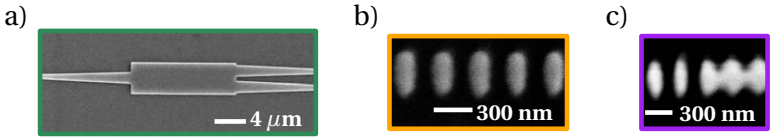

Figure 5.11.: SEM images of the fabricated structures. a) 1×2 MMI, b) SWG waveguide and c) SWG taper

thereby decreasing the duty-cycle and enhancing leakage to substrate. Figure 5.11 shows some of the patterned structures.

5.4.3. Measurements

The set-up used for the characterization of the SWG waveguides is shown in figures 5.12 and 5.13 a). Light is generated in a tunable laser and send to a polarization controller to properly set the polarization in order to optimise the coupling. Then, light is coupled to the chip using SMF-28 optical fiber. At the output of the chip, light is collected with an SMF-28 optical fiber and transmitted to a power meter.

For each test structure a wavelength sweep in the 1.5µm−1.6µm range with a wavelength step of 25 pm is performed, recording the measured power in each wavelength step. These measurements are then processed using Matlab.

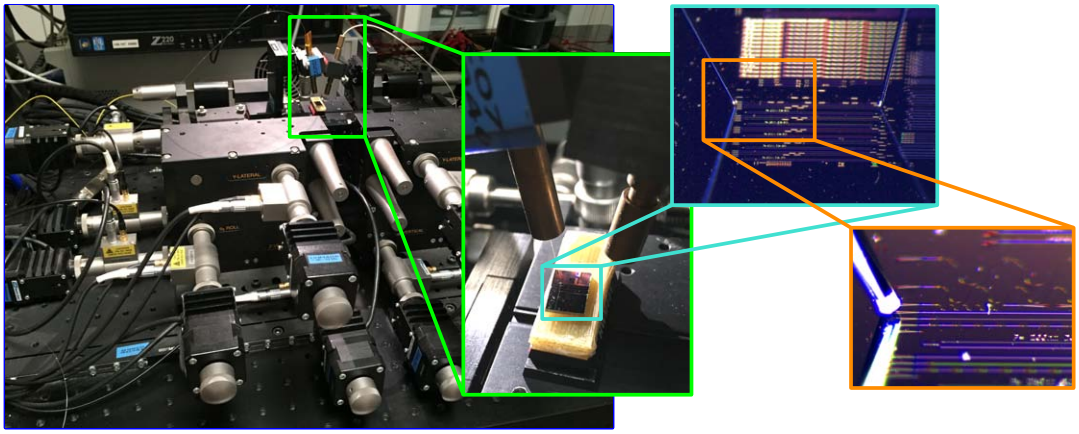

Figure 5.12.: a) Images of the measurement set-up and the photonic chip

The processing is rather simple: First of all, the wavelength response of the structures composed by a waveguide and the grating couplers is subtracted from the MZIs wavelength response. The second step is to find the wavelength position and the value of the interferogram local maxima and minima. Using this data together with the length of the arms ($L_{\text{arm}} = 3\,\text{mm}$), equations 5.6 and 5.7 can be properly evaluated.

So far, the differential group index and the differential losses have been obtained. However, our interest is to determine the group index and the leakage losses of the SWG waveguides, so the group index and the losses of the Si-wire have to be estimated. Regarding the group index of the Si-wire, it can be estimated using a 3D mode solver, in this case Fimmwave. It has been found to be nearly constant within the

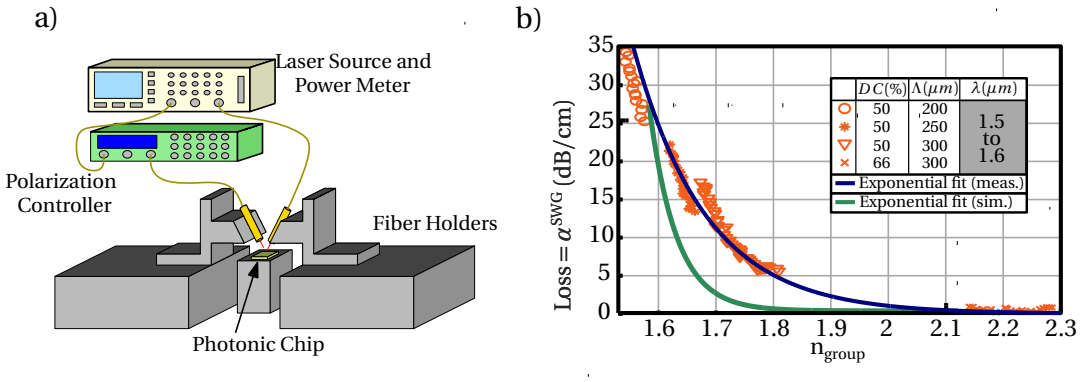

Figure 5.13.: a) Schematic draw of the measurement set-up. b) Measured leakage losses as a function of the measured group index, together with the exponential fit obtained from simulations.

considered wavelength range, $n_{group}^{wire} \sim 4.2$. Assuming that the waveguide tapers do not alter the group index measurement as they are much smaller than the SWG waveguide, the SWG waveguide group index can be determined from equation 5.4. Regarding the leakage losses, it can be assumed that the losses of the Si-wire are negligible, so the differential losses would have two main sources: the SWG leakage losses and the losses due to radiation in the SWG waveguide tapers, that were forgotten to be included in the lower arm. Thus the expression of the differential losses obeys to:

$$\Delta\alpha = \left|\alpha^{wire} - \alpha^{SWG}\right| = \alpha_{leak}^{SWG} + \alpha^{tapers}, \tag{5.8}$$

where the radiation losses in SWG tapers is estimated to be around 0.7 dB per taper.

Figure 5.13 b) shows the leakage losses as a function of the group index, for the characterized SWG waveguides. As was predicted in the previous simulations, there is an exponential relation between the leakage losses and the effective index, which is invariant on the SWG waveguide structural parameters. Furthermore, good agreement between simulations and measurement is found within the experimental accuracy, with a difference in the group index of 0.13 for a leakage losses of 5 dB.

5.5. Conclusion

In this chapter it has been demonstrated theoretically and experimentally that leakage losses in SWG waveguides are related with the modal effective index, independently of the structural parameters defining the SWG waveguide. By using this relation, designers can readily estimate the leakage losses from the calculated Bloch-Floquet effective index as follows:

1. For a given waveguide geometry, obtain the real part of the Bloch-Floquet mode effective index using a 3D simulator, wich can be calculated for instance, using the technique shown in section 5.2.2.1.

2. Using the computed effective index, the losses can be obtained from the exponential relation shown in figure 5.9.

Additionally, from figure 5.9, some practical conclusions, easing the design process of SWG devices can be formulated: For a 2-µm-thick BOX, leakage losses are negligible for a modal effective index higher than 1.65, while for a 3-µm-thick BOX virtually lossless operation is achieved for a modal effective index higher than 1.55.

Finally, if there is no chance to accurately calculate the effective index, i.e. only using 2D simulators, the modal effective index calculated using 2D simulators can be mapped to a 3D modal effective index comparing the curves on figure 5.8 a). Then, the leakage losses can be estimated as explained.

6
Conclusions and prospect

Three were the topic of this thesis: the design and implementation of an integrated fabrication tolerant polarization controller, the design and implementation of a dual polarization coherent receiver, and the exploration of the leakage losses in SWG devices. In this chapter, in the first section an overview of the achievements and contributions in these different topics is provided. The second section is devoted to briefly describe minor projects, i.e. collaborations in different tasks in the research group, that have been carried out during the PhD. Finally, in the third section the prospects of this thesis are reviewed.

6.1. Conclusions

6.1.1. Fabrication tolerant integrated polarization controller

The integrated implementation of polarization managing devices is challenging, mostly due to the high sensitivity to fabrication tolerances of such devices. Among the different proposed approaches, a trade-off between integrability and performance can be observed. One of the goals of this thesis was the implementation of a polarization controller that overcomes the trade-off between integrability and performance, while trying to relax the fabrication tolerances.

For this purpose, an integrated polarization controller scheme, inspired by the manual fiber polarization controller, has been proposed. The scheme only contains rotator waveguide sections and tunable polarization phase shifters (TPPS) both elements being well integrable. Furthermore, the scheme performances are maintained even when the rotator waveguide sections suffers from fabrication deviations. For this purpose, a tolerance condition has been demonstrated. This condition is technology independent and can be expresed in terms of the rotator waveguide extinction ratio.

In order to demostrate the device operation, a prototype has been designed, fabricated and characterized in the SOI platform using SU-8 as a cladding material. The TPPS are implemented exploiting the thermal properties of the materials in the platform, and the birefringence of the waveguide. The rotator waveguide sections are implemented using the approach proposed in [88]. Together with the polarization controller scheme, test structures were included, in order to evaluate the tolerance condition. The polarization controller was characterized, demonstrating a 40 dB polarization extinction ratio range. Furthermore, as the isolated rotator waveguide sec-

tion met the tolerance condition along the C-Band, the device operation has been demonstrated in the whole C-Band. Finally, several experiments were done demonstrating a degree of coverage of the Poincaré sphere of 98%.

6.1.2. Monolithically integrated dual polarization coherent receiver

A dual polarization coherent receiver retrieves information carried in the polarization, phase and amplitude of the optical field, enabling transmisions at high data rates. In a dual polarization coherent receiver, a polarization diversity network is used to separate the information carried in the orthogonal polarizations. However, the stringent fabrication tolerances of the polarization managing devices hinders the monolithic integration of the whole receiver, sacrifying compactness, reliability and cost. Thus, most of the current approaches implement the polarization diversity network in bulk optics, as the OIF recommends in its implementation agreement. In this thesis, one of the goals was the design and characterization of a dual polarization coherent receiver that avoids the use of polarization managing devices [21]. The receiver has been designed in the InP photonic platform offered by HHI. The polarization diversity network of the receiver is based on birefringent waveguides, that have been carefully designed in order to provided the maximum birefrigence while ensuring monomode operation and the best fabrication tolerances. The downconverters have been designed to operate with both polarizations, being OIF compliant. Once the receiver was fabricated, a responsitivity characterization was realized, obtaining unexpected results, as the measured responsitivity was far from the simulated one. From this characterization it was concluded that fabrication deviations were higher than specified, so at the moment of writing this manuscript, the second run of the receiver is being fabricated.

6.1.3. Leakage losses in SWG waveguides

SWG based devices have enabled a new degree of freedom in the design of integrated photonics devices. One of the goals of this thesis was the analysis of the leakage losses in integrated platforms when SWG devices are implemented. The goal of the analysis was to demonstrate that leakage losses are related with the modal effective index (and/or group index) of the field propagating along the SWG waveguide. To realize this analysis, a set of SWG waveguides have been fabricated in SOI, characterizing its group index and its leakage losses. Simultaneously, a numerical analysis has been performed in order to find the relation between effective index and leakage losses. Finally, it was demonstrated that for a given BOX thickness, the leakage losses of a SWG waveguide can be estimated from the mode effective index, independently of the structural parameters defining the SWG waveguide. From this relation, several techniques have been proposed in order to easily estimate the leakage losses of SWG waveguides from its modal effective index.

6.2. Other contributions

Appart from the contributions presented in this thesis, while in the PhD programme, the PhD student has been involved in several research lines, related with the topics included in this thesis. The two first contributions are the result of a 3 months stay at Ghent University, while the last one was at Málaga university.

Implementation of polarization rotator in the mid infrared band One of the goals of the stay was the design of polarization rotators at the mid-infrared band. This contribution included the analysis of the photonic platform, which was a pilot line at that time, the design of polarization rotators based on the approaches described in sections 2.4.2 and 2.4.4, and the generation of the layout for the fabrication of the device. At the time of writting this thesis the devices are being fabricated.

Characterization of a SOI coherent receiver for radio-over-fiber applications The second goal during the stay was the characterization of a SOI coherent receiver for radio over fiber applications. The results of this work are quite promising, as we demonstrated that SOI coherent receivers can be used in radio-over-fiber applications, improving the performances of the current schemes, that are based on IM-DD.

Study of the anisotropy in SWG structures SWG periodic waeguides are inherently anisotropic. This anisotropy has been demonstrated to be useful in order to improve the performance of devices such as the 2x2 MMI demonstrated in [12]. During the PhD programme, the student contributed to the analysis of the SWG waveguides anisotropy, that was included in [12].

6.3. Prospects

6.3.1. Improvement of the polarization controller performances

In this work we aimed at demonstration of the operation of the polarization controller, mainly demonstrating that polarization states in a large range of polarization extinction ratio are achieved. However, others parameters such as the bandwidth or the power consumption of the device have not been optimised. Once the operation has been demonstrated, in the short term, these performances can be addressed. For instance, the use of SWG waveguides to implement the TPPS could be explored.

6.3.2. Implementation of a PolSK transmitter

Communications systems based in polarization shift keying (PolSK) have been proposed for middle distance communication, offering better performances than IM-DD systems, while maintining low complexity. A PolSK modulator using the proposed polarization controller scheme could be implemented. To do so, it will be desirable to replace the thermal tunable polarization phase shifters with a faster alternative, such as PIN junction based modulators. The resulting device will provide an integrable

PolSK transmiter, with large fabrication tolerances, which will be very useful for massive fabrication of the same.

6.3.3. Characterization of monolithically integrated dual polarization coherent receiver

The coherent receiver has been unsuccessfully fabricated, so in the short term, the natural prospect on this goal is the characterization of the new dual polarization coherent receiver. If the responsivity of the new receivers is in good aggreement with the calculated one, the next step would be to realize the coherent characterization of the receiver. Once the coherent operation is demonstrated, the last step would be to demonstrate the operation of the polarization diversity.

6.3.4. Generalization of the leakage losses/effective index relation

The demonstrated relation between effective index and leakage losses has found a good acceptance in the research community. Given that interest, it would result useful in the medium term to derive a more general expresion, that could ease the design of SWG devices in different photonics platforms.

A
Appendices

A.1. Notation

In this thesis it has been used the following notation referring to the complex amplitude of the electrical field:

$$\begin{aligned} S(t) &= \mathrm{Re}\left\{Se^{j\omega_0 t}\right\} \text{ where} \quad S = \sqrt{P_S}e^{j\theta_S} = I + jQ = \left(\bar{I} + j\bar{Q}\right) \\ \mathbf{S}(t) &= \mathrm{Re}\left\{\mathbf{S}e^{j\omega_0 t}\right\} \; where \quad \mathbf{S} = \begin{bmatrix} S_x \\ S_y \end{bmatrix} \Rightarrow \begin{cases} S_x = \sqrt{P_{S_x}}e^{j\theta_{S_x}} \\ S_y = \sqrt{P_{S_y}}e^{j\theta_{S_y}} \end{cases} \end{aligned} \tag{A.1}$$

For example, in the coherente communications system, the received and the transmitted signals are:

$$\mathbf{S_{tx}} = \begin{bmatrix} S_x^{tx} \\ S_y^{tx} \end{bmatrix} \quad \mathbf{S_{rx}} = \begin{bmatrix} S_x^{rx} \\ S_y^{rx} \end{bmatrix} \Rightarrow \begin{cases} S_x^{rx} = \sqrt{P_{S_x^{rx}}}e^{j\theta_{S_x^{rx}}} = \sqrt{P_{S_x^{rx}}}\left(\bar{I}_x^{rx} + j\bar{Q}_x^{rx}\right) \\ S_y^{rx} = \sqrt{P_{S_y^{rx}}}e^{j\theta_{S_y^{rx}}} = \sqrt{P_{S_y^{rx}}}\left(\bar{I}_y^{rx} + j\bar{Q}_y^{rx}\right) \end{cases} \tag{A.2}$$

In a single polarization IQ downconverter, the input signal are S and OL. In a dual polarization down converter the inputs will be **S** and **OL**, as dual polarization signals are represented using a vector.

A.2. Derivation of the tolerance condition

In this section, the tolerance condition of a rotator waveguide section (RWS) needed to implement a polarization controller is presented. First of all some conclusions are extracted from the Jones matrix of a RWS. Then, the tolerance conditions of the RWS are derived for two differente cases: for polarization controllers containing two or three RWSs.

Let it consider an arbitrary polarization state with normalized power, describe by its Jones Vector:

$$\mathbf{E}(a,\rho) = \begin{bmatrix} ae^{j\rho} \\ \sqrt{1-a^2} \end{bmatrix}. \tag{A.3}$$

For the sake of clarity, the Jones matrix of a RWS, as a function of its optical axis tilt, θ and its phase shift, $\Delta\rho$, reproduced here:

$$\overline{\overline{J_R}}(\theta,\Delta\rho)=\begin{bmatrix} e^{j\Delta\rho}\cos^2\theta+\sin^2\theta & je^{j\varphi/2}\sin\Delta\rho/2\sin2\theta \\ je^{j\Delta\rho/2}\sin\Delta\rho/2\sin2\theta & \cos\theta+e^{j\Delta\rho}\sin^2\theta \end{bmatrix}, \tag{A.4}$$

and let also consider the square modulus of this matrix, as it will be useful later:

$$\left|\overline{\overline{J_R}}(\theta,\Delta\rho)\right|^2=\begin{bmatrix} |J_{11}|^2 & |J_{12}|^2 \\ |J_{21}|^2 & |J_{22}|^2 \end{bmatrix}, \tag{A.5}$$

after some algebra, and using trigonometric equivalences it can be expresed as

$$\left|\overline{\overline{J_R}}(\theta,\Delta\rho)\right|^2=\begin{bmatrix} (1-\mathrm{PCE})\mathrm{PCE} & \mathrm{PCE} \\ \mathrm{PCE} & (1-\mathrm{PCE})\mathrm{PCE} \end{bmatrix} \tag{A.6}$$

where the PCE is defined as:

$$\mathrm{PCE}=\sin^2(2\theta)\sin^2(\phi/2). \tag{A.7}$$

Let's now consider an arbitrary input polarization state at the input of the rotator, $\mathbf{E_{IN}}$. The output Jones Vector is given by:

$$\mathbf{E_{OUT}}=\overline{\overline{J_R}}(\theta,\Delta\rho)\mathbf{E_{IN}}(a_{\mathrm{IN}},\rho_{\mathrm{IN}}). \tag{A.8}$$

The power in each of the output components is given by:

$$|\mathbf{E_{OUT}}|^2=\begin{bmatrix} |A_{\mathrm{H}}|^2 \\ |A_{\mathrm{V}}|^2 \end{bmatrix}=\begin{bmatrix} P_{\mathrm{H}} \\ P_{\mathrm{V}} \end{bmatrix}=$$

$$\begin{bmatrix} a_{\mathrm{IN}}^2(1-\mathrm{PCE})+\mathrm{PCE}(1-a_{\mathrm{IN}}^2)-2\sqrt{(1-a_{\mathrm{IN}}^2)a_{\mathrm{IN}}^2\mathrm{PCE}(1-\mathrm{PCE})}\sin(\rho_{\mathrm{IN}}+f(\theta,\Delta\rho)) \\ a_{\mathrm{IN}}^2\mathrm{PCE}+(1-a_{\mathrm{IN}}^2)(1-\mathrm{PCE})+2\sqrt{(1-a_{\mathrm{IN}}^2)a_{\mathrm{IN}}^2\mathrm{PCE}(1-\mathrm{PCE})}\sin(\rho_{\mathrm{IN}}+f(\theta,\Delta\rho)) \end{bmatrix} \tag{A.9}$$

From this equation, the following conclusion can be made: The power in both components, will depend on the RWS parameters and the input SOP. However, the maximum and the minimum achievable power in each component will only depend on a_{IN}^2, which defines the polarization ratio, and θ and $\Delta\rho$, which are the parameters definning the RWS. Using this conclusion, the maximum and minimum powers in the vertical and horizontal components at the output of a rotator waveguide section can be rewriten as:

$$P_{\mathrm{OUT,max}}^{H}=\left(\sqrt{a_{\mathrm{IN}}^2(1-\mathrm{PCE})}+\sqrt{(1-a_{\mathrm{IN}}^2)PCE}\right)^2 \tag{A.10}$$

$$P_{\mathrm{OUT,min}}^{H}=\left(\sqrt{a_{\mathrm{IN}}^2(1-\mathrm{PCE})}-\sqrt{(1-a_{\mathrm{IN}}^2)PCE}\right)^2 \tag{A.11}$$

$$P_{\mathrm{OUT,max}}^{V}=\left(\sqrt{a_{\mathrm{IN}}^2\mathrm{PCE}}+\sqrt{(1-a_{\mathrm{IN}}^2)(1-\mathrm{PCE})}\right)^2 \tag{A.12}$$

$$P_{\mathrm{OUT,min}}^{V}=\left(\sqrt{a_{\mathrm{IN}}^2\mathrm{PCE}}-\sqrt{(1-a_{\mathrm{IN}}^2)(1-\mathrm{PCE})}\right)^2 \tag{A.13}$$

A.2.1. Tolerance condition for polarization controllers containing two RWSs

In this demonstration, for the sake of clarity we will consider that the input polarization state is horizontal, and we aim to generate arbitrary polarization states.

Assuming horizontal polarization at the input of the controller, and that the first TPPS does not change these amplitudes, the amplitude at the input of the second rotator can be calculated as:

$$\left|\mathbf{E_{IN,RWS}}2\right| = \left|\overline{\overline{J_R}}(\theta_{RWS1}, \Delta\rho_{RWS1}) \begin{bmatrix} 1 \\ 0 \end{bmatrix}\right| = \\ = \begin{bmatrix} \sqrt{1-\mathrm{PCE_{RWS1}}} \\ \sqrt{\mathrm{PCE_{RWS1}}} \end{bmatrix}. \tag{A.14}$$

In order to obtain the tolerance condition, we will impose that at the output of the second rotator, polarization states with arbitrary PER can be achieved (the last TPPS will provide the desired phase). This imposition is similar to impose that at the output of the second RWS the power in the vertical component is in the range [0,1], or similarly that at the output:

$$P^V_{\mathrm{OUT,RWS2,max}} = \left(\sqrt{a^2_{\mathrm{IN,RWS2}}\mathrm{PCE_{RWS2}}} + \sqrt{(1-a^2_{\mathrm{IN,RWS2}})(1-\mathrm{PCE_{RWS2}})}\right)^2 = 1. \\ P^V_{\mathrm{OUT,RWS2,min}} = \left(\sqrt{a^2_{\mathrm{IN,RWS2}}\mathrm{PCE_{RWS2}}} - \sqrt{(1-a^2_{\mathrm{IN,RWS2}})(1-\mathrm{PCE_{RWS2}})}\right)^2 = 0. \tag{A.15}$$

Asuming that $a_{\mathrm{IN,RWS2}} = \sqrt{1-\mathrm{PCE_{RWS1}}}$, and that $\mathrm{PCE_{RWS1}} = \mathrm{PCE_{RWS2}}$, after some algebra the tolerance condition is obtained:

$$\mathrm{PCE} = 1/2, \tag{A.16}$$

so, in a polarization controller containing only two RWS, as the depicted in figure 3.3 b), full polarization control is only achieved if the PCE of the RWS matches this condition.

A.2.2. Tolerance condition for polarization controllers containing three RWSs

In this case, the scheme contains an extra pair of TPPS-RWS. Again, we will consider that the input polarization state is horizontal, and we aim to generate arbitrary polarization states.

To perform this demonstration, we will impose that at the output of the last polarization rotator the power in the vertical component is in the range [0,1], and then last TPPS will provide the required polarization phase. The values of $a^2_{\mathrm{IN,RWS3}}$, in order to have$P^V_{\mathrm{OUT,RWS3,max}} = 1$ and $P^V_{\mathrm{OUT,RWS3,min}} = 0$, are calculated from equations A.12 and A.13, obtaining

$$a^2_{\mathrm{IN,RWS3,max}} = \mathrm{PCE}_{\mathrm{RWS3}} \text{ and} \tag{A.17}$$

$$a^2_{\mathrm{IN,RWS3,min}} = 1 - \mathrm{PCE}_{\mathrm{RWS3}} \tag{A.18}$$

for power in the vertical polarization of 0 and 1 respectively, note that intermediate values of $a^2_{\mathrm{IN,RWS3}}$ can be obtained by changing the polarization phase in TPPS1 and TPPS2.

At this point, considering horizontal polarization at the input of the polarization controller, the maximum and minimum achievable values of $P^V_{\mathrm{OUT,RWS2,max}}$ are calculated as a function of $\mathrm{PCE}_{\mathrm{RWS1}}$ and $\mathrm{PCE}_{\mathrm{RWS2}}$, being:

$$P^V_{\mathrm{OUT,RWS2,max}} = \left(\sqrt{(1-\mathrm{PCE}_{\mathrm{RWS1}})\mathrm{PCE}_{\mathrm{RWS2}}} + \sqrt{\mathrm{PCE}_{\mathrm{RWS1}}(1-\mathrm{PCE}_{\mathrm{RWS2}})}\right)^2 \tag{A.19}$$

$$P^V_{\mathrm{OUT,RWS2,min}} = \left(\sqrt{(1-\mathrm{PCE}_{\mathrm{RWS1}})\mathrm{PCE}_{\mathrm{RWS2}}} - \sqrt{\mathrm{PCE}_{\mathrm{RWS1}}(1-\mathrm{PCE}_{\mathrm{RWS2}})}\right)^2 \tag{A.20}$$

As the second TTPS will not change the amplitude of the polarization components, we will impose that the required $a^2_{\mathrm{IN,RWS3,V1}}$ and $a^2_{\mathrm{IN,RWS3,V2}}$ are in the range $[P^V_{\mathrm{OUT,RWS2,max}}, P^V_{\mathrm{OUT,RWS2,min}}]$ as follows:

$$P^V_{\mathrm{OUT,RWS2,min}} < a^2_{\mathrm{IN,RWS3,max}} < P^V_{\mathrm{OUT,RWS2,max}} \tag{A.21}$$

$$P^V_{\mathrm{OUT,RWS2,min}} < a^2_{\mathrm{IN,RWS3,min}} < P^V_{\mathrm{OUT,RWS2,max}} \tag{A.22}$$

substituting these values by using equations A.17, A.18, A.19 and A.20, and asumming similar RWSs ($\mathrm{PCE}_{\mathrm{RWS1}} = \mathrm{PCE}_{\mathrm{RWS2}} = \mathrm{PCE}_{\mathrm{RWS3}}$), the following tolerance condition can be obtained from equations A.21 and A.22:

$$1/4 < \mathrm{PCE}_{\mathrm{RWS2}} < 3/4. \tag{A.23}$$

Thus, in a polarization controller scheme as the proposed, depicted in figure 3.3 b), full polarization control is achieved in a broad range of PCE values, which ultimately results in a higher tolerance to fabrication deviations.

A.3. Extraction of differential losses and group index in a Mach-Zehnder interferometer

In this section, the expresions of the differential losses and the group index between the arms of a Mach-Zehnder interferometer are derived. For this purpose let's consider the Mach Zehnder interferometer.

The transfer function of this structure is given by

$$|H|^2 = \frac{1}{4}\left|e^{-\alpha_1 L_1} e^{j\beta_1 L_1} + e^{-\alpha_2 L_2} e^{j(\beta_2 L_2 + \frac{\pi}{2})}\right|^2. \tag{A.24}$$

In the case of $L_1 = L_2$and defining $\Delta\beta = \beta_2 - \beta_1$, the transfer function can be rewritten as

$$|H|^2 = \frac{1}{4}\left|e^{-\alpha_1 L} + e^{-\alpha_2 L} e^{j\Delta\beta L + \frac{\pi}{2})}\right|^2 \tag{A.25}$$

$$= \frac{1}{4}\left(e^{-2\alpha_1 L} + e^{-2\alpha_2 L} + 2e^{(\alpha_1+\alpha_2)L}\cos(\Delta\beta L)\right). \tag{A.26}$$

As $\beta = f(\lambda)$, the transfer function has a sinusoidal variation with the wavelength, defining the interferogram of the MZI. From this interferogram, the difference between the group index and the losses in both arms can be extracted as shown in the next subsections.

A.3.1. Extraction of the diferential group index

The difference between the group index of the waveguides placed in both arms, can be derived from the free spectral range (FSR) of the interferogram.

For this purpose, let's evaluate the argument of the cosine of equation A.26 at two different wavelengths, λ_1 and λ_2, spaced by the FSR of the interferogram so that, $\lambda_2 = \lambda_1 + \text{FSR} = \lambda_1 + \Delta\lambda$. In those cases, the values of the cosine arguments are:

$$\phi(\lambda_1) = \Delta\beta(\lambda_1)L = \left(\frac{2\pi}{\lambda_1} n_2(\lambda_1) - \frac{2\pi}{\lambda_1} n_1(\lambda_1)\right) L = 2k\pi \tag{A.27}$$

$$\phi(\lambda_2) = \Delta\beta(\lambda_2)L = \left(\frac{2\pi}{\lambda_2} n_2(\lambda_2) - \frac{2\pi}{\lambda_2} n_1(\lambda_2)\right) L = 2(k+1)\pi \tag{A.28}$$

by substraction both equations, we obtain

$$2\pi\left(\frac{1}{\lambda_2} n_2(\lambda_2) - \frac{1}{\lambda_2} n_1(\lambda_2)\right) - 2\pi\left(\frac{1}{\lambda_1} n_2(\lambda_1) - \frac{1}{\lambda_1} n_1(\lambda_1)\right) = \frac{2\pi}{L}. \tag{A.29}$$

Assuming that λ_1 and λ_2 are close enough to consider first order approximation of the dispersion,

$$n(\lambda_2) = n(\lambda_1) + \left.\frac{\delta n(\lambda_1)}{\delta\lambda}\right|_{\lambda_1} \Delta\lambda = n(\lambda_1) + \Delta\lambda n'(\lambda_1), \tag{A.30}$$

and including this expression in A.29, the following expression can be obtained after reordering:

$$\left(\Delta\lambda \frac{n(\lambda_1) + \lambda_1 n'(\lambda_1)}{\lambda_1\lambda_2}\right) - \left(\Delta\lambda \frac{n(\lambda_1) + \lambda_1 n'(\lambda_1)}{\lambda_1\lambda_2}\right) = \frac{1}{L}. \tag{A.31}$$

Finally, when $\lambda_1 \to \lambda_2$, this expresion results in:

$$\Delta n_g = \frac{\lambda^2}{L\Delta\lambda}, \tag{A.32}$$

where $\Delta\lambda$ is the FSR of the interferogram.

A.3.2. Extraction of the diferential losses

The difference between both arms of the interferometer, can be extracted from the "depth" of the interogram. It is easy to deduce from equation A.25 that the minimum and maximum achievable input powers at the output of the interferometer are:

$$P_{MAX} = \frac{e^{-2\alpha_1 L}}{4}\left|1+e^{-(\alpha_2-\alpha_1)L}\right|^2 \tag{A.33}$$

$$P_{MIN} = \frac{e^{-2\alpha_1 L}}{4}\left|1-e^{-(\alpha_2-\alpha_1)L}\right|^2, \tag{A.34}$$

defining the differential losses as $\Delta\alpha = \alpha_2 - \alpha_1$, the ratio P_{MAX}/P_{MIN} can be expressed as

$$\frac{P_{MAX}}{P_{MIN}} = \left|\frac{1+e^{-\Delta\alpha L}}{1-e^{-\Delta\alpha L}}\right|^2 \tag{A.35}$$

and from this expresion, the value of $\Delta\alpha$ can be expressed as a function of P_{MAX}, P_{MIN} and the length of the arms as:

$$\Delta\alpha = \frac{1}{L}\ln\left(\frac{\sqrt{\frac{P_{MAX}}{P_{MIN}}}+1}{\sqrt{\frac{P_{MAX}}{P_{MIN}}}-1}\right) \tag{A.36}$$

B

Resumen en español

B.1. Introducción

La luz ha jugado un papel fundamental a lo largo de la evolución del ser humano, estableciendo diferentes hitos que han marcado nuestra historia, desde el dominio del fuego hace varios millones de años [1], diferenciando a nuestros ancestros del resto de homínidos, hasta los más recientes avances en comunicaciones ópticas [183], que han contribuido al inicio de una nueva era, la era de la información.

El desarrollo de las comunicaciones ópticas, debe su origen a la invención del láser y al desarrollo de la fibra óptica, ambos hitos alcanzados en los años 60 [2], época en la que el término fotónica, definida como la ciencia del control de la luz, fue acuñado. Desde ese entonces, innumerables aplicaciones de la fotónica han emergido en diferentes campos: aplicaciones médicas como la cirugía láser, aplicaciones de sensado en estructuras civiles, aplicaciones fotovoltaicas, etc.

Durante los años sesenta también tuvo lugar el nacimiento de la fotónica integrada. A finales de dicha década, el ingeniero Stewart E. Miller, propuso por vez primera la fabricación de dispositivos ópticos en un mismo substrato [3]. En su artículo, Miller describe las ventajas de la integración de dispositivos fotónicos, y al mismo tiempo advierte de la dificultad de realizar su propuesta. Desde entonces, una parte importante de la actividad investigadora se ha centrado en la integración de aplicaciones fotónicas.

La aplicación de la fotónica que más repercusión ha tenido en la sociedad son las comunicaciones ópticas. Las comunicaciones ópticas conforman la base de Internet, conectando ciudades, países e incluso continentes. Desde su nacimiento, durante la década de los 60, han sufrido un constante crecimiento exponencial, existiendo en la actualidad sistemas comerciales integrados que alcanzan tasas binarias de 100 Gbps, en distancias superiores a los 1000 km [7] .

Por otro lado, durante los últimos años han aparecido un elevado número de aplicaciones y servicios basados en la computación en la nube, lo que ha generado que los enlaces de cobre hasta ahora presentes en los centros de procesamiento de datos hayan alcanzado su límite, empezando una migración a enlaces basados en comunicaciones ópticas [184]. Estos enlaces presentan unas características diferentes a los tradicionales, ya que las distancias son reducidas, y se prima el bajo consumo, un reducido coste y una alta capacidad integración. Así, en la actualidad, hablamos de

aplicaciones de comunicaciones ópticas telecom, donde se prima larga distancia y el elevado régimen binario, y aplicaciones datacom, donde se prima el bajo consumo y las distancias son mucho menores.

Tanto en aplicaciones datacom como aplicaciones telecom, el uso de la polarización de la luz, como un grado de libertad adicional, permite mejorar las prestaciones de los enlaces, a un coste reducido. En el caso de aplicaciones datacom, esquemas basados en la modulación de la polarización han sido propuestos como una alternativa a los esquemas IM-DD, ya que ofrecen una mayor eficiencia espectral y además permiten aplicar técnicas de linealización del canal [8]. En el caso de las aplicaciones telecom, la multiplexación en polarización permite doblar la capacidad de los enlaces, manteniendo la actual infraestructura [9, 114].

Otras de las mejoras de los sistemas de comunicaciones actuales es la ampliación del ancho de banda óptico. La mayoría de los sistemas actuales trabaja en la banda C, sin embargo, en el medio plazo esta banda puede resultar insuficiente. Entre otros factores, el ancho de banda de los receptores queda limitado por la dispersión, que dificulta el funcionamiento del mismo en bandas diferentes a las que fue diseñado. Recientemente, se ha propuesto el uso de estructuras periódicas sub-longitud de onda para implementar metamateriales en los que, a través de la geometría de las guías es posible aplicar ingeniería de la dispersión, lo que ha posibilitado la implementación de dispositivos con un gran ancho de banda [11, 12].

Esta tesis se centra en la implementación de dispositivos que implementan diversidad de polarización. Por un lado, se ha implementado un controlador de polarización integrado, con unas elevadas tolerancias a errores de fabricación. Por otro lado, se ha implementado un receptor coherente con diversidad de polarización. Finalmente, también se ha realizado una aportación en el campo de las estructuras periódicas sublongitud de onda.

Este resumen trata de cubrir las aportaciones realizadas en esta tesis de un modo breve, pero abarcando aquellos detalles necesarios para entender el desarrollo del trabajo. Así, se ha dividido el contenido de la tesis en tres bloques temáticos diferentes, de acuerdo a cada uno de los problemas tratados.

B.2. Control de polarización en óptica integrada

B.2.1. Introducción

El control de polarización tiene una importancia fundamental en diferentes campos de la fotónica con aplicaciones que van desde las comunicaciones ópticas, hasta la tomografía óptica coherente [14], pasando por aplicaciones de distribución de claves cuánticas [15]. Comparado con implementaciones en fibra o en óptica discreta, las implementaciones en óptica integrada presentan ventajas propias de la miniaturización tales como el reducido coste y la mejora de la estabilidad. Sin embargo, la integración de dispositivos que controlan el estado de polarización es compleja, debido fundamentalmente a las bajas tolerancias a errores de fabricación de los mismos [39].

Un controlador de polarización está compuesto esencialmente de dos elementos: rotadores de polarización, con ángulos de rotación que han de ser precisamente fab-

ricados y desfasadores de polarización. Mientras que los desfasadores de polarización pueden ser fácilmente implementados, los rotadores de polarización requieren o bien procesos de fabricación no estándar [185], o bien procesos de fabricación con precisiones del orden de las unidades de nanómetro [39]. De hecho, los controladores de polarización propuestos en [120, 121], han sido demostrados empleando soluciones de integración híbridas. Por otro lado, los controladores de polarización presentados en [70, 118] están basados en una arquitectura alternativa, pero requieren rotadores y separadores de polarización de muy altas prestaciones. Por último, la propuesta realizada en [119], basada en efectos cuánticos a escala macroscópica, presenta unas magníficas prestaciones, pero emplea guías de onda "out-of-plane" lo que dificulta su fabricación.

Así, los rotadores de polarización con mayores prestaciones reportados hasta el momento, presentan un ratio de extinción de polarización (PER, por sus siglas en inglés) de ±10 dB para esquemas totalmente integrados y ±20 dB para esquemas de integración híbridos, que sacrifican su integrabilidad en aras de sus prestaciones.

En esta tesis, se ha implementado un controlador de polarización totalmente integrado, superando el balance integrabilidad-prestaciones existente hasta el momento. El dispositivo en cuestión presenta un ratio de extinción de polarización de ±20 dB, siendo integrable y compatible con las tecnologías de fabricación CMOS. Además permite ser sintonizado en la banda C, y presenta elevadas tolerancias de fabricación. Para ello, el dispositivo fabricado consta de guías rotadoras de polarización y desfasadores de polarización que, además de ser empleados para sintonizar el dispositivo, se usan para compensar los errores de fabricación.

B.2.2. Operación del dispositivo

La arquitectura del dispositivo se muestra en la B.1 a), estando formada por tres guías rotadoras de polarización y tres desfasadores de polarización. Las guías rotadoras de polarización se encargarán de establecer el PER del estado de polarización deseado, alterando también la fase de polarización. Por su parte, los desfasadores de polarización controlarán la fase de polarización sin alterar el PER.

La operación del dispositivo está ilustrada en la esfera de Poincaré de la figura B.1 b). Por claridad, se ha considerado que el dispositivo presenta una polarización lineal horizontal a su entrada, mientras que a la salida la polarización es circular a derechas.

En primer lugar se realiza una rotación de polarización, en el primer PR (trayecto AB en la esfera). Seguidamente dos parejas TPPS-PR se encargarán de sintetizar a su salida un estado de polarización con el PER deseado. Para ello los TPPSs se encargan de ajustar la fase del estado de polarización con el que se alimenta cada uno de los rotadores de polarización, a fin de obtener el PER deseado, (trayecto BF en la esfera). Finalmente el último TPPS se encarga de proporcionar el desfase de polarización a la salida del dispositivo, obteniendo así el estado de polarización deseado (trayecto FG en la esfera) [186].

A diferencia de otros esquemas propuestos en la literatura, para que el esquema propuesto funcione adecuadamente no es necesario que las guías rotadoras presenten una eficiencia de conversión de polarización (PCE) determinada, como se propone en [37, 120, 121], si no que es necesario que dicha eficiencia esté en el margen:

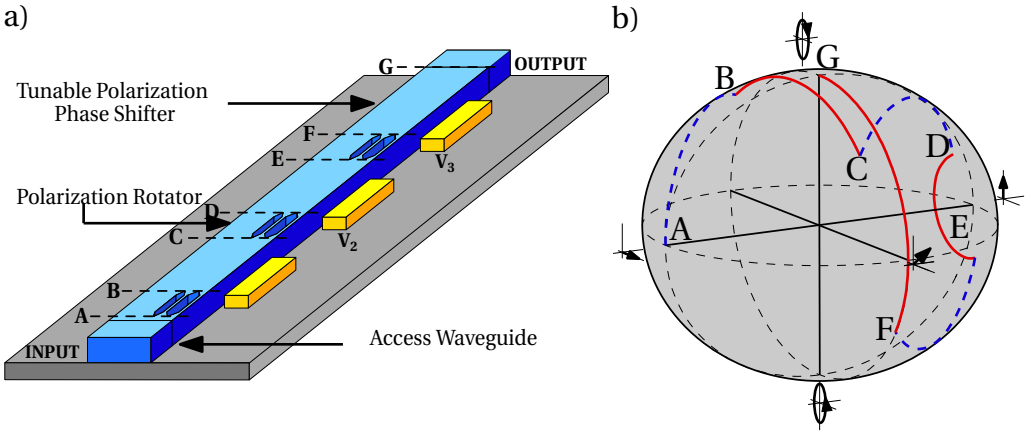

Figure B.1.: a)Arquitectura del controlador de polarización propuesto. b) Operación del controlador de polarización sobre la esfera de Poincaré.

$$\frac{1}{4} < \mathrm{PCE} < \frac{3}{4} \tag{B.1}$$

Dado que esta condición se puede cumplir en un rango de desviaciones de fabricación elevado, el esquema propuesto presenta unas altas tolerancias a errores de fabricación.

B.2.3. Implementación del dispositivo

Para demostrar el esquema propuesto experimentalmente se ha fabricado un prototipo en la tecnología de Silicio sobre aislante (SOI, por sus siglas en inglés). Las dimensiones de la guía estándar en esta plataforma son de $490 \times 260\,\mathrm{nm}$, mostrada en la figura B.2 a), estando cubierto por una capa de polímero SU-8.

La guía rotadora de polarización ha sido implementada siguiendo el diseño propuesto en [88]. En la figura B.2 b) se muestra la sección transversal de la guía rotadora de polarización, donde se han incluido las dimensiones de la misma. La longitud de las guías rotadoras de polarización es de $20\,\mu\mathrm{m}$. Nótese que las dimensiones exactas no son cruciales para que el dispositivo opere correctamente, siempre y cuando el PCE del dispositivo cumpla la condición B.1.

Para implementar el TPPS, se aprovecha que los coeficientes termo-ópticos del SU-8 y del silicio tienen signo opuesto, tal y como se muestra en la tabla B.1. Incluyendo estos coeficientes en el simulador electromagnético es posible calcular los coeficientes termo-ópticos de los modos TE y TM. Así, a partir de estos coeficientes y del índice efectivo de los modos TE y TM es posible obtener el desfase de polarización que introducirá el TPPS al incrementar su temperatura, empleando para ello la siguiente ecuación:

$$\Delta\rho = 2\pi \frac{L_{\mathrm{TPPS}}}{\lambda} \left[\left(n_{\mathrm{eff}}^{\mathrm{TE}} - n_{\mathrm{eff}}^{\mathrm{TM}} \right) + \Delta T \left(\frac{\mathrm{d}n_{\mathrm{eff}}^{\mathrm{TE}}}{\mathrm{d}T} - \frac{\mathrm{d}n_{\mathrm{eff}}^{\mathrm{TM}}}{\mathrm{d}T} \right) \right]. \tag{B.2}$$

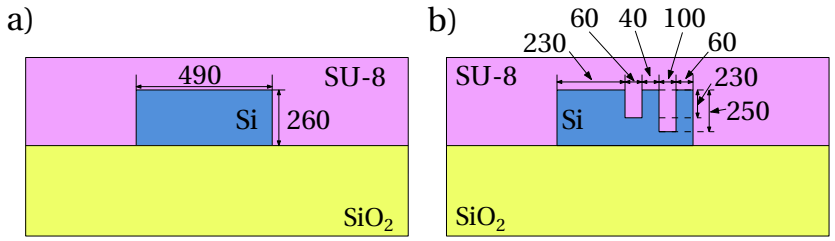

Figure B.2.: a) Sección transversal de la guía estándar de la plataforma en la que se ha fabricado el controlador de polarización. b) Sección transversal de la guía rotadora de polarización. Todas las dimensiones están en nm.

Material	Índice de refracción (r.i.u.)	Coeficiente termo-óptico ($°C^{-1}$)
Si	3.476	1.8×10^{-4}
SiO_2	1.44	1×10^{-5}
SU-8	1.58	-1.1×10^{-4}

Table B.1.: Índice de refracción y coeficiente termo-óptico de los materiales empleados para la implementación del controlador de polarización.

En esta ecuación se puede observar que a mayor longitud del TPPS, menor será el incremento de temperatura necesario para introducir un determinado desfase de polarización. No obstante, cuanto mayor sea la longitud, menor será el ancho de banda del dispositivo. Para elegir la longitud óptima se ha estimado el ancho de banda del dispositivo numéricamente, a través de su modelo basado en matrices de Jones. Por otro lado se ha calculado para diferentes incrementos de temperatura, cual es el desfase máximo introducido por el TPPS en función de su longitud. Los resultados de este breve estudio, están ilustrados en la figura B.3. Se puede observar que, con una longitud de 700µm es posible obtener desfases de hasta 2π con incrementos de temperatura inferiores a 40°C. No obstante, dado que el ancho de banda no es crítico, finalmente se optó por elegir una longitud de 1 mm a fin de emplear incrementos de temperatura menores.

Para aumentar la temperatura de la estructura, se ha implementado un calentador usando guías eléctricas situadas junto a la guía fotónica. Estas guías, con una sección transversal de $2 \times 0.1\,\mu m^2$, incrementan su temperatura al paso de una corriente a través de las mismas. Dichas guías se han situado a 2µm de la guía fotónica, con el fin de evitar que el campo evanescente interactúe con la estructura metálica introduciendo pérdidas en el TPPS.

Finalmente el dispositivo, junto a otras estructuras de prueba, fueron fabricados en instalaciones externas a las de la universidad de Málaga, concretamente en la Universidad Paris-Sud.

B.2.4. Caracterización del dispositivo

Para comprobar el correcto funcionamiento del dispositivo se han realizado cuatro pruebas diferentes, empleando para ello el set-up ilustrado en la figura B.4 a) y b). En

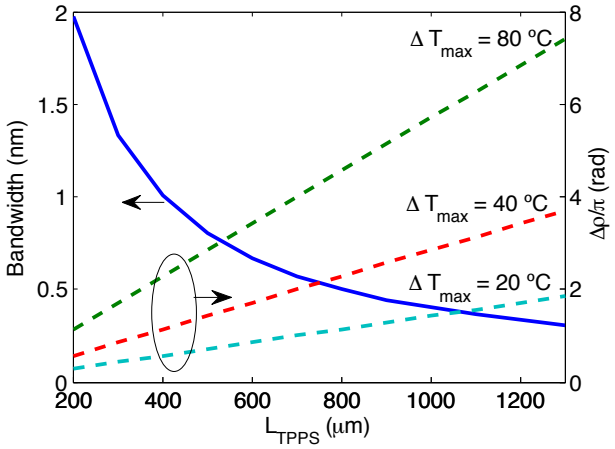

Figure B.3.: Eje izquierdo: Ancho de banda del controlador de polarización en función de la longitud de los TPPSs. Eje derecho: Incremento de fase en un TPPS para diferentes incrementos de temperatura en función de la longitud del TPPS.

este set-up luz horizontalmente polarizada es generada en un láser sintonizadble en longitud de onda. Para inyectar la luz en el chip se usa una fibra acabada en lente, que además es mantenedora de polarización. A la salida del chip la luz es recogida por un objetivo de microscopio y filtrada por un polarizador lineal, situado sobre una montura rotadora. Finalmente, la salida del polarizador es recogida por una cámara infrarroja que permite medir la potencia del haz incidente. El set-up ha sido previamente calibrado, obteniendo un PER máximo medible de 30 dB, lo que se traduce en un rango de PER medible de hasta 60 dB.

a) b)

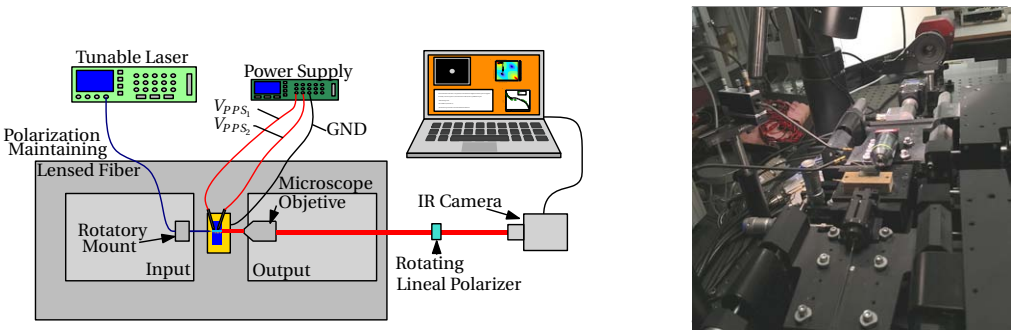

Figure B.4.: Esquemático del set-up de medida (a) e imagen del set-up (b).

El primer experimento tiene como objetivo mostrar que un único TPPS puede introducir desfases de polarización de hasta 2π radianes. Para ello se inyectó luz polarizada a 45° en una estructura de prueba, consistente un un TPPS aislado. Incrementando la temperatura del TPPS, el desfase de polarización a la salida se verá modificado con lo que el estado de polarización a la salida variará desde lineal a 45°, a circular a derechas, posteriormente a lineal a -45° y finalmente a circular a izquierdas. Para comprobar el correcto funcionamiento, se situó el polarizador lineal a 45°,

detectando una señal sinusoidal del tipo $\cos^2\left(\frac{\Delta\rho}{2}\right)$, de la cual es posible extraer la fase de polarización. Incrementando la potencia aplicada al TPPS se observaron diferentes ciclos de esta señal, observando una eficiencia de ajuste de 70 rad/W.

El segundo experimento tenía como objetivo generar estados de polarización con el mayor rango de PER posible, ya que en gran medida es lo que determina las prestaciones del dispositivo. En este caso se excitó el dispositivo con una polarización horizontal, y se generaron estados de polarización con un PER de +20 dB y -20 dB. El algoritmo de ajuste se basó en minimizar la potencia en el estado de polarización ortogonal. Este mismo proceso se realizó a diferentes longitudes de onda, con el fin de demostrar que el dispositivo es sintonizable a lo largo de la banda C, tal y como se muestra en la figura B.5, donde se ha añadido el ER de la guía rotadora de polarización, con el fin de comprobar que la condición de tolerancia se cumple a lo largo del rango de longitudes de onda.

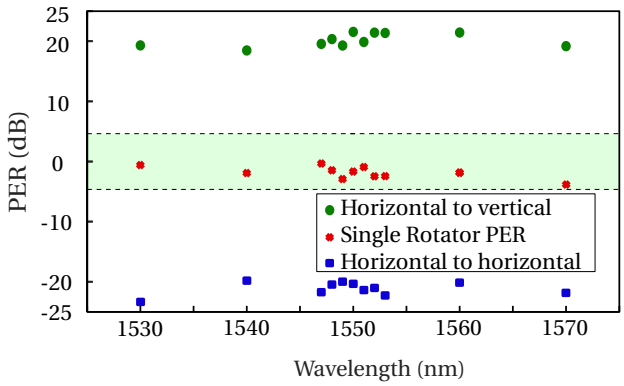

Figure B.5.: PER medido a la salida del controlador de polarización a diferentes longitudes de onda, excitanto el mismo con polarización horizontal y sintonizándolo para obtener polarización horizontal y vertical a la salida. Como se puede observar, es posible obtener un rango de PER de 40 dB, (desde -20 a +20 dB) a lo largo de la banda C.

El tercer experimento perseguía demostrar que el dispositivo puede generar estados de polarización con un PER arbitrario. Para ello supongamos que $(\rho_{1,y}, \rho_{2,y})$ y $(\rho_{1,x}, \rho_{2,x})$ son los desfases de polarización introducidos en los TPPS para conseguir polarizaciones horizontal y vertical a la salida, respectivamente. Para generar valores intermedios de PER, partimos del estado de polarización vertical a la salida con desfases $(\rho_{1,y}, \rho_{2,y})$ e incrementamos V_1 hasta alcanzar $(\rho_{1,x}, \rho_{2,y})$. Posteriormente V_2 es modificado del mismo modo hasta alcanzar $(\rho_{1,x}, \rho_{2,x})$, obteniendo así polarización horizontal a la salida. Los valores intermedios de ρ_1 y ρ_2 producirán estados de polarización con PER intermedio. El resultado de este experimento se muestra en la figura B.6. En la figura B.6 a) se muestra un mapa de contorno con el PER simulado en función de los desfases de polarización ρ_1 y ρ_2. Sobre dicho mapa de contorno se ha superpuesto el camino resultante de las combinaciones (ρ_1, ρ_2), donde la línea continua se corresponde con variaciones en ρ_1 y la línea discontinua con variaciones en ρ_2. Por otro lado, en la figura B.6 b), se muestran el PER medido y el simulado. Como se puede observar existe una gran concordancia entre ambas curvas, lo que confirma

que el dispositivo puede generar estados de polarización con cualquier PER.

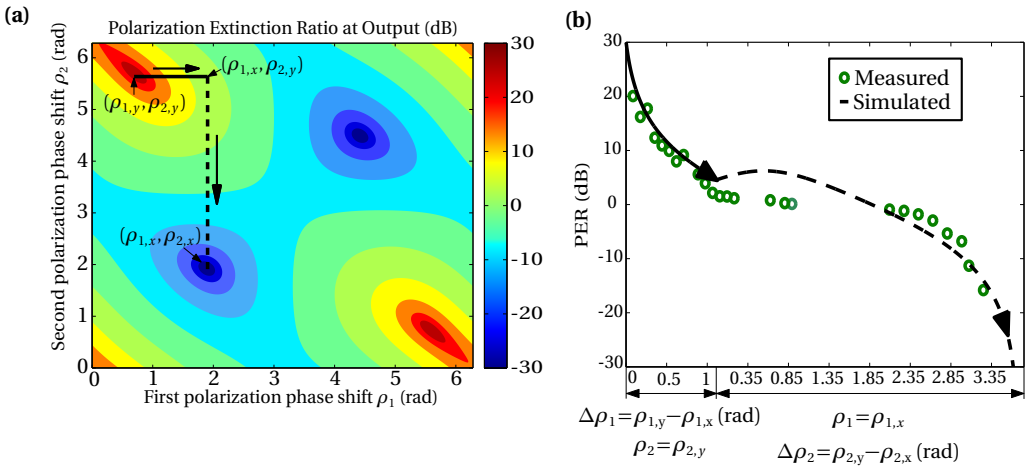

Figure B.6.: (a) PER a la salida del controlador de polarización en función de los desfases de polarización introducidos en los TPPSs, considerando polarización horizontal a la entrada. (b) PER medido comparado con el PER simulado, correspondiente al camino mostrado en (a).

Para poder afirmar que el dispositivo puede generar cualquier estado de polarización, no solo es necesario demostrar que se pueden generar estados de polarización con PER arbitrario, sino también que la fase de polarización a la salida puede ser arbitrariamente modificada. El cuarto experimento consistió en generar un estado de polarización con un PER arbitrario, y modificar la fase del mismo arbitrariamente en un rango de 0 a 2π. Considerando que set-up de medida permite obtener los parámetros de Stokes S_1 y S_2, y asumiendo que la luz del láser está totalmente polarizada, es posible obtener el parámetro de Stokes S_3. En la figura B.7 se muestra el resultado de este experimento, donde se puede observar como la fase de polarización varía en un rango de 2π.

B.3. Receptor DP-QPSK monolíticamente integrado sin separadores de polarización

En la última década, el tráfico IP en los nodos centrales de la red ha crecido de forma exponencial debido entre otros factores a la aparición de nuevos servicios multimedia, que cada vez demandan un mayor ancho de banda [5]. Además, recientes trabajos, proponen una integración homogénea entre la red móvil y la red cableada [187], con lo que es de prever que el crecimiento el exponencial del tráfico IP siga manteniéndose en los próximos años.

Una de las soluciones propuestas para la provisión del ancho de banda requerido, pasa por la migración de sistemas basados en detección directa a sistemas ópticos coherentes, que además de modular información en la amplitud del campo, también la modulan en la fase. Por otro lado, el uso de la diversidad de polarización permite duplicar la capacidad de los enlaces actuales, multiplexando la información en dos

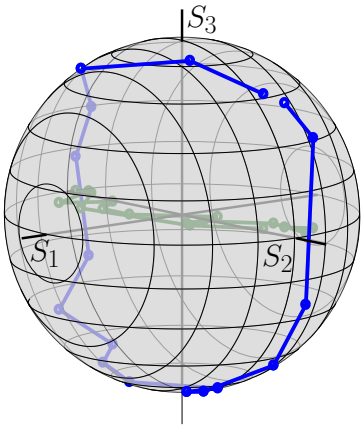

Figure B.7.: Estado de polarización medido al incrementar el voltaje aplicado en el tercer calentador, mostrando que cualquier fase de polarización puede ser obtenida. La traza azul se puede obtener de los puntos medidos (traza verde) proyectando los mismos en la superficie de la esfera de Poincaré.

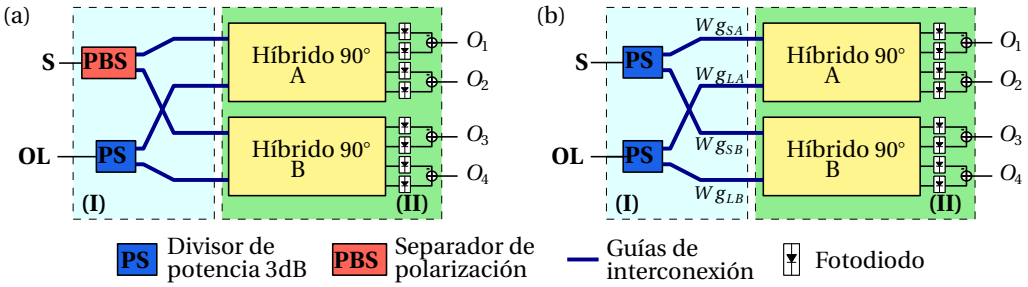

Figure B.8.: Diagrama de bloques de un receptor DP-QPSK. (a) Esquema tradicional basado en PBS [20]. (b) Receptor PBS-less [21].

estados de polarización ortogonales en la fibra.

Para la implementación de estos sistemas, el Optical Internetworking Forum (OIF), propone en un esquema de receptor integrado coherente con diversidad de polarización como el mostrado en la figura B.8 a), compuesto por una red de diversidad de polarización (I) y dos receptores coherentes (II). La red de diversidad de polarización, está esencialmente compuesta por un separador de polarización y un divisor de potencia, aunque la OIF también contempla el uso de dos separadores de polarización. Los receptores coherentes, a su vez, están formados por un híbrido a 90º y cuatro fotodiodos.

El esquema propuesto por el OIF, supone un desafío en cunatoa integración, pues las propuestas de integración de los separadores de polarización realizadas hasta el momento son, por lo general, muy poco tolerantes a errores de fabricación, lo que provoca que el rendimiento de fabricación de dicho dispositivo sea muy bajo. Así, para obtener mejores rendimientos de fabricación, en el acuerdo de implementación del OIF, no se exige la integración monolítica de los separadores de polarización, lo que ha provocado que en la práctica, la mayoría de los receptores comerciales no integren monolíticamente la red de diversidad de polarización, lo que en última in-

stancia se traduce en dispositivos más costosos.

En esta parte de la tesis, se ha diseñado un receptor coherente con diversidad de polarización, integrando monolíticamente la red de diversidad de polarización. Dicha red de diversidad de polarización, publicada en [21], prescinde del uso de separadores de polarización, mejorando así las tolerancias de fabricación del dispositivo. La red de diversidad de polarización propuesta, se muestra en la figura B.8 b), y como se puede observar sólo incluye divisores de potencia a 3 dB y cuatro guías de interconexión que han de ser birrefringentes.

B.3.1. Funcionamiento de la red de diversidad de polarización

La red de diversidad de polarización propuesta en [21], a diferencia de las propuestas por el OIF [20], no separa ambas polarizaciones a su salida, sino que proporciona señales con ambas polarizaciones mezcladas, y un cierto desfase de polarización entre ellas. Gracias al desfase de polarización introducido es posible obtener la información multiplexada en cada uno de los estados de polarización, aplicando técnicas de procesado de señal habituales.

El desfase de polarización introducido en una guía birrefringente obedece a la siguiente expresión:

$$\rho = BL \tag{B.3}$$

Donde B es la birefringencia de la guía y L su longitud. Para que el esquema funcione adecuadamente, se ha de cumplir que los desfases de polarización introducidos en cada una de las guías de interconexión cumpla la siguiente condición:

$$\phi_{Dist} = (\rho_{SA} - \rho_{LA}) - (\rho_{SB} - \rho_{LB}) = (2p+1)\cdot\pi, s \;\; p = 0, 1, \ldots, . \tag{B.4}$$

Para cumplir dicha condición existen diferentes alternativas. No obstante, la alternativa que ofrece una mejor tolerancia a errores de fabricación consiste en mantener todas las guías con la misma birefringencia, B_{NOM} , y, simultáneamente, escoger caminos iguales dos a dos, es decir $L_{SA} = L_{LB}$ y $L_{SB} = L_{LA}$, con lo que se conserva la simetría de la red. Así, la condición B.4 puede expresarse en función de la birefringencia nominal y la diferencia de caminos ($\Delta L = L_{SA} - L_{SB}$):

$$\phi_{Dist} = 2B\Delta L = \pi \tag{B.5}$$

B.3.2. Diseño e implementación del receptor

El receptor se ha implementado en tecnología de fosfuro de indio (InP), ofrecida por el instituto alemán Fraunhofer HHI, a través de la plataforma MWP Jeppix. De las estructuras de guiado ofrecidas, se ha optado por emplear la de mayor profundidad de grabado (inset figura B.9), ya que es la que permite utilizar radios de curvatura menores (250µm) y conduce por tanto a diseños más compactos.

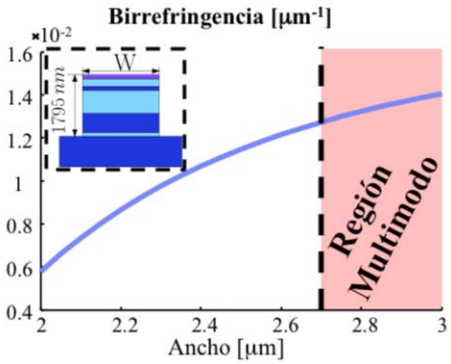

Figure B.9.: birefringencia de la guía en función del ancho, W. (Inset) Geometría transversal de la guía utilizada.

B.3.2.1. Diseño de la red de diversidad de polarización

Para implementar los divisores de potencia de la red de diversidad de polarización se han diseñados dos MMI's 1×2. Esta solución, además de la sencillez en su implementación, es muy tolerante a errores de fabricación y en esta tecnología presenta un comportamiento poco dependiente de la polarización.

En cuanto a las guías de interconexión, su diseño se reduce a la elección del ancho de las mismas, que ha de cumplir los siguientes requisitos: operar en régimen monomodo, ser tolerante a errores de fabricación y presentar la máxima birefringencia posible. Como se puede observar en la figura B.9, a mayor ancho de la guía mayor es la birefringencia y menor dependencia presenta la misma respecto a variaciones en el ancho. No obstante para anchos mayores a 2.8 µm, los modos superiores de la guía dejan de estar al corte. Así, el ancho elegido es de 2.4 µm, ya que está lo suficientemente alejado de la zona multimodo, sin comprometer las tolerancias de fabricación. Para dicho ancho la birefringencia de las guías es $10.6\,\mathrm{mm}^{-1}$, y la diferencia de caminos a implementar para cumplir la condición de diseño debe ser de 147 µm, calculada según la ecuación B.5. Fijado este valor del ancho, se ha realizado un análisis de tolerancias considerando otras fuentes de error [162]. De dicho análisis se concluye que la máxima desviación con respecto a la condición B.4 es de $\pi/4$, lo que se traduce en una penalización en sensibilidad inferior a 1 dB, respecto del caso ideal [21].

B.3.2.2. Diseño de los híbridos a 90°

Los híbridos a 90° se encargan de combinar la señal recibida con el oscilador local, con el fin de poder recuperar las componentes I y Q de la señal recibida.

Existen diferentes alternativas para implementar los híbridos a 90° [149–152]. En este caso, se ha optado por implementarlo mediante un MMI 4×4 del que solo se usan dos entradas. Esta opción se ha escogido debido a las tolerancias a errores de fabricación y al buen comportamiento en ancho de banda que presenta. El diseño se ha optimizado para presentar una mínima dependencia con la polarización, además de perseguir la consecución de las especificaciones que el OIF fija en la banda C.

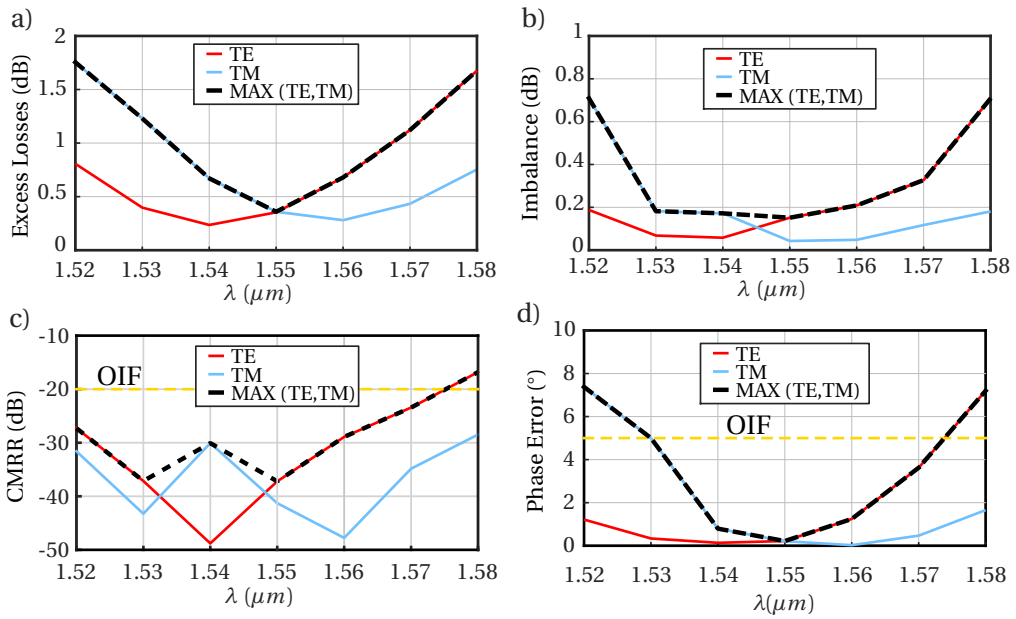

Figure B.10.: Figuras de mérito del híbrido a 90° diseñado, implementado mediante un MMI 2×4.

Como figuras de mérito para su diseño se han empleado las cuatro más comunes : el rechazo al modo común (CMRR), el error de fase entre las salidas, el desbalanceo entre las salidas y las pérdidas de exceso. En la figura B.10 se muestra el valor de estas figuras de mérito a lo largo de la banda C.

Como se puede observar, el CMRR es inferior a -20 dB a lo largo de la banda C, las pérdidas de exceso se sitúan bajo los 1.3 dB, el desbalanceo es menor a 0.5 dB y el error de fase máximo no supera los 5°. Tras el diseño del híbrido, se ha realizado un análisis de tolerancias del mismo, considerando $\lambda = 1550\,\text{nm}$. Así, se ha comprobado que en el peor de los casos, determinado por la máxima variación en el ancho de la zona multimodo, el dispositivo sigue cumpliendo las especificaciones del OIF.

B.3.2.3. Diseño de la red de salida

Esta red se encarga de interconectar las salidas de los híbridos a 90° con los fotodiodos. Su diseño ha de tener como objetivo principal el garantizar que las señales que recorren los diferentes caminos no sufran diferentes variaciones en su amplitud. Para conseguirlo, se ha diseñado una red en la que cada uno de los cuatro caminos contiene el mismo número de curvas y de cruces, con lo que es de esperar que la respuesta en amplitud de los diferentes caminos sea similar. Por otro lado se ha procurado que la diferencia de longitud entre los caminos sea mínima, estando situada en torno a los 70 µm, e introduciendo una diferencia de retardo de 0.7 ps, cumpliendo especificaciones OIF.

En este caso el ancho de las guías de interconexión y el radio de curvatura son los recomendados por HHI ($W = 2\,\mu\text{m}$ y $R = 250\,\mu\text{m}$ respectivamente). Los cruces se han realizado a 90° y, al igual que se hizo en la red de diversidad de polarización, el an-

cho de las guías en el cruce se aumenta hasta 4µm para minimizar las pérdidas y el crosstalk.

B.3.3. Caracterización previa del dispositivo

La primera caracterización realizada sobre los dispositivos fabricados ha consistido en la evaluación de la respuesta en amplitud (responsividad) del receptor, ignorando la respuesta en polarización y en fase del mismo. La caracterización se ha realizado empleando el esquema de la B.11. Para ello luz generada en un láser sintonizable es empleada para excitar el circuito, para posteriormente medir la fotocorriente generada en cada uno de los fotodiodos.

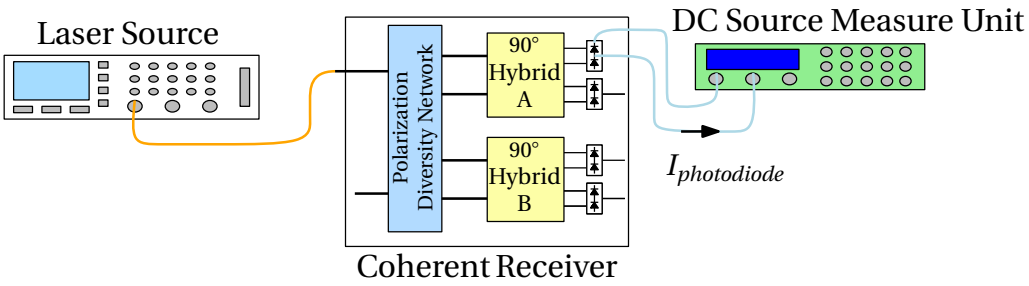

Figure B.11.: Set-up empleado para la caracterización previa del receptor coherente.

Dado que el comportamiento en ancho de banda del receptor está limitado por los híbridos a 90º, la respuesta medida se corresponde en esencia con la respuesta de los híbridos, exceptuando el factor de escala que incluye las pérdidas de inserción del resto de elementos. En la figura B.12 se comparan la respuesta en amplitud medida con la respuesta en amplitud simulada para el híbrido a 90º, observando una gran discrepancia entre ambas respuestas. Tras realizar diversos análisis se ha llegado a la conclusión de que se ha producido un error de fabricación en el ancho de las guías del orden de 600 nm, muy superior al especificado en la plataforma. Con este error en el ancho, es de esperar que la red de diversidad de polarización tampoco funcione adecuadamente. Tras contactar con los responsables de la fabricación, se ha acordado volver fabricar el dispositivo. En el momento en el que se redactan estas líneas, la fabricación del dispositivo sigue sin concluir.

B.4. Pérdidas por leakage en guías SWG

Las redes sub-longitud de onda, SWG por sus siglas en inglés son estructuras periódicas, cuyo periodo espacial es menor que la longitud de onda de trabajo, suprimiendo los efectos de difracción. En dispositivos SWG la luz se propaga en forma de modos Bloch-Floquet, que en teoría no presentan pérdidas, al igual que los modos de una guía convencional. De este modo, una estructura SWG se comporta como un metamaterial cuyas propiedades ópticas, tales como índice de refracción, dispersión y birefringencia, pueden ser modificados.

Estos dispositivos fueron propuestos por primera vez a principios de los años noventa, pero la tecnología de fabricación en aquel tiempo dificultó su implementación [22].

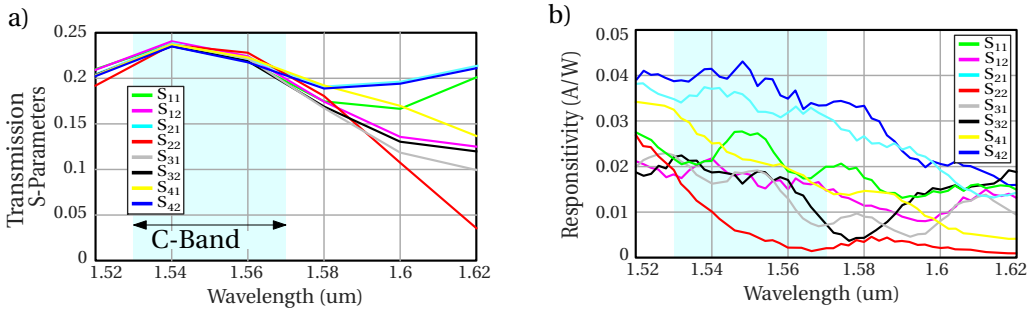

Figure B.12.: a)Parámetros S de transmisión del MMI 2×4 diseñado. b) Responsividad medida del receptor coherente. Idealmente, ambas gráficas deberían tener la misma tendencia.

Sin embargo, las recientes mejoras en los procesos de fabricación han permitido desarrollar dispositivos que exploten las ventajas de las estructuras SWG, con aplicaciones que van desde acopladores chip fibra de altas prestaciones, hasta dispositivos de banda ancha [11, 171].

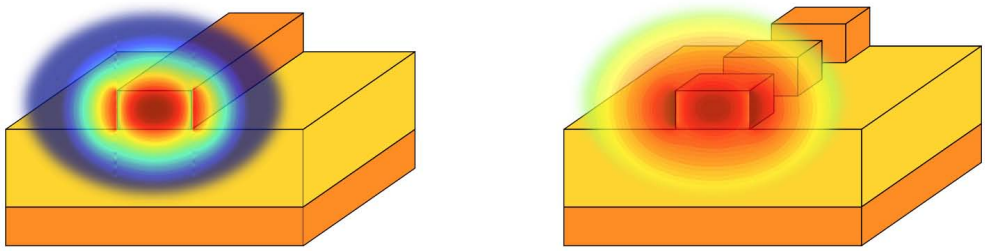

Figure B.13.: Campo en guía Si-wire vs. campo en guía SWG. Como se puede observar, el campo en la guía SWG se encuentra mucho más expandido que en el Si-wire.

La implementación de dispositivos periódicos en plataformas que en su origen no fueron concebidas para ello como ocurre con la plataforma de Silicio sobre aislante, SOI, puede acarrear problemas de pérdidas por fuga al substrato. Tal y como se muestra en la figura B.13, el confinamiento del campo es menor en guías SWG, con lo que si el grosor del BOX no es suficiente, el campo evanescente puede interactuar con el substrato, originando pérdidas por fuga al substrato, comúnmente denominadas pérdidas por leakage. Por lo tanto, tener en cuenta las pérdidas por leakage durante el proceso de diseño de dispositivos SWG es fundamental, a fin de evitar el diseño de dispositivos con pérdidas de exceso desmesuradas.

No obstante, la simulación de las pérdidas por leakage ni siquiera es trivial en guías convencionales, siendo aún más dificultosa en guías SWG. El trabajo realizado en esta parte de la tesis se ha centrado en proveer soluciones que permitan estimar de un modo simple las pérdidas por leakage que una guía SWG puede presentar. Para ello se ha demostrado numérica y experimentalmente que existe una relación exponencial, independiente de la geometría de la guía, entre las pérdidas por leakage y el índice

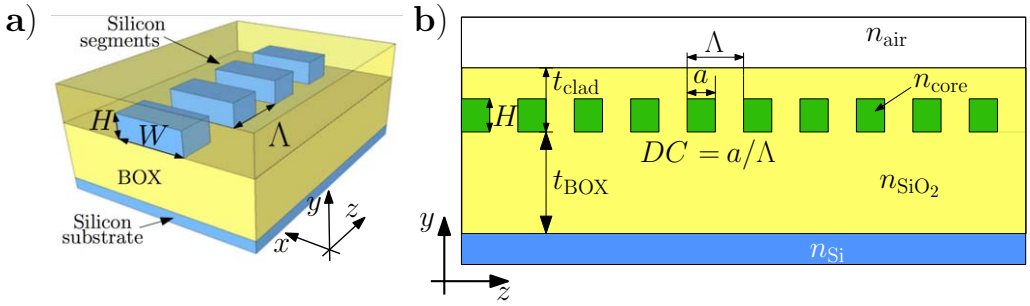

Figure B.14.: a) Guía SWG 3D. b) Estructura 2D equivalente a la guía 3D mostrada en a). El valor de n_{core} es el resultante de aplicar el método del índice efectivo en la dirección x.

efectivo del campo que se propaga a través de una guía SWG.

B.4.1. Demostración numérica de la relación entre el índice efectivo y las pérdidas por leakage en guías SWG.

Para la demostración numérica de dicha relación, nos remitiremos a la guía SWG mostrada en la figura B.14 a), y estudiaremos el índice efectivo y las pérdidas por leakage del campo que se propaga por la guía en función de los parámetros estructurales de la misma: periodo espacial (Λ), ciclo de trabajo (DC), ancho y alto de la guía, y grosor del BOX, considerando únicamente la polarización TE en un rango de longitudes de onda de 1500 a 1600 nm.

En primer lugar se ha comprobado si es posible realizar esta demostración en base a aproximaciones 2D, evitando así tener que emplear simulaciones 3D, que requieren una mayor cantidad de recursos hardware así como unmayor tiempo de cómputo. Para ello se ha empleado el método del índice effectivo, que nos permite transformar el problema original 3D, en un problema 2D equivalente. Así, se han analizado simultáneamente en 2D y en 3D, el valor del índice efectivo y las pérdidas por leakage del campo que se propaga por una guía SWG con un ancho de 400 nm, un alto de 220 nm, y un periodo espacial de 200 nm, considerando un grosor del BOX de 2µm, en función del ciclo de trabajo.

Los resultados de este análisis se muestran en la figura B.15. Se puede observar que para un mismo valor del ciclo de trabajo (misma estructura física) las simulaciones 2D sobreestiman el índice efectivo, y por lo tanto subestiman las pérdidas por leakage, en comparación con la simulación 3D (figuras B.15 a) y b)). No obstante, para un mismo valor del índice efectivo, tal y como se observa en la figura B.15 c), las simulaciones 2D proporcionan un valor más elevado de las pérdidas por leakage. Así, podemos afirmar que las simulaciones 2D sobreestiman las pérdidas por leakage, y podríamos emplearlas para demostrar la relación numérica entre el índice efectivo y las pérdidas por leakage. Por otro lado, es posible observar que la relación numérica existente posee una naturaleza exponencial, y puede ser expresada mediante la siguiente ecuación:

$$\text{Loss(dB/cm)} = \exp(\kappa(n_{eff} - n_m)) \tag{B.6}$$

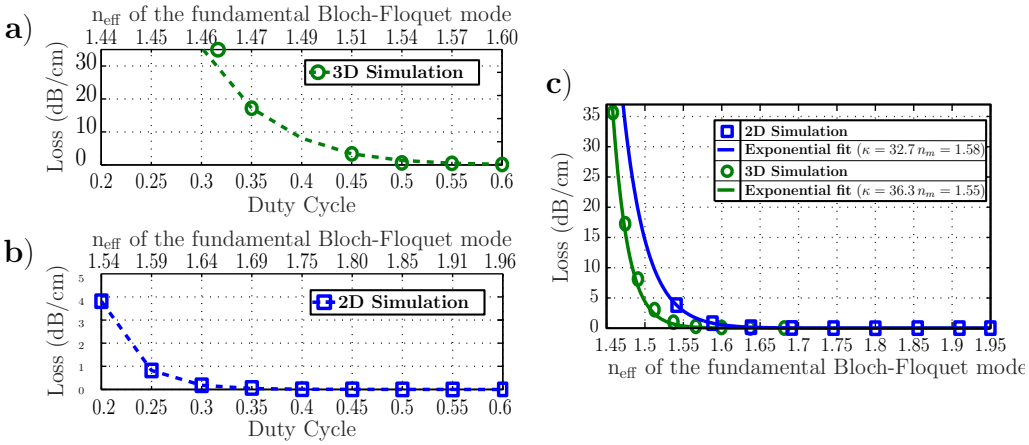

Figure B.15.: a) Variación de las pérdidas por leakage en función del ciclo de trabajo, calculado en una guía SWG 3D. b) Variación de las pérdidas por leakage en función del ciclo de trabajo, calculado en una estructura 2D equivalente a la guía SWG 3D. c) Pérdidas por fuga al substrato en función del índice del modo que se propaga por la estructura periódica, para el caso 2D (azul) y para el caso 3D (verde).

Para completar la demostración numérica de esta relación, se ha procedido a analizar un amplio conjunto de geometrías de la guía SWG, para grosores del BOX de 2 y 3 µm y diferentes combinaciones de ciclo de trabajo, periodo espacial, ancho de la guía, modelado a través del índice del núcleo, altura de la guía y longitud de onda de trabajo.

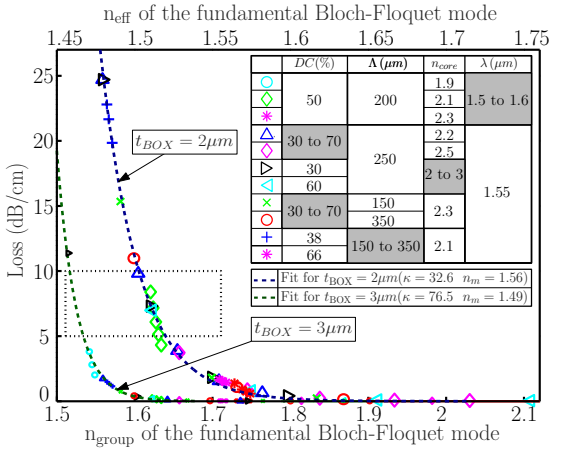

Figure B.16.: a) Pérdidas por leakage calculadas para diferentes parámentros estructurales de la guía SWG, expresadas en función del índice efectivo del modo Bloch-Floquet.

El resultado de este análisis se muestra en la figura B.16, donde puede comprobarse que la relación exponencial se sigue cumpliendo. Además, se ha mostrado dicha relación en función del índice de grupo, con el fin de poder comparar el resultado

teórico con el experimental. De esta figura se puede concluir que para un determinado grosor del BOX, las pérdidas por leakage en guías SWG quedan determinadas por el índice efectivo del modo, siendo esta relación independiente de la geometría de la guía.

B.4.2. Demostración experimental de la relación entre el índice efectivo y las pérdidas por leakage en guías SWG.

Para validar experimentalmente los resultados numéricos, se fabricó y caracterizó un conjunto de guías SWG, con diferentes periodos y ciclos de trabajo. Dichas guías se fabricaron en tecnología de Silicio (SOI), con una altura de la capa de silicio de 220 nm y un grosor del BOX de 2µm. Una vez las estructuras fueron definidas se cubrieron con una capa SiO_2, con un grosor de 700 nm. Durante la simulación se comprobó que esta capa no afectaba sustancialmente a las pérdidas por leakage.

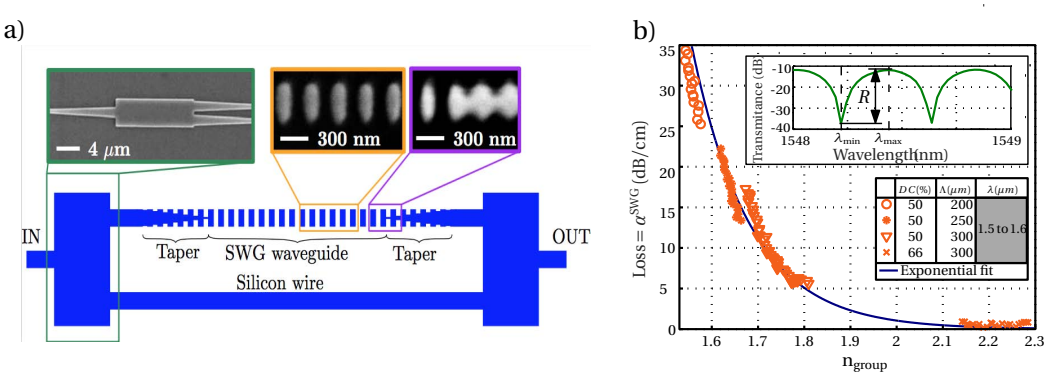

Figure B.17.: a) Interferómetro de Mach Zehnder implementado para facilitar la caracterización de la guía SWG. b) Resultado de la caracterización de las guías SWG. Se puede observar la tendencia exponencial, predicha numéricamente.

Para caracterizar las guías, éstas se incluyeron dentro de un interferómetro Mach Zehnder, MZI por sus siglas en inglés, tal y como se muestran en la figura B.17 a), donde se han incluido algunas imágenes de las estructuras fabricadas, obtenidas con el microscopio de barrido electrónico. En uno de los brazos se incluyó una guía Si-wire, mientras que el otro incluye la guía SWG, junto a los tapers encargados implementar la transición entre las guías de interconexión y las guías SWG. Los dos brazos del interferómetro tienen la misma longitud, lo que permite calcular a partir del espectro de transmisión del interferómetro la diferencia entre las pérdidas de ambas guías y la diferencia entre los índices de grupo de ambas guías. Para realizar las medidas se ha empleado un láser ajustable en longitud de onda, cuya salida es transmitida a través de una fibra SMF-28, que se acopla al chip a través de un grating coupler [23]. A la salida del MZI, se emplea otro grating coupler para acoplar la salida a otra fibra, que transportará la señal a un fotodiodo.

Así, para cada guía SWG incluida dentro de un MZI, se ha obtenido un interferograma en el rango de longitudes de onda de 1500 a 1600 nm, (obsérvese un detalle de este interferograma en el inset de la figura B.17 b). A partir de cada periodo del

interferograma, se puede obtener la diferencia entre las pérdidas y la diferencia entre los índices de grupo de ambas guías empleado las siguientes relaciones:

$$\Delta n_{\text{group}} = \frac{\lambda_{\max}\lambda_{\min}}{2L_{\text{arm}}(\lambda_{\max}-\lambda_{\min})} = n_{\text{group}}^{\text{wire}} - n_{\text{group}}^{\text{SWG}} \tag{B.7}$$

$$\Delta\alpha = \frac{1}{L_{\text{arm}}[\text{cm}]}\left[20\log\left(\frac{10^{R/20}+1}{10^{R/20}-1}\right)\right] \quad [\text{dB/cm}] = \alpha^{\text{wire}} - (\alpha^{\text{SWG}} + \alpha^{\text{tapers}}) \tag{B.8}$$

Como se puede observar en dichas expresiones, para obtener las pérdidas por leakage y el índice de grupo de la guía SWG, es necesario obtener la misma información de las guías de silicio. El índice de grupo de las guías de silicio se puede estimar a partir de resolutores modales vectoriales. Para el caso que nos ocupa, el valor estimado es de 4.2, manteniéndose constante en el rango de longitudes de onda considerado. La diferencia de pérdidas proviene de las perdidas por leakage y las pérdidas ocasionadas en los tapers, cuyo valor se estima de 0.7 dB. Así, dado que en el brazo que contiene la Si-wire no se introdujeron tapers, es necesario restar este valor de las pérdidas calculadas, podemos obtener las pérdidas por leakage. El resultado de estas medidas se encuentra en la figura B.17 b). Como se puede observar, esta figura corrobora los resultados obtenidos de forma numérica, comprobándose que existe una relación exponencial entre las pérdidas por leakage y el índice efectivo, y que además esta relación es independiente de los parámetros geométricos que definen la guía.

C
Curriculum Vitae

Work experience and research

I started research in June 2013, while carrying out my master thesis at Málaga University as a research assistant. Since November 2013 I am working towards my Ph.D. in polarization management and coherent receivers at Málaga University, under the supervision of Dr. Robert Halir and Dr. Alejandro Ortega-Moñux. These are my main research activities:

SOI Integrated Polarization Controller

Together with the research group, and the collaboration of the Université Paris-Sud, we have developed a world-record polarization controller, achieving 40 dB in polarization extinction ratio range. I carried out the design and the characterization of the device.

MUCORE

As a part of the research group, I am actively involved in the MUltiport COherent REceivers (MUCORE) project, which is funded by the Spanish Ministry of Science. In this scope I have accomplished the design of a dual-polarization monolithically integrated coherent receiver, whose main novelty is that polarization diversity is implemented avoiding the use of both polarization splitter and rotators. I have also performed the characterization of coherent receivers based on the 2x3 architecture.

Leakage Losses in sub-wavelength waveguides

With the collaboration of the National Research Council of Canada, and the Commissariat à l'énergie atomique (CEA-Leti), from France, I have analysed the impact of the leakage losses in SWG waveguides.

Education

2008–2013	MSc in Telecommunications Engineering (communications option) at Málaga University.
2013–2014	MSc in Telematics and Telecomunication Networks at Málaga University.

Stays in foreign centers

June 2016-October 2016

Stay at Photonics Research Group, Ghent University, Belgium. During this stay I worked on the design of polarization rotator for midIR applications and the characterization of a SOI coherent receiver for Radio-over-Fiber applications, under the supervision of professor Gunther Roelkens.

International Journal Papers

[1] J. D. Sarmiento-Merenguel, R. Halir, X. Le Roux, C. Alonso-Ramos, L. Vivien, P. Cheben, E. Durán-Valdeiglesias, I. Molina-Fernández, D. Marris-Morini, D.-X. Xu, J. H. Schmid, S. Janz, and A. Ortega-Moñux, "Demonstration of integrated polarization control with a 40 dB range in polarization extinction ratio". Optica 2, 1019-1023 (2015).

[2] J. D. Sarmiento-Merenguel, A. Ortega-Moñux, J-M. Fédéli, J. G. Wangüemert-Pérez, C. Alonso-Ramos, E. Durán-Valdeiglesias, P. Cheben, I. Molina-Fernández, R. Halir, "Design guidelines for leakage losses in subwavelength grating waveguides". Optics Letters 41 (15), 3443-3446 (2016).

[3] R. Halir, P. Cheben, J.M. Luque-González, J. D. Sarmiento-Merenguel, J. H. Schmid, A. Ortega-Moñux, G. Wangüemert-Pérez, D.-X. Xu, S. Wang, I. Molina-Fernández, "Ultra-broadband nanophotonic beam- splitter using an anisotropic sub-wavelength metamaterial". Laser Photonics Rev. 10, 1039-1046 (2016).

International Conferences

[1] J. D. Sarmiento-Merenguel, C. Alonso-Ramos, R. Halir, L. Vivien, P. Cheben, A. Ortega-Moñux, I. Molina-Fernández, X. Leroux, D. Marris-Morini, D. X. Xu, J. H. Schmid, S. Janz, "Silicon-on-insulator polarization controller with relaxed fabrication tolerances," Group IV Photonics (GFP), 2014 IEEE 11th International Conference on, Paris, 2014.

[2] R. Halir, P. Reyes-Iglesias, C. Alonso-Ramos, J. D. Sarmiento-Merenguel, G. Wangüemert-Pérez, P. Cheben, I. Molina-Fernández, A. Ortega-Moñux, "Colorless devices and reception techniques for polarization multiplexed communications," Transparent Optical Networks (ICTON), 2015 17th International Conference on, Budapest, 2015.

[3] J.D. Sarmiento-Merenguel, C. Alonso-Ramos, R. Halir, X. Le Roux, L. Vivien, P. Cheben, E. Durán-Valdeiglesias, I. Molina-Fernández, D. Marris-Morini, Danxia Xu, J. H. Schmid, S. Janz, A. Ortega-Moñux, “Silicon-on-insulator integrated polarization controlller", SPIE Photonics Europe, Brussels 2016.

[4] J.D. Sarmiento-Merenguel, C. Alonso-Ramos, R. Halir, X. Le Roux, L. Vivien, P. Cheben, E. Durán-Valdeiglesias, I. Molina-Fernández, D. Marris-Morini, Danxia Xu, J. H. Schmid, S. Janz, A. Ortega-Moñux, “Integrated polarization controller with 40 dB polarization extinction ratio range in the C-Band", in European Conference on Integrated Optics, Varsaw 2016.

[5] J. D. Sarmiento-Merenguel, A. Ortega-Moñux, J-M. Fédéli, J. G. Wangüemert-Pérez, C. Alonso-Ramos, E. Durán-Valdeiglesias, P. Cheben, I. Molina-Fernández, R. Halir, “On leakage losses in subwavelength grating devices", in International Conference on Metamaterials, Photonic Crystals and Plasmonics, M?laga 2016.

[6] C. Alonso-Ramos, J.D. Sarmiento-Merenguel, R. Halir, X. Le Roux, L. Vivien, P. Cheben, E. Durán-Valdeiglesias, I. Molina-Fernández, D. Marris-Morini, D.-X. Xu, J.H. Schmid, S. Janz, A. Ortega-Moñux, “Integrated Polarization Controllers", 2016 Progress in Electromagnetic Research Symposium (PIERS), Shanghai, 2016.

[7] P. Cheben, J. H. Schmid, D. X. Xu, S. Janz, J. Lapointe, M. Rahim, S. Wang, M. Vachon, R. Halir, A. Ortega-Moñux, J. D. Sarmiento-Merenguel, G. Wangüemert-Pérez, I. Molina-Fernández, J. Pond, D. Benedikovic, C. Alonso-Ramos, X. Le Roux, L. Vivien, D. Marris-Morini, J. S. Penadés, M. Nedeljkovic, G. Z. Mashanovich, A. V. Velasco, M. L. Calvo, M. Dado, J. Müllerová, W. Ye, M. Pápeš, V. Vašinek, “Subwavelength structures for nanophotonic couplers, colourless splitters, polarization control and mid-infrared waveguides," 2016 18th International Conference on Transparent Optical Networks (ICTON), Trento, Italy, 2016.

[8] J.D. Sarmiento-Merenguel, J. Verbist, K. Van Gasse, J. Zhang, B. Moeneclaey, J. Bauwelinck, X. Yin, R. Halir, A. Ortega-Moñux, I. Molina-Fernández, G. Roelkens, “Demonstration of Silicon-On-Insulator Coherent receiver for Radio-Over-Fiber applications," in European Conference on Integrated Optics, Eindhoven 2017.

Bibliography

[1] S. R. James, R. W. Dennell, A. S. Gilbert, H. T. Lewis, J. A. J. Gowlett, T. F. Lynch, W. C. McGrew, C. R. Peters, G. G. Pope, A. B. Stahl, and S. R. James, "Hominid use of fire in the lower and middle pleistocene: A review of the evidence [and comments and replies]," *Current Anthropology*, vol. 30, no. 1, pp. 1–26, 1989. [Online]. Available: http://dx.doi.org/10.1086/203705

[2] T. Maiman, "Stimulated optical radiation in ruby masers," *Nature*, vol. 187, pp. 493–494, 1960.

[3] S. E. Miller, "Integrated Optics: An Introduction," *Bell System Technical Journal*, vol. 48, no. 7, pp. 2059–2069, 1969. [Online]. Available: http://dx.doi.org/10.1002/j.1538-7305.1969.tb01165.x

[4] E. Agrell, M. Karlsson, A. R. Chraplyvy, D. J. Richardson, P. M. Krummrich, P. Winzer, K. Roberts, J. K. Fischer, S. J. Savory, B. J. Eggleton, M. Secondini, F. R. Kschischang, A. Lord, J. Prat, I. Tomkos, J. E. Bowers, S. Srinivasan, M. Brandt-Pearce, and N. Gisin, "Roadmap of optical communications," *Journal of Optics*, vol. 18, no. 6, p. 063002, 2016. [Online]. Available: http://stacks.iop.org/2040-8986/18/i=6/a=063002

[5] C. V. N. Index, "The zettabyte era–trends and analysis," *Cisco white paper*, 2016.

[6] T. Li, "Advances in optical fiber communications: An historical perspective," *IEEE Journal on Selected Areas in Communications*, vol. 1, no. 3, pp. 356–372, April 1983.

[7] "AC400 flex product family," Acacia Communications Inc., Tech. Rep. [Online]. Available: http://acacia-inc.com/products/ac400-flex-product-family/

[8] D. Che, Q. Hu, and W. Shieh, "Linearization of direct detection optical channels using self-coherent subsystems," *Journal of Lightwave Technology*, vol. 34, no. 2, pp. 516–524, Jan 2016.

[9] E. Ip, A. P. T. Lau, D. J. F. Barros, and J. M. Kahn, "Coherent detection in optical fiber systems," *Opt. Express*, vol. 16, no. 2, pp. 753–791, Jan 2008. [Online]. Available: http://www.opticsexpress.org/abstract.cfm?URI=oe-16-2-753

[10] B. Koch, R. Noé, V. Mirvoda, D. Sandel, V. Filsinger, and K. Puntsri, "40-krad/s polarization tracking in 200-gb/s pdm-rz-dqpsk transmission over 430 km," *IEEE Photonics Technology Letters*, vol. 22, no. 9, p. 613, 2010.

[11] R. Halir, P. J. Bock, P. Cheben, A. Ortega-Moñux, C. Alonso-Ramos, J. H. Schmid, J. Lapointe, D.-X. Xu, J. G. Wangüemert-Pérez, Í. Molina-Fernández, and S. Janz, "Waveguide sub-wavelength structures: a review of principles and applications," *Laser & Photonics Reviews*, vol. 9, no. 1, pp. 25–49, 2015. [Online]. Available: http://dx.doi.org/10.1002/lpor.201400083

[12] R. Halir, P. Cheben, J. M. Luque-González, J. D. Sarmiento-Merenguel, J. H. Schmid, G. Wangüemert-Pérez, D.-X. Xu, S. Wang, A. Ortega-Moñux, and Í. Molina-Fernández, "Ultra-broadband nanophotonic beamsplitter using an anisotropic sub-wavelength metamaterial," *Laser & Photonics Reviews*, vol. 10, no. 6, pp. 1039–1046, 2016. [Online]. Available: http://dx.doi.org/10.1002/lpor.201600213

[13] D. Dai, L. Liu, S. Gao, D.-X. Xu, and S. He, "Polarization management for silicon photonic integrated circuits," *Laser & Photonics Reviews*, vol. 7, no. 3, pp. 303–328, 2012.

[14] M. Pircher, C. K. Hitzenberger, and U. Schmidt-Erfurth, "Polarization sensitive optical coherence tomography in the human eye," *Progress in Retinal and Eye Research*, vol. 30, no. 6, pp. 431 – 451, 2011. [Online]. Available: http://www.sciencedirect.com/science/article/pii/S1350946211000395

[15] P. Sibson, J. E. Kennard, S. Stanisic, C. Erven, J. L. O'Brien, and M. G. Thompson, "Integrated silicon photonics for high-speed quantum key distribution," *Optica*, vol. 4, no. 2, pp. 172–177, Feb 2017. [Online]. Available: http://www.osapublishing.org/optica/abstract.cfm?URI=optica-4-2-172

[16] R. C. Alferness and L. L. Buhl, "Electro-optic waveguide te-tm mode converter with low drive voltage," *Opt. Lett.*, vol. 5, no. 11, pp. 473–475, Nov 1980. [Online]. Available: http://ol.osa.org/abstract.cfm?URI=ol-5-11-473

[17] J. D. Sarmiento-Merenguel, R. Halir, X. L. Roux, C. Alonso-Ramos, L. Vivien, P. Cheben, E. Durán-Valdeiglesias, Í. Molina-Fernández, D. Marris-Morini, D.-X. Xu, J. H. Schmid, S. Janz, and A. Ortega-Moñux, "Demonstration of integrated polarization control with a 40 dB range in extinction ratio," *Optica*, vol. 2, no. 12, pp. 1019–1023, Dec 2015. [Online]. Available: http://www.osapublishing.org/optica/abstract.cfm?URI=optica-2-12-1019

[18] R. J. Deri, E. C. M. Pennings, A. Scherer, A. S. Gozdz, C. Caneau, N. C. Andreadakis, V. Shah, L. Curtis, R. J. Hawkins, J. B. D. Soole, and J. I. Song, "Ultra-compact monolithic integration of balanced, polarization diversity photodetectors for coherent lightwave receivers," *IEEE Photonics Technology Letters*, vol. 4, no. 11, pp. 1238–1240, Nov 1992.

[19] "Acacia communications introduces cfp2-aco module based on its silicon pic," Acacia Communications Inc., techreport, Mar. 2016. [Online]. Available: http://ir.acacia-inc.com/phoenix.zhtml?c=254242&p=irol-newsArticle_print&ID=2164394

[20] OIF, "Implementation agreement for integrated dual polarization micro-intradyne coherent receivers," OIF, Tech. Rep., 2015. [Online]. Available: http://www.oiforum.com/wp-content/uploads/OIF-DPC-MRX-01.0-IA.pdf

[21] C. Alonso-Ramos, P. J. Reyes-Iglesias, A. Ortega-Moñux, D. Pérez-Galacho, R. Halir, and Í. Molina-Fernández, "Polarization-beam-splitter-less integrated

dual-polarization coherent receiver," *Opt. Lett.*, vol. 39, no. 15, pp. 4400–4403, Aug 2014. [Online]. Available: http://ol.osa.org/abstract.cfm?URI=ol-39-15-4400

[22] M. W. Farn, "Binary gratings with increased efficiency," *Appl. Opt.*, vol. 31, no. 22, pp. 4453–4458, Aug 1992. [Online]. Available: http://ao.osa.org/abstract.cfm?URI=ao-31-22-4453

[23] C. A. Alonso-Ramos, "Photonic chip interconnects and integrated polarization management for coherent communication," Ph.D. dissertation, Universidad de Málaga, 2014.

[24] D. Benedikovic, C. Alonso-Ramos, P. Cheben, J. H. Schmid, S. Wang, R. Halir, A. Ortega-Moñux, D.-X. Xu, L. Vivien, J. Lapointe, S. Janz, and M. Dado, "Single-etch subwavelength engineered fiber-chip grating couplers for 1.3 μm datacom wavelength band," *Opt. Express*, vol. 24, no. 12, pp. 12 893–12 904, Jun 2016. [Online]. Available: http://www.opticsexpress.org/abstract.cfm?URI=oe-24-12-12893

[25] D. Benedikovic, P. Cheben, J. H. Schmid, D.-X. Xu, B. Lamontagne, S. Wang, J. Lapointe, R. Halir, A. Ortega-Moñux, S. Janz, and M. Dado, "Subwavelength index engineered surface grating coupler with sub-decibel efficiency for 220-nm silicon-on-insulator waveguides," *Opt. Express*, vol. 23, no. 17, pp. 22 628–22 635, Aug 2015. [Online]. Available: http://www.opticsexpress.org/abstract.cfm?URI=oe-23-17-22628

[26] P. Cheben, J. H. Schmid, S. Wang, D.-X. Xu, M. Vachon, S. Janz, J. Lapointe, Y. Painchaud, and M.-J. Picard, "Broadband polarization independent nanophotonic coupler for silicon waveguides with ultra-high efficiency," *Opt. Express*, vol. 23, no. 17, pp. 22 553–22 563, Aug 2015. [Online]. Available: http://www.opticsexpress.org/abstract.cfm?URI=oe-23-17-22553

[27] B. E. Saleh, M. C. Teich, and B. E. Saleh, *Fundamentals of photonics*. Wiley New York, 1991, vol. 22.

[28] R. C. Jones, "A new calculus for the treatment of optical systems I. Description and discussion of the calculus," *J. Opt. Soc. Am.*, vol. 31, no. 7, pp. 488–493, Jul 1941. [Online]. Available: http://www.osapublishing.org/abstract.cfm?URI=josa-31-7-488

[29] D. H. Goldstein, *Polarized light*. CRC press, 2016.

[30] G. G. Stokes, "On the change of refrangibility of light," *Philosophical Transactions of the Royal Society of London*, vol. 142, pp. 463–562, 1852.

[31] C.-L. Chen, *Foundations for guided-wave optics, section 5.3*. John Wiley & Sons, 2006.

[32] C. Alonso-Ramos, S. Romero-García, A. Ortega-Moñux, Í. Molina-Fernández, R. Zhang, H. Bach, and M. Schell, "Polarization rotator for InP rib waveguide," *Opt. Lett.*, vol. 37, no. 3, pp. 335–337, 2012.

[33] L. Liu, Y. Ding, K. Yvind, and J. M. Hvam, "Silicon-on-insulator polarization splitting and rotating device for polarization diversity circuits," *Opt. Express*, vol. 19, no. 13, pp. 12 646–12 651, Jun 2011. [Online]. Available: http://www.opticsexpress.org/abstract.cfm?URI=oe-19-13-12646

[34] T. Kawazoe, K. Satoh, I. Hayashi, and H. Mori, "Fabrication of integrated-optic polarization controller using Z-propagating Ti-LiNbO3 waveguides," *Journal of Lightwave Technology*, vol. 10, no. 1, pp. 51–56, Jan 1992.

[35] F. Heismann, M. Divino, and L. Buhl, "Integrated-optic polarization controller with unlimited transformation range," *Applied physics letters*, vol. 57, no. 9, pp. 855–857, 1990.

[36] S. H. Rumbaugh, M. D. Jones, and L. W. Casperson, "Polarization control for coherent fiber-optic systems using nematic liquid crystals," *Journal of Lightwave Technology*, vol. 8, no. 3, pp. 459–465, Mar 1990.

[37] K. Suzuki, Y. Kawabata, T. Tanemura, and Y. Nakano, "Design and experimental investigation of monolithic polarization controller with InGaAlAs/inAlAs multiple quantum wells," in *2015 International Conference on Photonics in Switching (PS)*, Sept 2015, pp. 226–228.

[38] S.-H. Park, J.-W. Kim, M.-C. Oh, Y.-O. Noh, and H.-J. Lee, "Polymer waveguide birefringence modulators," *IEEE Photonics Technology Letters*, vol. 24, no. 10, pp. 845–847, 2012.

[39] C. Alonso-Ramos, R. Halir, A. Ortega-Moñux, P. Cheben, L. Vivien, Í. Molina-Fernández, D. Marris-Morini, S. Janz, D.-X. Xu, and J. Schmid, "Highly tolerant tunable waveguide polarization rotator scheme," *Opt. Lett.*, vol. 37, no. 17, pp. 3534–3536, Sep 2012. [Online]. Available: http://ol.osa.org/abstract.cfm?URI=ol-37-17-3534

[40] T. Barwicz, M. Watts, M. Popovic, P. Rakich, L. Socci, F. Kärtner, E. Ippen, and H. Smith, "Polarization-transparent microphotonic devices in the strong confinement limit," *Nat. Photonics*, vol. 1, no. 1, pp. 57–60, 2007.

[41] M. R. Watts and H. A. Haus, "Integrated mode-evolution-based polarization rotators," *Opt. Lett.*, vol. 30, no. 2, pp. 138–140, Jan 2005. [Online]. Available: http://ol.osa.org/abstract.cfm?URI=ol-30-2-138

[42] J. Zhang, T.-Y. Liow, M. Yu, G.-Q. Lo, and D.-L. Kwong, "Silicon waveguide based TE mode converter," *Opt. Express*, vol. 18, no. 24, pp. 25 264–25 270, Nov 2010. [Online]. Available: http://www.opticsexpress.org/abstract.cfm?URI=oe-18-24-25264

[43] L. Chen, C. R. Doerr, and Y.-K. Chen, "Compact polarization rotator on silicon for polarization-diversified circuits," *Opt. Lett.*, vol. 36, no. 4, pp. 469–471, Feb 2011. [Online]. Available: http://ol.osa.org/abstract.cfm?URI=ol-36-4-469

[44] H. Zhang, S. Das, J. Zhang, Y. Huang, C. Li, S. Chen, H. Zhou, M. Yu, P. Guo-Qiang Lo, and J. T. Thong, "Efficient and broadband polarization rotator using horizontal slot waveguide for silicon photonics," *Applied physics letters*, vol. 101, no. 2, p. 021105, 2012.

[45] G. Chen, L. Chen, W. Ding, F. Sun, and R. Feng, "Ultra-short Silicon-On-Insulator (SOI) polarization rotator between a slot and a strip waveguide based on a nonlinear raised cosine flat-tip taper," *Opt. Express*, vol. 21, no. 12, pp. 14 888–14 894, Jun 2013. [Online]. Available: http://www.opticsexpress.org/abstract.cfm?URI=oe-21-12-14888

[46] Y. Xiong, D. X. Xu, J. H. Schmid, P. Cheben, S. Janz, and W. N. Ye, "Robust silicon waveguide polarization rotator with an amorphous silicon overlayer," *IEEE Photonics Journal*, vol. 6, no. 2, pp. 1–8, April 2014.

[47] K. Goi, A. Oka, H. Kusaka, K. Ogawa, T.-Y. Liow, X. Tu, G.-Q. Lo, and D.-L. Kwong, "Low-loss partial rib polarization rotator consisting only of silicon core and silica cladding," *Opt. Lett.*, vol. 40, no. 7, pp. 1410–1413, Apr 2015. [Online]. Available: http://ol.osa.org/abstract.cfm?URI=ol-40-7-1410

[48] L. Liu, Y. Ding, K. Yvind, and J. M. Hvam, "Efficient and compact TE–TM polarization converter built on silicon-on-insulator platform with a simple fabrication process," *Opt. Lett.*, vol. 36, no. 7, pp. 1059–1061, Apr 2011. [Online]. Available: http://ol.osa.org/abstract.cfm?URI=ol-36-7-1059

[49] K. Mertens, B. Scholl, and H. J. Schmitt, "New highly efficient polarization converters based on hybrid supermodes," *Journal of Lightwave Technology*, vol. 13, no. 10, pp. 2087–2092, Oct 1995.

[50] Y. Xiong, J. G. Wangüemert-Pérez, D.-X. Xu, J. H. Schmid, P. Cheben, and W. N. Ye, "Polarization splitter and rotator with subwavelength grating for enhanced fabrication tolerance," *Opt. Lett.*, vol. 39, no. 24, pp. 6931–6934, Dec 2014. [Online]. Available: http://ol.osa.org/abstract.cfm?URI=ol-39-24-6931

[51] Y. Xu and J. Xiao, "Ultracompact and high efficient silicon-based polarization splitter-rotator using a partially-etched subwavelength grating coupler," *Scientific Reports*, vol. 6, p. 27949, 2016.

[52] Y. Ding, L. Liu, C. Peucheret, and H. Ou, "Fabrication tolerant polarization splitter and rotator based on a tapered directional coupler," *Opt. Express*, vol. 20, no. 18, pp. 20 021–20 027, Aug 2012. [Online]. Available: http://www.opticsexpress.org/abstract.cfm?URI=oe-20-18-20021

[53] Y. Fei, L. Zhang, T. Cao, Y. Cao, and S. Chen, "Ultracompact polarization splitter–rotator based on an asymmetric directional coupler," *Appl. Opt.*, vol. 51, no. 34, pp. 8257–8261, Dec 2012. [Online]. Available: http://ao.osa.org/abstract.cfm?URI=ao-51-34-8257

[54] H. Guan, A. Novack, M. Streshinsky, R. Shi, Q. Fang, A. E.-J. Lim, G.-Q. Lo, T. Baehr-Jones, and M. Hochberg, "CMOS-compatible highly efficient

polarization splitter and rotator based on a double-etched directional coupler," *Opt. Express*, vol. 22, no. 3, pp. 2489–2496, Feb 2014. [Online]. Available: http://www.opticsexpress.org/abstract.cfm?URI=oe-22-3-2489

[55] Y. Xiong, D.-X. Xu, J. H. Schmid, P. Cheben, S. Janz, and W. N. Ye, "Fabrication tolerant and broadband polarization splitter and rotator based on a taper-etched directional coupler," *Opt. Express*, vol. 22, no. 14, pp. 17 458–17 465, Jul 2014. [Online]. Available: http://www.opticsexpress.org/abstract.cfm?URI=oe-22-14-17458

[56] L. Socci, V. Sorianello, and M. Romagnoli, "300 nm bandwidth adiabatic SOI polarization splitter-rotators exploiting continuous symmetry breaking," *Opt. Express*, vol. 23, no. 15, pp. 19 261–19 271, Jul 2015. [Online]. Available: http://www.opticsexpress.org/abstract.cfm?URI=oe-23-15-19261

[57] M. Yin, Q. Deng, Y. Li, X. Wang, and H. Li, "Ultrashort and low-loss polarization rotators utilizing hybrid plasmonic-dielectric couplers," *IEEE Photonics Technology Letters*, vol. 27, no. 3, pp. 229–232, Feb 2015.

[58] Y. Wang, M. Ma, H. Yun, Z. Lu, X. Wang, N. A. F. Jaeger, and L. Chrostowski, "Ultra-compact sub-wavelength grating polarization splitter-rotator for silicon-on-insulator platform," *IEEE Photonics Journal*, vol. 8, no. 6, pp. 1–9, Dec 2016.

[59] Y. Xu and J. Xiao, "Design of a compact and integrated TM-rotated/TE-through polarization beam splitter for silicon-based slot waveguides," *Appl. Opt.*, vol. 55, no. 3, pp. 611–618, Jan 2016. [Online]. Available: http://ao.osa.org/abstract.cfm?URI=ao-55-3-611

[60] X. Sun, M. Z. Alam, J. S. Aitchison, and M. Mojahedi, "Polarization rotator based on augmented low-index-guiding waveguide on silicon nitride/silicon-on-insulator platform," *Opt. Lett.*, vol. 41, no. 14, pp. 3229–3232, Jul 2016. [Online]. Available: http://ol.osa.org/abstract.cfm?URI=ol-41-14-3229

[61] K. Tan, Y. Huang, G.-Q. Lo, C. Lee, and C. Yu, "Compact highly-efficient polarization splitter and rotator based on 90° bends," *Opt. Express*, vol. 24, no. 13, pp. 14 506–14 512, Jun 2016. [Online]. Available: http://www.opticsexpress.org/abstract.cfm?URI=oe-24-13-14506

[62] Y. Zhang, Y. He, X. Jiang, B. Liu, C. Qiu, Y. Su, and R. A. Soref, "Ultra-compact and highly efficient silicon polarization splitter and rotator," *APL Photonics*, vol. 1, no. 9, p. 091304, 2016.

[63] K. Tan, Y. Huang, G.-Q. Lo, C. Yu, and C. Lee, "Experimental realization of an O-band compact polarization splitter and rotator," *Opt. Express*, vol. 25, no. 4, pp. 3234–3241, Feb 2017. [Online]. Available: http://www.opticsexpress.org/abstract.cfm?URI=oe-25-4-3234

[64] D. Dai and J. E. Bowers, "Novel concept for ultracompact polarization splitter-rotator based on silicon nanowires," *Opt. Express*, vol. 19, no. 11, pp.

10 940–10 949, May 2011. [Online]. Available: http://www.opticsexpress.org/abstract.cfm?URI=oe-19-11-10940

[65] H. Xu and Y. Shi, "Ultra-compact and highly efficient polarization rotator utilizing multi-mode waveguides," *Opt. Lett.*, vol. 42, no. 4, pp. 771–774, Feb 2017. [Online]. Available: http://ol.osa.org/abstract.cfm?URI=ol-42-4-771

[66] W. Yuan, K. Kojima, B. Wang, T. Koike-Akino, K. Parsons, S. Nishikawa, and E. Yagyu, "Mode-evolution-based polarization rotator-splitter design via simple fabrication process," *Opt. Express*, vol. 20, no. 9, pp. 10 163–10 169, Apr 2012. [Online]. Available: http://www.opticsexpress.org/abstract.cfm?URI=oe-20-9-10163

[67] Y. Ding, H. Ou, and C. Peucheret, "Wideband polarization splitter and rotator with large fabrication tolerance and simple fabrication process," *Opt. Lett.*, vol. 38, no. 8, pp. 1227–1229, Apr 2013. [Online]. Available: http://ol.osa.org/abstract.cfm?URI=ol-38-8-1227

[68] H. Guan, Y. Ma, R. Shi, A. Novack, J. Tao, Q. Fang, A. E.-J. Lim, G.-Q. Lo, T. Baehr-Jones, and M. Hochberg, "Ultracompact silicon-on-insulator polarization rotator for polarization-diversified circuits," *Opt. Lett.*, vol. 39, no. 16, pp. 4703–4706, Aug 2014. [Online]. Available: http://ol.osa.org/abstract.cfm?URI=ol-39-16-4703

[69] W. D. Sacher, T. Barwicz, B. J. F. Taylor, and J. K. S. Poon, "Polarization rotator-splitters in standard active silicon photonics platforms," *Opt. Express*, vol. 22, no. 4, pp. 3777–3786, Feb 2014. [Online]. Available: http://www.opticsexpress.org/abstract.cfm?URI=oe-22-4-3777

[70] W. D. Sacher, Y. Huang, L. Ding, T. Barwicz, J. C. Mikkelsen, B. J. F. Taylor, G.-Q. Lo, and J. K. S. Poon, "Polarization rotator-splitters and controllers in a si3n4-on-soi integrated photonics platform," *Opt. Express*, vol. 22, no. 9, pp. 11 167–11 174, May 2014. [Online]. Available: http://www.opticsexpress.org/abstract.cfm?URI=oe-22-9-11167

[71] J. Wang, M. Qi, Y. Xuan, H. Huang, Y. Li, M. Li, X. Chen, Q. Jia, Z. Sheng, A. Wu, W. Li, X. Wang, S. Zou, and F. Gan, "Proposal for fabrication-tolerant SOI polarization splitter-rotator based on cascaded MMI couplers and an assisted bi-level taper," *Opt. Express*, vol. 22, no. 23, pp. 27 869–27 879, Nov 2014. [Online]. Available: http://www.opticsexpress.org/abstract.cfm?URI=oe-22-23-27869

[72] J. Wang, J. Xiao, and X. Sun, "Design of a broadband polarization rotator for silicon-based cross-slot waveguides," *Appl. Opt.*, vol. 54, no. 12, pp. 3805–3810, Apr 2015. [Online]. Available: http://ao.osa.org/abstract.cfm?URI=ao-54-12-3805

[73] Y. Yin, Z. Y. Li, and D. Dai, "Ultra-broadband polarization splitter-rotator based on the mode evolution in a dual-core adiabatic taper," *Journal of Lightwave Technology*, vol. PP, no. 99, pp. 1–1, 2017.

[74] X. Tu, M. Li, J. Xing, H. Fu, and D. Geng, "Compact PSR based on an asymmetric bi-level lateral taper in an adiabatic directional coupler," *J. Lightwave Technol.*, vol. 34, no. 3, pp. 985–991, Feb 2016. [Online]. Available: http://jlt.osa.org/abstract.cfm?URI=jlt-34-3-985

[75] D. Dai and H. Wu, "Realization of a compact polarization splitter-rotator on silicon," *Opt. Lett.*, vol. 41, no. 10, pp. 2346–2349, May 2016. [Online]. Available: http://ol.osa.org/abstract.cfm?URI=ol-41-10-2346

[76] V. P. Tzolov and M. Fontaine, "A passive polarization converter free of longitudinally-periodic structure," *Optics Communications*, vol. 127, no. 1-3, pp. 7–13, 1996.

[77] Z. Wang and D. Dai, "Ultrasmall Si-nanowire-based polarization rotator," *J. Opt. Soc. Am. B*, vol. 25, no. 5, pp. 747–753, May 2008. [Online]. Available: http://josab.osa.org/abstract.cfm?URI=josab-25-5-747

[78] B. M. Holmes and D. C. Hutchings, "Realization of novel low-loss monolithically integrated passive waveguide mode converters," *IEEE Photonics Technology Letters*, vol. 18, no. 1, pp. 43–45, Jan 2006.

[79] V. P. Tzolov and M. Fontaine, "A passive polarization converter free of longitudinally-periodic structure," *Optics Communications*, vol. 127, no. 1, pp. 7 – 13, 1996. [Online]. Available: http://www.sciencedirect.com/science/article/pii/0030401896000399

[80] C. van Dam, L. H. Spiekman, F. P. G. M. van Ham, F. H. Groen, J. J. G. M. van der Tol, I. Moerman, W. W. Pascher, M. Hamacher, H. Heidrich, C. M. Weinert, and M. K. Smit, "Novel compact polarization converters based on ultra short bends," *IEEE Photonics Technology Letters*, vol. 8, no. 10, pp. 1346–1348, Oct 1996.

[81] Z. Huan, R. Scarmozzino, G. Nagy, J. Steel, and R. M. Osgood, "Realization of a compact and single-mode optical passive polarization converter," *IEEE Photonics Technology Letters*, vol. 12, no. 3, pp. 317–319, March 2000.

[82] B. M. A. Rahman, S. S. A. Obayya, N. Somasiri, M. Rajarajan, K. T. V. Grattan, and H. A. El-Mikathi, "Design and characterization of compact single-section passive polarization rotator," *Journal of Lightwave Technology*, vol. 19, no. 4, pp. 512–519, Apr 2001.

[83] M. Kotlyar, L. Bolla, M. Midrio, L. O'Faolain, and T. Krauss, "Compact polarization converter in InP-based material," *Opt. Express*, vol. 13, no. 13, pp. 5040–5045, 2005.

[84] L. M. Augustin, R. Hanfoug, J. J. G. M. van der Tol, W. J. M. de Laat, and M. K. Smit, "A compact integrated polarization splitter/converter in InGaAsP-InP," *IEEE Photonics Technology Letters*, vol. 19, no. 17, pp. 1286–1288, Sept 2007.

[85] H. Fukuda, K. Yamada, T. Tsuchizawa, T. Watanabe, H. Shinojima, and S. ichi Itabashi, "Polarization rotator based on silicon wire waveguides," *Opt. Express*, vol. 16, no. 4, pp. 2628–2635, Feb 2008. [Online]. Available: http://www.opticsexpress.org/abstract.cfm?URI=oe-16-4-2628

[86] J. J. Bregenzer, S. McMaster, M. Sorel, B. M. Holmes, and D. C. Hutchings, "Compact polarization mode converter monolithically integrated within a semiconductor laser," *J. Lightwave Technol.*, vol. 27, no. 14, pp. 2732–2736, Jul 2009. [Online]. Available: http://jlt.osa.org/abstract.cfm?URI=jlt-27-14-2732

[87] S.-H. Kim, R. Takei, Y. Shoji, and T. Mizumoto, "Single-trench waveguide TE-TM mode converter," *Opt. Express*, vol. 17, no. 14, pp. 11 267–11 273, Jul 2009. [Online]. Available: http://www.opticsexpress.org/abstract.cfm?URI=oe-17-14-11267

[88] A. V. Velasco, M. L. Calvo, P. Cheben, A. Ortega-Moñux, J. H. Schmid, C. A. Ramos, Í. M. Fernández, J. Lapointe, M. Vachon, S. Janz, and D.-X. Xu, "Ultracompact polarization converter with a dual subwavelength trench built in a silicon-on-insulator waveguide," *Opt. Lett.*, vol. 37, no. 3, pp. 365–367, Feb 2012. [Online]. Available: http://ol.osa.org/abstract.cfm?URI=ol-37-3-365

[89] D. Vermeulen, S. Selvaraja, P. Verheyen, P. Absil, W. Bogaerts, D. V. Thourhout, and G. Roelkens, "Silicon-on-insulator polarization rotator based on a symmetry breaking silicon overlay," *IEEE Photonics Technology Letters*, vol. 24, no. 6, pp. 482–484, March 2012.

[90] J. N. Caspers, M. Z. Alam, and M. Mojahedi, "Compact hybrid plasmonic polarization rotator," *Opt. Lett.*, vol. 37, no. 22, pp. 4615–4617, Nov 2012. [Online]. Available: http://ol.osa.org/abstract.cfm?URI=ol-37-22-4615

[91] M. Aamer, A. M. Gutierrez, A. Brimont, D. Vermeulen, G. Roelkens, J. M. Fedeli, A. Hakansson, and P. Sanchis, "CMOS compatible Silicon-on-Insulator polarization rotator based on symmetry breaking of the waveguide cross section," *IEEE Photonics Technology Letters*, vol. 24, no. 22, pp. 2031–2034, Nov 2012.

[92] M. Zaitsu, T. Tanemura, A. Higo, and Y. Nakano, "Experimental demonstration of self-aligned InP/InGaAsP polarization converter for polarization multiplexed photonic integrated circuits," *Opt. Express*, vol. 21, no. 6, pp. 6910–6918, Mar 2013. [Online]. Available: http://www.opticsexpress.org/abstract.cfm?URI=oe-21-6-6910

[93] L. Jia, T. Y. Liow, J. Song, X. Luo, N. Duan, S. C. Koh, Q. Fang, M. Yu, and G. Lo, "Compact optical polarization rotators based on an asymmetric silicon waveguide," *IEEE Photonics Technology Letters*, vol. 25, no. 22, pp. 2229–2232, Nov 2013.

[94] T. Cao, S. Chen, Y. Fei, L. Zhang, and Q.-Y. Xu, "Ultra-compact and fabrication-tolerant polarization rotator based on a bend asymmetric-slab waveguide," *Appl. Opt.*, vol. 52, no. 5, pp. 990–996, Feb 2013. [Online]. Available: http://ao.osa.org/abstract.cfm?URI=ao-52-5-990

[95] L. Gao, Y. Huo, J. S. Harris, and Z. Zhou, "Ultra-compact and low-loss polarization rotator based on asymmetric hybrid plasmonic waveguide," *IEEE Photonics Technology Letters*, vol. 25, no. 21, pp. 2081–2084, Nov 2013.

[96] Y. Xu, J. Xiao, and X. Sun, "A compact polarization converter for silicon-based slot waveguides using a hybrid plasmonic effect," *Journal of Optics*, vol. 16, no. 8, p. 085502, 2014. [Online]. Available: http://stacks.iop.org/2040-8986/16/i=8/a=085502

[97] L. Jin, Q. Chen, and L. Wen, "Mode-coupling polarization rotator based on plasmonic waveguide," *Opt. Lett.*, vol. 39, no. 9, pp. 2798–2801, May 2014. [Online]. Available: http://ol.osa.org/abstract.cfm?URI=ol-39-9-2798

[98] Y. Fei, L. Zhang, Y. Cao, X. Lei, and S. Chen, "A novel polarization rotator based on an asymmetric slot waveguide," *Optics Communications*, vol. 324, pp. 22 – 25, 2014. [Online]. Available: http://www.sciencedirect.com/science/article/pii/S0030401814002466

[99] H. Zhou, C. Li, A. L. Eujin, L. Jia, M. Yu, and G. Lo, "Ultra-compact and broadband si photonics polarization rotator by self-alignment process," *Opt. Express*, vol. 23, no. 5, pp. 6815–6821, Mar 2015. [Online]. Available: http://www.opticsexpress.org/abstract.cfm?URI=oe-23-5-6815

[100] A. Xie, L. Zhou, J. Chen, and X. Li, "Efficient silicon polarization rotator based on mode-hybridization in a double-stair waveguide," *Opt. Express*, vol. 23, no. 4, pp. 3960–3970, Feb 2015. [Online]. Available: http://www.opticsexpress.org/abstract.cfm?URI=oe-23-4-3960

[101] C.-W. Hsu, H.-Y. Lin, J.-Y. Chen, and Y.-C. Cheng, "Ultracompact polarization rotator in an asymmetric single dielectric loaded rib waveguide," *Appl. Opt.*, vol. 55, no. 6, pp. 1395–1400, Feb 2016. [Online]. Available: http://ao.osa.org/abstract.cfm?URI=ao-55-6-1395

[102] X. Wang and J. Dong, "Ultrashort polarization rotator based on cross-symmetry waveguide," *Optics Communications*, vol. 367, pp. 68 – 71, 2016. [Online]. Available: http://www.sciencedirect.com/science/article/pii/S0030401816300402

[103] Y. Kim, D. W. Kim, M.-H. Lee, M. H. Lee, D. E. Yoo, K. N. Kim, S. C. Jeon, and K. H. Kim, "Demonstration of integrated polarization rotator based on an asymmetric silicon waveguide with a trench," *Journal of Optics*, vol. 18, no. 9, p. 095801, 2016. [Online]. Available: http://stacks.iop.org/2040-8986/18/i=9/a=095801

[104] M. Baier, F. M. Soares, T. Gaertner, R. Weiser, M. Moehrle, N. Grote, and M. Schell, "Highly fabrication tolerant polarization converter for generic photonic integration technology," in *2016 Compound Semiconductor Week (CSW) [Includes 28th International Conference on Indium Phosphide Related Materials (IPRM) 43rd International Symposium on Compound Semiconductors (ISCS)*, June 2016, pp. 1–2.

[105] Y. Shani, R. Alferness, T. Koch, U. Koren, M. Oron, B. I. Miller, and M. G. Young, "Polarization rotation in asymmetric periodic loaded rib waveguides," *Applied Physics Letters*, vol. 59, no. 11, pp. 1278–1280, 1991. [Online]. Available: http://dx.doi.org/10.1063/1.105474

[106] H. Heidrich, P. Albrecht, M. Hamacher, H. P. Nolting, H. Schroeter-Janssen, and C. M. Weinert, "Passive mode converter with a periodically tilted InP/GaInAsP rib waveguide," *IEEE Photonics Technology Letters*, vol. 4, no. 1, pp. 34–36, Jan 1992.

[107] W. Huang and Z. M. Mao, "Polarization rotation in periodic loaded rib waveguides," *Journal of Lightwave Technology*, vol. 10, no. 12, pp. 1825–1831, Dec 1992.

[108] J. J. G. M. van der Tol, J. W. Pedersen, E. G. Metaal, F. Hakimzadeh, Y. S. Oei, F. H. Groen, and I. Moerman, "Realization of a short integrated optic passive polarization converter," *IEEE Photonics Technology Letters*, vol. 7, no. 8, pp. 893–895, Aug 1995.

[109] T. Lang, F. Bahnmuller, and P. Benech, "New passive polarization converter on glass substrate," *IEEE Photonics Technology Letters*, vol. 10, no. 9, pp. 1295–1297, Sept 1998.

[110] T. Koster and P. V. Lambeck, "Passive polarization converter in sion technology," *Journal of Lightwave Technology*, vol. 19, no. 6, pp. 876–883, Jun 2001.

[111] J. Pello, J. van der Tol, S. Keyvaninia, R. van Veldhoven, H. Ambrosius, G. Roelkens, and M. Smit, "High-efficiency ultrasmall polarization converter in InP membrane," *Opt. Lett.*, vol. 37, no. 17, pp. 3711–3713, Sep 2012. [Online]. Available: http://ol.osa.org/abstract.cfm?URI=ol-37-17-3711

[112] H. Yun, Z. Chen, Y. Wang, J. Fluekiger, M. Caverley, L. Chrostowski, and N. A. F. Jaeger, "Polarization-rotating, bragg-grating filters on silicon-on-insulator strip waveguides using asymmetric periodic corner corrugations," *Opt. Lett.*, vol. 40, no. 23, pp. 5578–5581, Dec 2015. [Online]. Available: http://ol.osa.org/abstract.cfm?URI=ol-40-23-5578

[113] Y. Sun, Y. Xiong, and W. N. Ye, "Compact SOI polarization rotator using asymmetric periodic loaded waveguides," *IEEE Photonics Journal*, vol. 8, no. 1, pp. 1–8, Feb 2016.

[114] K. Kikuchi, "Fundamentals of coherent optical fiber communications," *Journal of Lightwave Technology*, vol. 34, no. 1, pp. 157–179, Jan 2016.

[115] J. Capmany, J. Mora, I. Gasulla, J. Sancho, J. Lloret, and S. Sales, "Microwave photonic signal processing," *Journal of Lightwave Technology*, vol. 31, no. 4, pp. 571–586, Feb 2013.

[116] H. LeFevre, "Fiber optic polarization controller," Jun. 21 1983, US Patent 4,389,090. [Online]. Available: http://www.google.com/patents/US4389090

[117] F. Heismann and M. S. Whalen, "Broadband reset-free automatic polarisation controller," *Electronics Letters*, vol. 27, no. 4, pp. 377–379, Feb 1991.

[118] L. Moller, "WDM polarization controller in PLC technology," *IEEE Photonics Technology Letters*, vol. 13, no. 6, pp. 585–587, June 2001.

[119] Q. Xu, L. Chen, M. G. Wood, P. Sun, and R. M. Reano, "Electrically tunable optical polarization rotation on a silicon chip using Berrys phase," *Nature Communications*, vol. 5, p. 5337, Nov. 2014. [Online]. Available: http://dx.doi.org/10.1038/ncomms6337

[120] D. C. Hutchings and B. M. Holmes, "A waveguide polarization toolset design based on mode beating," *IEEE Photonics Journal*, vol. 3, no. 3, pp. 450–461, June 2011.

[121] J.-W. Kim, S.-H. Park, W.-S. Chu, and M.-C. Oh, "Integrated-optic polarization controllers incorporating polymer waveguide birefringence modulators," *Opt. Express*, vol. 20, no. 11, pp. 12 443–12 448, May 2012. [Online]. Available: http://www.opticsexpress.org/abstract.cfm?URI=oe-20-11-12443

[122] T. Okoshi and K. Kikuchi, *Coherent optical fiber communications*. Springer Science & Business Media, 1988, vol. 4.

[123] M. Cvijetic and I. Djordjevic, *Advanced optical communication systems and networks*. Artech House, 2013.

[124] M. Nakazawa, K. Kikuchi, and T. Miyazaki, *High Spectral Density Optical Communication Technologies*, ser. 6. Springer Berlin Heidelberg, 2010.

[125] A. Davis, M. Pettitt, J. King, and S. Wright, "Phase diversity techniques for coherent optical receivers," *Journal of lightwave technology*, vol. 5, no. 4, pp. 561–572, 1987.

[126] C. R. Doerr, "Silicon photonic integration in telecommunications," *Frontiers in Physics*, vol. 3, p. 37, 2015.

[127] S. J. Savory, "Coherent detection-why is it back?" in *Lasers and Electro-Optics Society, 2007. LEOS 2007. The 20th Annual Meeting of the IEEE*. IEEE, 2007, pp. 212–213.

[128] R. Linke, B. Kasper, N. Olsson, and R. Alferness, "Coherent lightwave transmission over 150 km fibre lengths at 400 Mbit/s and 1 Gbit/s data rates using phase modulation," *Electronics Letters*, vol. 22, no. 1, pp. 30–31, 1986.

[129] B. S. Glance, "Polarization independent coherent optical receiver," *Journal of Lightwave Technology*, vol. 5, p. 274, 1987.

[130] P. J. R. Iglesias, "Nuevos esquemas de recepcion coherente multipuerto para comunicaciones opticas," Ph.D. dissertation, Universidad de Málaga, 2015.

[131] P. R. Iglesias, I. M. Fernández, and W. Forysiak, "Long amplifier-spacing 16× 40 Gbit/s transmission with standard fiber," in *Conference on Lasers and Electro-Optics*. Optical Society of America, 2000, p. CTuG4.

[132] R. Griffin and A. Carter, "Optical differential quadrature phase-shift key (oDQPSK) for high capacity optical transmission," in *Optical Fiber Communication Conference*. Optical Society of America, 2002, p. WX6.

[133] "Coherent WDM technologies," Infinera Corporation, Tech. Rep., 2015. [Online]. Available: https://www.infinera.com/wp-content/uploads/2015/07/Infinera_Coherent_Tech.pdf

[134] "40Gb/s DQPSK receiver," Optoplex Corporation, Tech. Rep., 2016. [Online]. Available: http://www.optoplex.com/download/Optoplex%20Datasheets_Integrated%2040G%20DQPSK%20Receiver_2016_ar.pdf

[135] C. R. Doerr, P. J. Winzer, Y. K. Chen, S. Chandrasekhar, M. S. Rasras, L. Chen, T. Y. Liow, K. W. Ang, and G. Q. Lo, "Monolithic polarization and phase diversity coherent receiver in silicon," *Journal of Lightwave Technology*, vol. 28, no. 4, pp. 520–525, Feb 2010.

[136] "AC100-MSA product family," Acacia Communications Inc., Tech. Rep. [Online]. Available: http://acacia-inc.com/products/ac100-msa-product-family/

[137] OIF, "Technology options for 400G implementation," OIF, Tech. Rep., 2015. [Online]. Available: http://www.oiforum.com/wp-content/uploads/OIF-DPC-MRX-01.0-IA.pdf

[138] K. Wang, Y. Lu, L. Liu, B. Mao, B. Wu, Y. Huang, R. Mo, Y. Wang, and L. Li, "Dual-carrier 400G field trial submarine transmission over 6,577-km using 60-GBaud digital faster-than-nyquist shaping PDM-QPSK modulation format," in *2015 Optical Fiber Communications Conference and Exhibition (OFC)*, March 2015, pp. 1–3.

[139] R. Rios-Müller, J. Renaudier, P. Brindel, C. Simonneau, P. Tran, A. Ghazisaeidi, I. FernÃ¡ndez, L. Schmalen, and G. Charlet, "Optimized spectrally efficient transceiver for 400-Gb/s single carrier transport," in *2014 The European Conference on Optical Communication (ECOC)*, Sept 2014, pp. 1–3.

[140] E. Agrell, M. Karlsson, A. Chraplyvy, D. J. Richardson, P. M. Krummrich, P. Winzer, K. Roberts, J. K. Fischer, S. J. Savory, B. J. Eggleton *et al.*, "Roadmap of optical communications," *Journal of Optics*, vol. 18, no. 6, p. 063002, 2016.

[141] E. Ip, A. Lau, D. Barros, and J. Kahn, "Coherent detection in optical fiber systems," *Opt. Express*, vol. 16, no. 2, pp. 753–791, 2008.

[142] S. J. Savory, "Digital coherent optical receivers: Algorithms and subsystems," *IEEE Journal of Selected Topics in Quantum Electronics*, vol. 16, no. 5, pp. 1164–1179, Sept 2010.

[143] I. Fatadin, S. J. Savory, and D. Ives, "Compensation of quadrature imbalance in an optical QPSK coherent receiver," *IEEE Photonics Technology Letters*, vol. 20, no. 20, pp. 1733–1735, Oct 2008.

[144] D. Godard, "Self-recovering equalization and carrier tracking in two-dimensional data communication systems," *IEEE Transactions on Communications*, vol. 28, no. 11, pp. 1867–1875, Nov 1980.

[145] J. Yang, J.-J. Werner, and G. A. Dumont, "The multimodulus blind equalization and its generalized algorithms," *IEEE Journal on Selected Areas in Communications*, vol. 20, no. 5, pp. 997–1015, 2002.

[146] K. Mueller and M. Muller, "Timing recovery in digital synchronous data receivers," *IEEE Transactions on Communications*, vol. 24, no. 5, pp. 516–531, May 1976.

[147] E. Ip and J. M. Kahn, "Feedforward carrier recovery for coherent optical communications," *Journal of Lightwave Technology*, vol. 25, no. 9, pp. 2675–2692, 2007.

[148] A. J. Viterbi and A. M. Viterbi, "Nonlinear estimation of psk-modulated carrier phase with application to burst digital transmission," *IEEE Transactions on information theory*, vol. 29, no. 4, p. 543, 1983.

[149] R. Kunkel, H. G. Bach, D. Hoffmann, C. M. Weinert, Ã. Molina-FernÃ¡ndez, and R. Halir, "First monolithic InP-based 90°-hybrid OEIC comprising balanced detectors for 100GE coherent frontends," in *Indium Phosphide Related Materials, 2009. IPRM '09. IEEE International Conference on*, May 2009, pp. 167–170.

[150] M. Seimetz and C.-M. Weinert, "Options, feasibility, and availability of 2×4 90° hybrids for coherent optical systems," *J. Lightwave Technol.*, vol. 24, no. 3, p. 1317, Mar 2006. [Online]. Available: http://jlt.osa.org/abstract.cfm?URI=jlt-24-3-1317

[151] P. Runge, S. Schubert, A. Seeger, K. Janiak, J. Stephan, D. Trommer, P. Domburg, and M. L. Nielsen, "Monolithic InP receiver chip with a 90° hybrid and 56 Ghz balanced photodiodes," *Opt. Express*, vol. 20, no. 26, pp. B250–B255, Dec 2012. [Online]. Available: http://www.opticsexpress.org/abstract.cfm?URI=oe-20-26-B250

[152] S.-H. Jeong and K. Morito, "Optical 90° hybrid with broad operating bandwidth of 94 nm," *Opt. Lett.*, vol. 34, no. 22, pp. 3505–3507, Nov 2009. [Online]. Available: http://ol.osa.org/abstract.cfm?URI=ol-34-22-3505

[153] P. Dong, X. Liu, S. Chandrasekhar, L. L. Buhl, R. Aroca, Y. Baeyens, and Y. K. Chen, "224-Gb/s PDM-16-QAM modulator and receiver based on silicon photonic integrated circuits," in *Optical Fiber Communication Conference and Exposition and the National Fiber Optic Engineers Conference (OFC/NFOEC), 2013*, March 2013, pp. 1–3.

[154] S. Farwell, P. Aivaliotis, Y. Qian, P. Bromley, R. Griggs, J. N. Y. Hoe, C. Smith, and S. Jones, "InP coherent receiver chip with high performance and manufacturability for CFP2 modules," in *Optical Fiber Communication Conference*. Optical Society of America, 2014, p. W1I.6. [Online]. Available: http://www.osapublishing.org/abstract.cfm?URI=OFC-2014-W1I.6

[155] P. Dong, C. Xie, and L. L. Buhl, "Monolithic polarization diversity coherent receiver based on 120-degree optical hybrids on silicon," *Opt. Express*, vol. 22, no. 2, pp. 2119–2125, Jan 2014. [Online]. Available: http://www.opticsexpress.org/abstract.cfm?URI=oe-22-2-2119

[156] L. Xiang, Y. Xu, Y. Yu, and X. Zhang, "An ultracompact DP-QPSK demodulator based on multimode interference and photonic crystals," *Journal of Lightwave Technology*, vol. 30, no. 11, pp. 1595–1601, June 2012.

[157] D. Dai, "Silicon polarization beam splitter based on an asymmetrical evanescent coupling system with three optical waveguides," *Journal of Lightwave Technology*, vol. 30, no. 20, pp. 3281–3287, Oct 2012.

[158] D. Pérez-Galacho, R. Zhang, A. Ortega-Moñux, R. Halir, C. Alonso-Ramos, P. Runge, K. Janiak, G. Zhou, H.-G. Bach, A. G. Steffan *et al.*, "Integrated polarization beam splitter for 100/400 GE polarization multiplexed coherent optical communications," *Journal of Lightwave Technology*, vol. 32, no. 3, pp. 361–368, 2013.

[159] L. B. Soldano and E. C. Pennings, "Optical multi-mode interference devices based on self-imaging: principles and applications," *Journal of lightwave technology*, vol. 13, no. 4, pp. 615–627, 1995.

[160] M. Smit, X. Leijtens, H. Ambrosius, E. Bente, J. Van der Tol, B. Smalbrugge, T. De Vries, E.-J. Geluk, J. Bolk, R. Van Veldhoven *et al.*, "An introduction to InP-based generic integration technology," *Semiconductor Science and Technology*, vol. 29, no. 8, p. 083001, 2014.

[161] H. Mardoyan, O. B. Pardo, P. Jennevé, G. de Valicourt, M. A. Mestre, S. Bigo, C. Kazmierski, N. Chimot, A. Steffan, J. Honecker, R. Zhang, P. Runge, A. R. Richter, C. Arellano, A. Ortega-Moñux, and Í. M. Fernández, "PIC-to-PIC experiment at 130Gb/s based on a monolithic transmitter using switching of prefixed optical phases and a monolithic coherent receiver," in *Optical Fiber Communication Conference: Postdeadline Papers*. Optical Society of America, 2014, p. Th5C.2. [Online]. Available: http://www.osapublishing.org/abstract.cfm?URI=OFC-2014-Th5C.2

[162] PARADIGM and E. consortia, *JePPIX - PARADIGM/EuroPIC Design Manual*.

[163] [Online]. Available: http://www.photond.com.

[164] M. Heiblum and J. Harris, "Analysis of curved optical waveguides by conformal transformation," *IEEE Journal of Quantum Electronics*, vol. 11, no. 2, pp. 75–83, February 1975.

[165] W. Bogaerts, P. Dumon, D. Van Thourhout, and R. Baets, "Low-loss, low-cross-talk crossings for silicon-on-insulator nanophotonic waveguides," *Optics letters*, vol. 32, no. 19, pp. 2801–2803, 2007.

[166] P. Sanchis, J. Galan, A. Griol, J. Marti, M. Piqueras, and J. Perdigues, "Low-crosstalk in silicon-on-insulator waveguide crossings with optimized-angle," *IEEE Photonics Technology Letters*, vol. 19, no. 20, pp. 1583–1585, 2007.

[167] R. Halir, G. Roelkens, A. Ortega-Moñux, and J. G. Wangüemert-Pérez, "High-performance 90° hybrid based on a silicon-on-insulator multimode interference coupler," *Opt. Lett.*, vol. 36, no. 2, pp. 178–180, Jan 2011. [Online]. Available: http://ol.osa.org/abstract.cfm?URI=ol-36-2-178

[168] M. Bachmann, P. A. Besse, and H. Melchior, "Overlapping-image multimode interference couplers with a reduced number of self-images for uniform and nonuniform power splitting," *Appl. Opt.*, vol. 34, no. 30, pp. 6898–6910, Oct 1995. [Online]. Available: http://ao.osa.org/abstract.cfm?URI=ao-34-30-6898

[169] R. Halir, "Photonic reflectometer on silicon-on-insulator," Ph.D. dissertation, Universidad de Málaga, 2010.

[170] [Online]. Available: https://www.hhi.fraunhofer.de/en/departments/pc/research-groups/detectors.html

[171] V. Donzella, A. Sherwali, J. Flueckiger, S. T. Fard, S. M. Grist, and L. Chrostowski, "Sub-wavelength grating components for integrated optics applications on soi chips," *Opt. Express*, vol. 22, no. 17, pp. 21 037–21 050, Aug 2014. [Online]. Available: http://www.opticsexpress.org/abstract.cfm?URI=oe-22-17-21037

[172] J. G. Wangüemert-Pérez, P. Cheben, A. Ortega-Moñux, C. Alonso-Ramos, D. Pérez-Galacho, R. Halir, Í. Molina-Fernández, D.-X. Xu, and J. H. Schmid, "Evanescent field waveguide sensing with subwavelength grating structures in silicon-on-insulator," *Opt. Lett.*, vol. 39, no. 15, pp. 4442–4445, Aug 2014. [Online]. Available: http://ol.osa.org/abstract.cfm?URI=ol-39-15-4442

[173] P. J. Bock, P. Cheben, J. H. Schmid, J. Lapointe, A. Delâge, D.-X. Xu, S. Janz, A. Densmore, and T. J. Hall, "Subwavelength grating crossings for silicon wire waveguides," *Opt. Express*, vol. 18, no. 15, pp. 16 146–16 155, Jul 2010. [Online]. Available: http://www.opticsexpress.org/abstract.cfm?URI=oe-18-15-16146

[174] J. Wang, R. Ashrafi, R. Adams, I. Glesk, I. Gasulla, J. Capmany, and L. R. Chen, "Subwavelength grating enabled on-chip ultra-compact optical true time delay line," *Scientific Reports*, vol. 6, 2016.

[175] D. Pérez-Galacho, D. Marris-Morini, A. Ortega-Moñux, J. G. Wangüemert-Pérez, and L. Vivien, "Add/drop mode-division multiplexer based on a mach -zehnder interferometer and periodic waveguides," *IEEE Photonics Journal*, vol. 7, no. 4, pp. 1–7, Aug 2015.

[176] H. Yun, Y. Wang, F. Zhang, Z. Lu, S. Lin, L. Chrostowski, and N. A. F. Jaeger, "Broadband 2×2 adiabatic 3 dB coupler using silicon-on-insulator sub-wavelength grating waveguides," *Opt. Lett.*, vol. 41, no. 13, pp. 3041–3044, Jul 2016. [Online]. Available: http://ol.osa.org/abstract.cfm?URI=ol-41-13-3041

[177] A. Sánchez-Postigo, J. G. Wangüemert-Pérez, J. M. Luque-González, Í. Molina-Fernández, P. Cheben, C. A. Alonso-Ramos, R. Halir, J. H. Schmid, and A. Ortega-Moñux, "Broadband fiber-chip zero-order surface grating coupler with 0.4 dB efficiency," *Opt. Lett.*, vol. 41, no. 13, pp. 3013–3016, Jul 2016. [Online]. Available: http://ol.osa.org/abstract.cfm?URI=ol-41-13-3013

[178] Y. Xiong, D. X. Xu, J. H. Schmid, P. Cheben, and W. N. Ye, "High extinction ratio and broadband silicon TE-pass polarizer using subwavelength grating index engineering," *IEEE Photonics Journal*, vol. 7, no. 5, pp. 1–7, Oct 2015.

[179] J. Wang, I. Glesk, and L. R. Chen, "Subwavelength grating filtering devices," *Opt. Express*, vol. 22, no. 13, pp. 15 335–15 345, Jun 2014. [Online]. Available: http://www.opticsexpress.org/abstract.cfm?URI=oe-22-13-15335

[180] P. Bienstman, S. Selleri, L. Rosa, H. P. Uranus, W. C. L. Hopman, R. Costa, A. Melloni, L. C. Andreani, J. P. Hugonin, P. Lalanne, D. Pinto, S. S. A. Obayya, M. Dems, and K. Panajotov, "Modelling leaky photonic wires: A mode solver comparison," *Optical and Quantum Electronics*, vol. 38, no. 9, pp. 731–759, 2006. [Online]. Available: http://dx.doi.org/10.1007/s11082-006-9025-9

[181] A. Kumar, K. Thyagarajan, and A. K. Ghatak, "Analysis of rectangular-core dielectric waveguides: an accurate perturbation approach," *Opt. Lett.*, vol. 8, no. 1, pp. 63–65, Jan 1983. [Online]. Available: http://ol.osa.org/abstract.cfm?URI=ol-8-1-63

[182] L. Zavargo-Peche, A. Ortega-Moñux, J. G. Wangüemert-Pérez, and I. Molina-Fernández, "Fourier based combined techniques to design novel sub-wavelength optical integrated devices," *Progress In Electromagnetics Research*, vol. 123, pp. 447–465, 2012.

[183] NTT. (2017) One petabit per second fiber transmission over a record distance of 200 km.

[184] IBM. (2015) IBM silicon photonics technology ready to speed up cloud and big data applications.

[185] G. Corrielli, A. Crespi, R. Geremia, R. Ramponi, L. Sansoni, A. Santinelli, P. Mataloni, F. Sciarrino, and R. Osellame, "Rotated waveplates in integrated waveguide optics," *Nature Communications*, vol. 5, p. 4249, Jun. 2014. [Online]. Available: http://dx.doi.org/10.1038/ncomms5249

[186] J. D. Sarmiento-Merenguel, C. Alonso-Ramos, R. Halir, L. Vivien, P. Cheben, A. Ortega-Moñux, Í. Molina-Fernández, X. Leroux, D. Marris-Morini, D. X. Xu, J. H. Schmid, and S. Janz, "Silicon-on-insulator polarization controller with

relaxed fabrication tolerances," in *11th International Conference on Group IV Photonics (GFP)*, Aug 2014, pp. 87–88.

[187] K. Kanonakis, I. Tomkos, T. Pfeiffer, J. Prat, and P. Kourtessis, "Accordance: A novel ofdma-pon paradigm for ultra-high capacity converged wireline-wireless access networks," in *2010 12th International Conference on Transparent Optical Networks*, June 2010, pp. 1–4.